# Low-Speed Sensorless Control of Permanent-Magnet Synchronous Motors

by

Christian Aaen

A thesis submitted in partial fulfilment
of the requirements for the degree of

Master of Science

in

Mechatronic Control Engineering

Aalborg University
May 2014

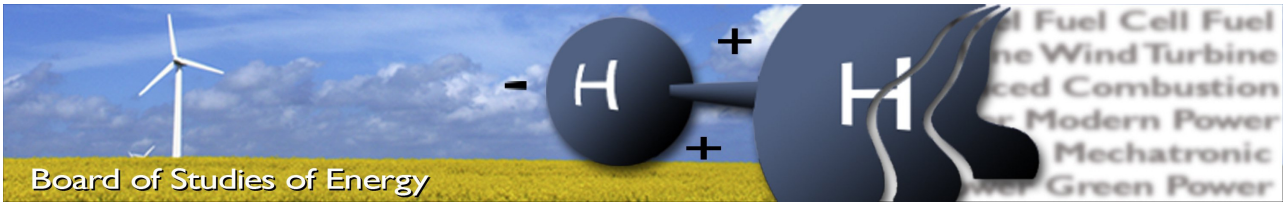


| | |
|---|---|
| **Title:** | Low-Speed Sensorless Control of Permanent-Magnet Synchronous Motors |
| **Semester:** | 9 & 10 |
| **Project period:** | 01.09.13 to 27.05.14 |
| **ECTS:** | 50 |
| **Supervisor:** | Kaiyuan Lu |
| **Project group:** | MCE4-1026 |

**SYNOPSIS:**

This thesis presents, in the framework of space vectors, sensorless schemes for field-oriented control of permanent-magnet synchronous motors for speeds of 10 RPM and below. A method based on high-frequency voltage injection is initially developed, but due to its sensitivity to the voltage error introduced by voltage source inverter drives, the focus shifts to voltage pulse injection methods that are robust to this error. A modification of the INFORM method shows reasonable tracking performance, but its accuracy degrades with load current. A new algorithm is developed that incorporates the advantages of the INFORM method and can estimate the rotor position to within ±20° electrical, regardless of load current.

Christian Aaen

| | |
|---|---|
| Copies: | 2 |
| Pages, total: | 110 |
| Appendix: | 1 |
| Supplements: | Attached DVD |

**By signing this document, each member of the group confirms that all group members have participated in the project work, and thereby all members are collectively liable for the contents of the report. Furthermore, all group members confirm that the report does not include plagiarism.**

# Preface

This thesis was written during the fall and spring semesters of 2013 and 2014, respectively, as part of the M.Sc. study programme in Mechatronic Control Engineering at the Department of Energy Technology, Aalborg University, Denmark. It is submitted in partial fulfilment of the requirements for the degree of Master of Science in Mechatronic Control Engineering.

The work presented here is in large part based on experiments performed at the Advanced Electric Machine and Drive Laboratory, Pontoppidanstræde 109, room 19, Aalborg University, Denmark.

The Author would like to thank OJ Electronics, Sønderborg, Denmark for providing the project proposal and a student grant to help develop this thesis.

The attached DVD contains an electronic copy of this thesis and all papers referenced in it.

# Abstract

Permanent-magnet synchronous motors provide, in conjunction with field-oriented control (FOC), a servo system with very high power density, efficiency and dynamic performance. The drawback of the classical FOC configuration is the requirement of a position or speed sensor for its reference frame transformations.

Sensorless control schemes aim to eliminate this sensor from the FOC topology, which the back-EMF estimation methods have generally succeeded in for motor speeds above, typically, 15 % to 20 % of rated value. The focus of this thesis is on developing sensorless schemes that function reliably in the low-speed range, which is defined here as speeds at or below 10 RPM, including operation at standstill.

In this thesis, in the framework of space vectors, high-frequency and voltage pulse injection methods are developed and tested by experiment.

The high-frequency injection methods are generally sensitive to the voltage error introduced by the nonideal characteristics of voltage source inverter drives. Compensating for the inverter voltage error typically requires offline characterization of the inverter, which represents an impractical dependency.

Instead of compensating for the inverter voltage error, the voltage pulse injection methods are instead developed to be robust to it. The INFORM method is modified to directly take into account the inverter voltage error, and measurements results show reasonable tracking performance of the rotor position, which, due to the effect of magnetic saturation, degrades significantly above the rated current of the motor tested.

A new algorithm is developed based on the same fundamentals as the INFORM method, but which deliberately utilizes less information. This restricts the estimate of the rotor position to fixed 30° sectors, but in doing so, the algorithm is able to reliably estimate the rotor position to within ±20° electrical, regardless of the level of load current. For low levels of load current, the estimation error of the INFORM method is slightly lower.

# Key Symbols and Abbreviations

| | |
|---|---|
| $\boldsymbol{K}$ | Matrix |
| $\mathbf{k}$ | Space vector (complex) |
| $\overline{\mathbf{k}}$ | Complex conjugate of $\mathbf{k}$ |
| $\mathbf{k}^{(\mathrm{r})}$ | Space vector $\mathbf{k}$ in reference frame (r) |
| AAF | Anti-aliasing filter |
| DFT | Discrete Fourier transform |
| DSP | Digital signal processor |
| FIR | Finite impulse response |
| FOC | Field-oriented control |
| IIR | Infinite impulse response |
| LPF | Low-pass filter |
| LSB | Least significant bit |
| IMPMSM | Interior-mounted permanent-magnet synchronous motor |
| PM | Permanent magnet |
| SMPMSM | Surface-mounted permanent-magnet synchronous motor |
| SNR | Signal-to-noise ratio |
| SVM | Space-vector modulation |
| SVT | Space-vector transformation |
| VSI | Voltage source inverter |

If not otherwise specified:

- Amplitudes are peak values.
- No windowing is used for the DFT.
- $\arg(z), z \in \mathbb{C}$ gives the principal value in the range $[-\pi; \pi]$.

# Contents

**Preface** v

**Abstract** vii

**Key Symbols and Abbreviations** ix

**1. Introduction** 1
1.1. Problem Statement . . . 2

**2. Space-Vector Model of the Permanent-Magnet Synchronous Motor** 3
2.1. Three-Phase Machine Equations . . . 3
2.2. The Space-Vector Transformation . . . 8
2.3. Conversion to Space-Vector Form . . . 10
2.3.1. Relationship to d-q Model . . . 12
2.3.2. Utility of a Complex Representation . . . 13
2.4. Electromechanical Torque . . . 15

**3. Hardware Platform** 17
3.1. Inverter Voltage Error . . . 20
3.1.1. Measuring the Voltage Error . . . 22
3.1.2. Measurement Results . . . 23

**4. High-Frequency Voltage Injection** 25
4.1. High-Frequency Model . . . 26
4.2. Four-Quadrant Estimation of Rotor Position . . . 29
4.3. Polarity Detection of PM Field . . . 31
4.4. Effect of Stator Winding Resistance . . . 34
4.5. Measurement Results . . . 36
4.5.1. Linear Inverter Range . . . 36
4.5.2. Nonlinear Inverter Range . . . 40
4.5.3. Spectrum of Current Response to Inverter Voltage Error . . . 40
4.6. Summary . . . 47

**5. Voltage Pulse Injection** 49
5.1. Clamping the Voltage Injection Angle . . . 49
5.2. The INFORM Method . . . 52
5.2.1. Interperiod Sampling . . . 56

5.2.2. Estimation Rate . . . . . 57
5.2.3. Effect of Magnetic Saturation . . . . . 58
5.2.4. Measurement Results, Siemens Motor . . . . . 61
5.2.5. Measurement Results, SEM Motor . . . . . 64
5.3. Sector Estimation . . . . . 65
5.3.1. Measurement Results, Siemens Motor . . . . . 80
5.3.2. Measurement Results, SEM Motor . . . . . 80
5.4. Summary . . . . . 90

**6. Conclusion** **91**
6.1. Future Work . . . . . 92

**A. Noise Filtering of the LEM LA-P Series Current Transducer** **93**

**Bibliography** **97**

# 1. Introduction

With the advent, in recent years, of cheap microprocessors, power electronics and new, powerful magnet alloys, the applications for permanent-magnet synchronous motors have expanded greatly. They are generally considered the benchmark for high power density and efficiency, and combined with field-oriented control, they have excellent dynamic performance. As such, they are often the motor of choice in high performance servo systems, and especially so when the system package has to be compact.

The advantages of field-oriented control has generally caused it to become the de facto standard control topology in modern servo drives. The pervasiveness of the technology has led to a surge in interest in eliminating what is perceived as the main drawback of the classical FOC configuration, namely the requirement of a rotor position or speed sensor for its reference frame transformations. These sensors add cost and complexity to the servo system.

For a low-cost motor, the cost of the sensor can represent a nontrivial share of its unit price. For larger, more expensive motors, the predominant concern is the reliability of the electrical and mechanical components of the sensor.

Sensorless schemes for PMSM, in which the rotor position is determined without direct feedback, is an active area of research, but well-documented solutions, primarily based on back-EMF estimation, already exist for motor speeds typically in excess of 15 % to 20 % of its rated value (Yongdong and Hao 2008). For low-speed operation, which we will define here as speeds at or below 10 RPM, the low signal-to-noise ratio of the back-EMF generally make these algorithms unusable. The focus of this thesis is on sensorless schemes that can estimate the rotor position reliably at low speed to standstill.

Permanent-magnet synchronous motors are broadly classified according to the mounting method of the permanent magnets. The two prevailing classes are:

- Surface-Mounted Permanent-Magnet Synchronous Motor (SMPMSM).
- Interior-Mounted Permanent-Magnet Synchronous Motor (IMPMSM).

A schematic of the two classes are shown in Figure 1.1.

Motors of the IMPMSM type are generally better suited for low-speed sensorless control, in that they have a significant air gap, effectively, that varies with the rotor position. It is this anisotropic property of the motor that be utilized in low-speed sensorless schemes to estimate the rotor position. This effect is also present in a SMPMSM due to a

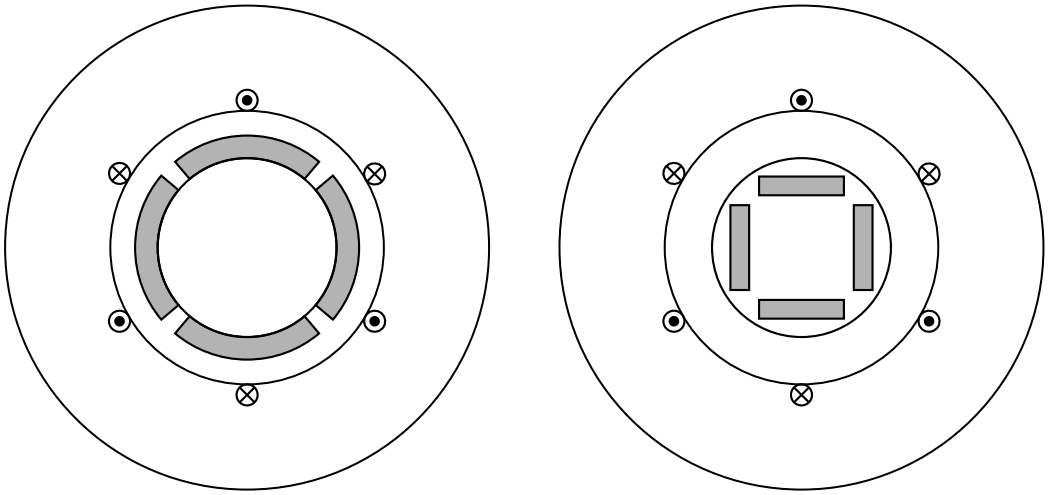

(a) SMPMSM (b) IMPMSM

Figure 1.1.: Schematic of a PMSM. Magnet alloy shown in grey.

directional-dependent saturation of the machine iron by the PM flux, but it is much less prominent.

In this thesis, we will limit ourselves to working with surface-mounted permanent-magnet synchronous motors, based on the hypothesis that: If it works for a SMPMSM, it will work for a IMPMSM.

## 1.1. Problem Statement

The classical FOC configuration requires a position or speed sensor for its reference frame transformations. In order to lower cost and increase reliability, this dependency must be removed.

In order to do without the position or speed sensor, the angular position of the rotor must be determined by other means. For low-speed operation, the sensorless schemes based on back-EMF estimation are generally unusable.

New algorithms must be developed, if possible, that allow us to estimate the rotor position at low speed.

# 2. Space-Vector Model of the Permanent-Magnet Synchronous Motor

This chapter is dedicated to deriving a mathematical model of a wye-connected, three-phase permanent-magnet synchronous machine with an isolated neutral for use in motor control applications. A model of the PMSM in phase quantities of voltage, current and flux linkage, followed by a conversion to its space-vector representation, will form the outline of the chapter. Some basic properties of space vectors are included for reference purposes, and the merits of using a space-vector representation is touched on briefly.

## 2.1. Three-Phase Machine Equations

Figure 2.1a shows a schematic diagram of a three-phase, one pole-pair SMPMSM. The stator windings are pictured as coils of a single turn, but it is important to note they are meant to portray the windings of a generalized machine. The physical stator windings could be distributed or concentrated, but with the same magnetic axes as the windings shown in Figure 2.1a.

A simplified diagram is shown in Figure 2.1b with the stator windings schematically represented as concentrated coils aligned with their respective magnetic axes. Assuming a symmetric machine, the schematic shown could then also represent a machine with an arbitrary number of pole-pairs, reduced to its one pole-pair equivalent.

The derivation in this chapter makes the following assumptions:

(1) The machine is symmetric.

(2) The stator winding resistances are constant.

(3) The magnetic system of the machine is linear.

(4) For spatial distributions, only the fundamental component is considered. Harmonics are disregarded.

(5) The spatial amplitude of the PM flux linkage is constant.

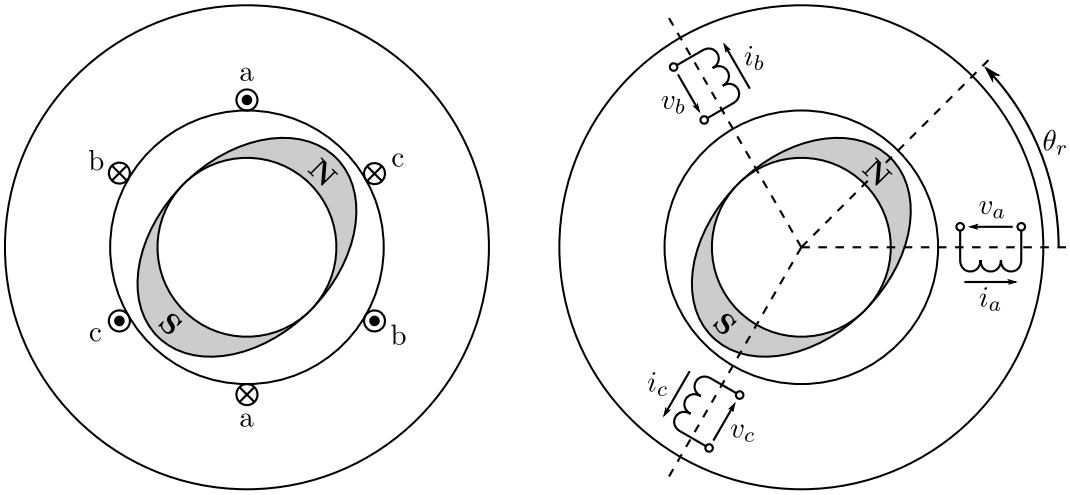


(a) Peak location of winding distributions (b) Simplified representation

Figure 2.1.: Schematic of a three-phase, one-pole pair SMPMSM. Magnet alloy shown in grey.

For the PMSM in Figure 2.1, enumerate the phase windings as a, b and c. The governing system of equations is then:

$$v_a = R_s i_a + \frac{\mathrm{d}\Psi_a}{\mathrm{d}t} \tag{2.1a}$$

$$v_b = R_s i_b + \frac{\mathrm{d}\Psi_b}{\mathrm{d}t} \tag{2.1b}$$

$$v_c = R_s i_c + \frac{\mathrm{d}\Psi_c}{\mathrm{d}t} \tag{2.1c}$$

where:

- $v_a$, $v_b$, $v_c$ are phase voltages,
- $i_a$, $i_b$, $i_c$ are phase currents,
- $\Psi_a$, $\Psi_b$, $\Psi_c$ is the magnetic flux linkage with winding a, b and c, respectively,
- $R_s$ is the stator winding resistance.

The total magnetic flux linkage with, for instance, phase a is given by:

$$\Psi_a = \Psi_{aa} + \Psi_{ab} + \Psi_{ac} + \Psi_{af} \tag{2.2}$$

where:

- $\Psi_{aa}$, $\Psi_{ab}$, $\Psi_{ac}$ is the component of flux linkage induced by current in phase a, b, c, respectively.

- $\Psi_{af}$ is the component of flux linkage generated by the magnetic field of the permanent magnets.

The flux linkage components $\Psi_{aa}$, $\Psi_{ab}$, $\Psi_{ac}$ can be expressed in terms of phase currents as:

$$\Psi_{aa} = L_{aa} i_a \tag{2.3}$$
$$\Psi_{ab} = M_{ab} i_b \tag{2.4}$$
$$\Psi_{ac} = M_{ac} i_c \tag{2.5}$$

where:

- $L_{aa}$ is the self-inductance of phase a,
- $M_{ab}$ is the mutual inductance between phase a and b,
- $M_{ac}$ is the mutual inductance between phase a and c.

Define the self-inductance of phase a as:

$$L_{aa} \triangleq L_\sigma + L_{Ma} \tag{2.6}$$

where:

- $L_\sigma$ is the stator winding leakage inductance,
- $L_{Ma}$ is the magnetizing inductance of phase a.

Since the difference in magnetic permeability of air and magnet alloy is usually considered negligible, the SMPMSM effectively has a non-salient rotor and, as a consequence, a near-uniform air gap. A slight distortion of this air gap occurs, though, as a consequence of saturation of the stator iron by the PM flux. Saturation has the effect of increasing the reluctance along the magnetic axis of the PM field, which can be visualized as a localized increase in the effective air gap, thus introducing rotor-saliency in the SMPMSM. This is schematically illustrated in Figure 2.2 for the PM field axis aligned and in quadrature with the magnetic axis of phase a.

For the position of the rotor in Figure 2.2a, the flux linkage with phase a, induced by current in phase a, should be at a *minimum*, since the phase is aligned with the path of maximum reluctance.

Similarly, for the position of the rotor in Figure 2.2b, the flux linkage with phase a, induced by current in phase a, should be at a *maximum*, since the phase is aligned with the path of minimum reluctance.

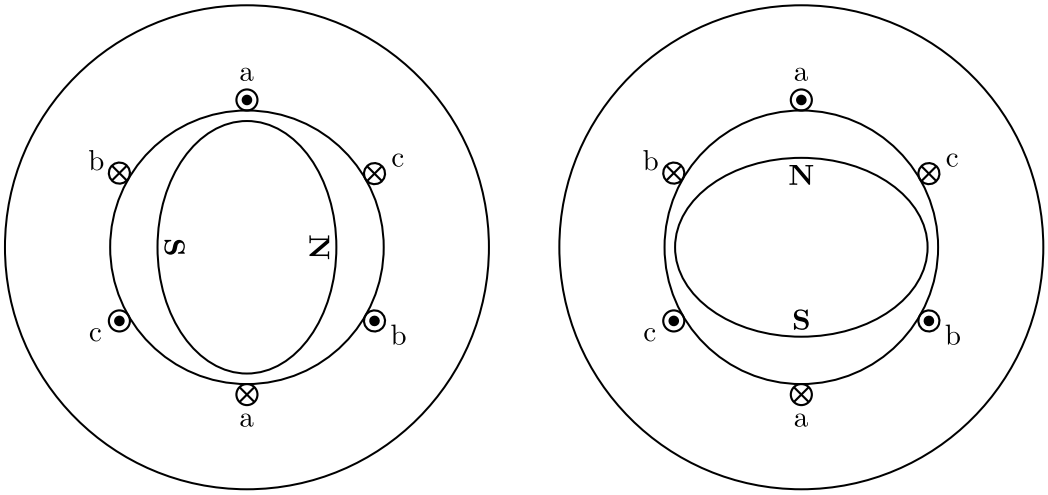


(a) Aligned with axis of phase a (b) In quadrature with axis of phase a

Figure 2.2.: Variation of the effective air gap due to saturation of the stator iron along the PM field axis.

It follows that $\Psi_{aa}$, and thereby $L_{aa}$, is a periodic function of $\theta_r$. Neglecting harmonics, the Fourier series expansion of $L_{aa}$ is then:

$$L_{aa} = L_\sigma + L_{Ma} = L_\sigma + L_A - L_B \cos 2\,\theta_r, \quad L_{Ma} = L_A - L_B \cos 2\,\theta_r \tag{2.7}$$

where $L_A$, $L_B$ are the Fourier coefficients of the partial sum.

Note that:

$$\cos 2(x) \triangleq \cos(2x) \tag{2.8}$$

Under the assumptions of this section, it can be shown that (Krause, Wasynczuk, and Sudhoff 2002):

$$L_{Ma} i_a + M_{ab} i_a + M_{ac} i_a = 0 \Leftrightarrow L_{Ma} + M_{ab} + M_{ac} = 0 \tag{2.9}$$

Constrained by symmetry, (2.9) is solved by:

$$M_{ab} = -\frac{1}{2} L_A - L_B \cos 2\Big(\theta_r - \frac{\pi}{3}\Big) \tag{2.10}$$

$$M_{ac} = -\frac{1}{2} L_A - L_B \cos 2\Big(\theta_r + \frac{\pi}{3}\Big) \tag{2.11}$$

Finally, since the PM flux links with phase a at an angle $\theta_r$, it follows that:

$$\Psi_{af} = \Psi_f \cos \theta_r \tag{2.12}$$

where $\Psi_f$ is the peak amplitude of the PM flux linkage.

Following the derivation of (2.2)–(2.12) for phase b and c yields:

$$\Psi_a = L_{aa} i_a + M_{ab} i_b + M_{ac} i_c + \Psi_f \cos\theta_r \tag{2.13}$$

$$\Psi_b = M_{ab} i_a + L_{bb} i_b + M_{bc} i_c + \Psi_f \cos\left(\theta_r - \frac{2\pi}{3}\right) \tag{2.14}$$

$$\Psi_c = M_{ac} i_a + M_{bc} i_b + L_{cc} i_c + \Psi_f \cos\left(\theta_r + \frac{2\pi}{3}\right) \tag{2.15}$$

$$L_{aa} = L_\sigma + L_A - L_B \cos 2\,\theta_r \tag{2.16}$$

$$L_{bb} = L_\sigma + L_A - L_B \cos 2\left(\theta_r - \frac{2\pi}{3}\right) \tag{2.17}$$

$$L_{cc} = L_\sigma + L_A - L_B \cos 2\left(\theta_r + \frac{2\pi}{3}\right) \tag{2.18}$$

$$M_{ab} = -\frac{1}{2} L_A - L_B \cos 2(\theta_r - \frac{\pi}{3}) \tag{2.19}$$

$$M_{ac} = -\frac{1}{2} L_A - L_B \cos 2(\theta_r + \frac{\pi}{3}) \tag{2.20}$$

$$M_{bc} = -\frac{1}{2} L_A - L_B \cos 2\,\theta_r \tag{2.21}$$

The system of (2.1) and (2.13)–(2.21) represents the model of the PMSM in phase quantities[1], which in matrix form is given by:

$$\boldsymbol{V_s} = R_s \boldsymbol{I_s} + \frac{\mathrm{d}\boldsymbol{\Psi_s}}{\mathrm{d}t} \tag{2.22}$$

$$\boldsymbol{\Psi_s} = (L_\sigma \mathbf{1} + L_A \boldsymbol{K} - L_B \boldsymbol{\Lambda}) \boldsymbol{I_s} + \Psi_f \boldsymbol{M} \tag{2.23}$$

where:

$$\boldsymbol{V_s} = \begin{bmatrix} v_a & v_b & v_c \end{bmatrix}^{\mathrm{T}} \tag{2.24}$$

$$\boldsymbol{I_s} = \begin{bmatrix} i_a & i_b & i_c \end{bmatrix}^{\mathrm{T}} \tag{2.25}$$

$$\boldsymbol{\Psi_s} = \begin{bmatrix} \Psi_a & \Psi_b & \Psi_c \end{bmatrix}^{\mathrm{T}} \tag{2.26}$$

$$\boldsymbol{K} = \begin{bmatrix} 1 & -\frac{1}{2} & -\frac{1}{2} \\ -\frac{1}{2} & 1 & -\frac{1}{2} \\ -\frac{1}{2} & -\frac{1}{2} & 1 \end{bmatrix} \tag{2.27}$$

$$\boldsymbol{\Lambda} = \begin{bmatrix} \cos 2\,\theta_r & \cos 2\big(\theta_r - \frac{\pi}{3}\big) & \cos 2\big(\theta_r + \frac{\pi}{3}\big) \\ \cos 2\big(\theta_r - \frac{\pi}{3}\big) & \cos 2\big(\theta_r - \frac{2\pi}{3}\big) & \cos 2\,\theta_r \\ \cos 2\big(\theta_r + \frac{\pi}{3}\big) & \cos 2\,\theta_r & \cos 2\big(\theta_r + \frac{2\pi}{3}\big) \end{bmatrix} \tag{2.28}$$

$$\boldsymbol{M} = \begin{bmatrix} \cos\theta_r \\ \cos\big(\theta_r - \frac{2\pi}{3}\big) \\ \cos\big(\theta_r + \frac{2\pi}{3}\big) \end{bmatrix} \tag{2.29}$$

[1] A full mathematical treatise can be found in Krause, Wasynczuk, and Sudhoff (2002).

## 2.2. The Space-Vector Transformation

Define the space-vector transformation as:

$$\mathbf{k} \triangleq \frac{2}{3}\left[k_a(t) + \mathbf{a}k_b(t) + \mathbf{a}^2 k_c(t)\right] \tag{2.30}$$

where $\{k_a(t), k_b(t), k_c(t)\}$ is a set of related phase quantities and:

$$\mathbf{a} = e^{j2\pi/3} = -\frac{1}{2} + j\frac{\sqrt{3}}{2} \tag{2.31}$$

The inverse space-vector transformation is then given by (Kazmierkowski and Tunia 1994):

$$k_a(t) = \mathrm{Re}(\mathbf{k}) + k_0 \tag{2.32a}$$
$$k_b(t) = \mathrm{Re}(\mathbf{a}^2\mathbf{k}) + k_0 \tag{2.32b}$$
$$k_c(t) = \mathrm{Re}(\mathbf{a}\mathbf{k}) + k_0 \tag{2.32c}$$

where:

$$k_0 = \frac{1}{3}\left[k_a(t) + k_b(t) + k_c(t)\right] \tag{2.33}$$

Eq. (2.30) can be expressed as:

$$\begin{aligned}\mathbf{k} &= \frac{2}{3}\left(k_a + \mathbf{a}k_b + \mathbf{a}^2 k_c\right) \\ &= \frac{2}{3}\left[k_a + \left(-\frac{1}{2} + j\frac{\sqrt{3}}{2}\right)k_b + \left(-\frac{1}{2} + j\frac{\sqrt{3}}{2}\right)^2 k_c\right] \\ &= \frac{2}{3}\left(k_a - \frac{1}{2}k_b - \frac{1}{2}k_c + j\frac{\sqrt{3}}{2}k_b - j\frac{\sqrt{3}}{2}k_c\right)\end{aligned} \tag{2.34}$$

Therefore, we have:

$$\mathrm{Re}(\mathbf{k}) = \frac{2}{3}\left(k_a - \frac{1}{2}k_b - \frac{1}{2}k_c\right) \tag{2.35}$$
$$\mathrm{Im}(\mathbf{k}) = \frac{2}{3}\left(\frac{\sqrt{3}}{2}k_b - \frac{\sqrt{3}}{2}k_c\right) \tag{2.36}$$

Eq. (2.33), (2.35) and (2.36) can then be combined in matrix form as:

$$\begin{bmatrix}\mathrm{Re}(\mathbf{k}) \\ \mathrm{Im}(\mathbf{k}) \\ k_0\end{bmatrix} = \frac{2}{3}\begin{bmatrix}1 & -\frac{1}{2} & -\frac{1}{2} \\ 0 & \frac{\sqrt{3}}{2} & -\frac{\sqrt{3}}{2} \\ \frac{1}{2} & \frac{1}{2} & \frac{1}{2}\end{bmatrix}\begin{bmatrix}k_a \\ k_b \\ k_c\end{bmatrix} \tag{2.37}$$

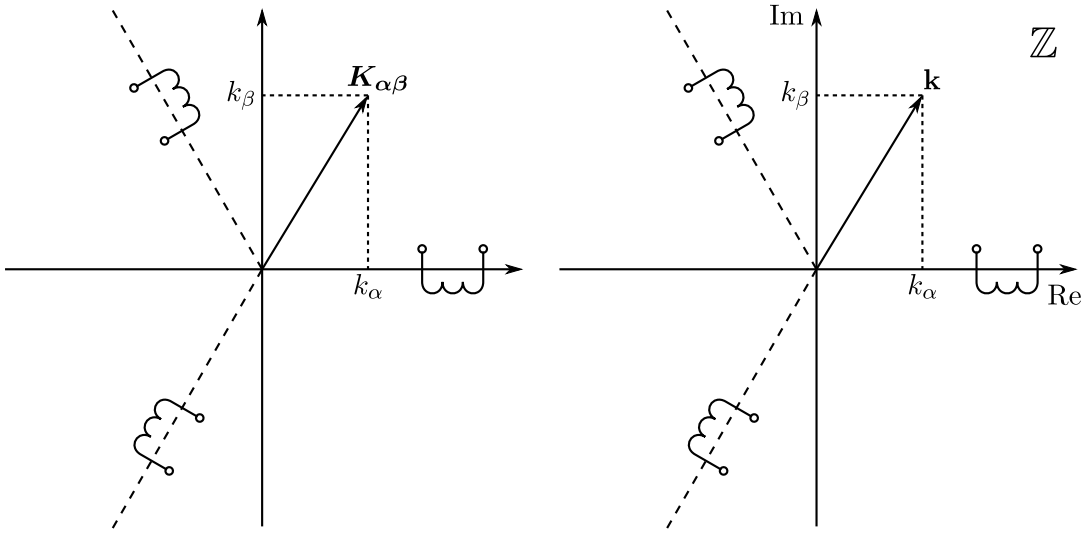


(a) Clarke transformation (b) Space-vector transformation

Figure 2.3.: Geometry of the resultant vectors of the Clarke and space-vector transformations.

Compare (2.37) to the amplitude-invariant Clarke, or $\alpha\beta\gamma$, transformation:

$$\boldsymbol{K_{\alpha\beta\gamma}} = \begin{bmatrix} k_\alpha \\ k_\beta \\ k_\gamma \end{bmatrix} = \frac{2}{3} \begin{bmatrix} 1 & -\frac{1}{2} & -\frac{1}{2} \\ 0 & \frac{\sqrt{3}}{2} & -\frac{\sqrt{3}}{2} \\ \frac{1}{2} & \frac{1}{2} & \frac{1}{2} \end{bmatrix} \begin{bmatrix} k_a \\ k_b \\ k_c \end{bmatrix} \tag{2.38}$$

Now define:

$$\boldsymbol{K_{\alpha\beta}} \triangleq \begin{bmatrix} k_\alpha \\ k_\beta \end{bmatrix} \tag{2.39}$$

It is apparent, then, that the space vector $\mathbf{k}$ is simply a complex representation of $\boldsymbol{K_{\alpha\beta}}$:

$$\mathbf{k} = k_\alpha + jk_\beta \tag{2.40}$$

In a geometrical sense, $\mathbf{k}$ and $\boldsymbol{K_{\alpha\beta}}$ represents the same vector, but where the Clarke transformation employs a real basis, the space-vector transformation substitutes in the complex plane, as shown in Figure 2.3.

The space-vector transformation has a simple matrix form, given by:

$$\mathbf{k} = \frac{2}{3}\left(k_a + \mathbf{a}k_b + \mathbf{a}^2 k_c\right) = \frac{2}{3}\boldsymbol{A}\boldsymbol{K_{abc}} \tag{2.41}$$

where:

$$\boldsymbol{A} = \begin{bmatrix} 1 & \mathbf{a} & \mathbf{a}^2 \end{bmatrix} \tag{2.42}$$

$$\boldsymbol{K_{abc}} = \begin{bmatrix} k_a & k_b & k_c \end{bmatrix}^{\mathrm{T}} \tag{2.43}$$

We can then interpret $\frac{2}{3}\boldsymbol{A}$ as a space-vector *operator*. Additionally, since:

$$\begin{aligned}\mathrm{Re}(\mathbf{k}) &= \frac{2}{3}\left[\mathrm{Re}(k_a) + \mathrm{Re}(\mathbf{a}k_b) + \mathrm{Re}(\mathbf{a}^2k_c)\right] \\ &= \frac{2}{3}\left[k_a + \frac{1}{2}(\mathbf{a}k_b + \mathbf{a}^2k_b) + \frac{1}{2}(\mathbf{a}^2k_c + \mathbf{a}k_c)\right] \qquad (2.44)\\ \mathrm{Im}(\mathbf{k}) &= \frac{2}{3}\left[\mathrm{Im}(k_a) + \mathrm{Im}(\mathbf{a}k_b) + \mathrm{Im}(\mathbf{a}^2k_c)\right] \\ &= \frac{2}{3}\left[\frac{1}{j2}(\mathbf{a}k_b - \mathbf{a}^2k_b) + \frac{1}{j2}(\mathbf{a}^2k_c - \mathbf{a}k_c)\right] \qquad (2.45)\end{aligned}$$

we have:

$$\begin{aligned}\overline{\mathbf{k}} &= \mathrm{Re}(\mathbf{k}) - j\,\mathrm{Im}(\mathbf{k}) \\ &= \frac{2}{3}\Big[k_a + \frac{1}{2}(\mathbf{a}k_b + \mathbf{a}^2k_b) + \frac{1}{2}(\mathbf{a}^2k_c + \mathbf{a}k_c) \\ &\qquad - \frac{1}{2}(\mathbf{a}k_b - \mathbf{a}^2k_b) - \frac{1}{2}(\mathbf{a}^2k_c - \mathbf{a}k_c)\Big] \\ &= \frac{2}{3}\left(k_a + \mathbf{a}^2k_b + \mathbf{a}k_c\right) \qquad (2.46)\end{aligned}$$

where $\mathbf{k}$ and $\overline{\mathbf{k}}$ are complex conjugates.

## 2.3. Conversion to Space-Vector Form

Recall the model of the PMSM in phase quantities:

$$\boldsymbol{V_s} = R_s\boldsymbol{I_s} + \frac{\mathrm{d}\boldsymbol{\Psi_s}}{\mathrm{d}t} \qquad (2.22 \text{ revisited})$$

$$\boldsymbol{\Psi_s} = (L_\sigma\mathbf{1} + L_A\boldsymbol{K} - L_B\boldsymbol{\Lambda})\boldsymbol{I_s} + \Psi_f\boldsymbol{M} \qquad (2.23 \text{ revisited})$$

Applying the space-vector operator:

$$\frac{2}{3}\boldsymbol{A}\boldsymbol{V_s} = R_s\frac{2}{3}\boldsymbol{A}\boldsymbol{I_s} + \frac{2}{3}\boldsymbol{A}\frac{\mathrm{d}\boldsymbol{\Psi_s}}{\mathrm{d}t} \qquad (2.47)$$

$$\frac{2}{3}\boldsymbol{A}\boldsymbol{\Psi_s} = L_\sigma\frac{2}{3}\boldsymbol{A}\boldsymbol{I_s} + L_A\frac{2}{3}\boldsymbol{A}\boldsymbol{K}\boldsymbol{I_s} - L_B\frac{2}{3}\boldsymbol{A}\boldsymbol{\Lambda}\boldsymbol{I_s} + \Psi_f\frac{2}{3}\boldsymbol{A}\boldsymbol{M} \qquad (2.48)$$

Converting (2.47) is trivial using the definition of the space-vector transformation:

$$\frac{2}{3}\boldsymbol{A}\boldsymbol{V_s} = R_s\frac{2}{3}\boldsymbol{A}\boldsymbol{I_s} + \frac{2}{3}\boldsymbol{A}\frac{\mathrm{d}\boldsymbol{\Psi_s}}{\mathrm{d}t} \Leftrightarrow \qquad (2.49)$$

$$\mathbf{v_s} = R_s\mathbf{i_s} + \frac{\mathrm{d}\boldsymbol{\Psi_s}}{\mathrm{d}t} \qquad (2.50)$$

where $\mathbf{v_s}$, $\mathbf{i_s}$ and $\boldsymbol{\Psi_s}$ are space vectors for phase voltages, currents and flux linkages, respectively.

Converting (2.48) requires expansion of its terms:

$$\begin{aligned}
L_A\frac{2}{3}\boldsymbol{AKI_s} &= L_A\frac{2}{3}\begin{bmatrix}1 & \mathbf{a} & \mathbf{a}^2\end{bmatrix}\begin{bmatrix}1 & -\frac{1}{2} & -\frac{1}{2}\\ -\frac{1}{2} & 1 & -\frac{1}{2}\\ -\frac{1}{2} & -\frac{1}{2} & 1\end{bmatrix}\begin{bmatrix}i_a\\ i_b\\ i_c\end{bmatrix}\\
&= \frac{3}{2}L_A\frac{2}{3}(i_a + \mathbf{a}i_b + \mathbf{a}^2 i_c)\\
&= \frac{3}{2}L_A\mathbf{i_s} \qquad (2.51)\\
L_B\frac{2}{3}\boldsymbol{A\Lambda I_s} &= L_B\frac{2}{3}\begin{bmatrix}1 & \mathbf{a} & \mathbf{a}^2\end{bmatrix}\\
&\quad\cdot\begin{bmatrix}\cos 2\,\theta_r & \cos 2\big(\theta_r - \frac{\pi}{3}\big) & \cos 2\big(\theta_r + \frac{\pi}{3}\big)\\ \cos 2\big(\theta_r - \frac{\pi}{3}\big) & \cos 2\big(\theta_r - \frac{2\pi}{3}\big) & \cos 2\,\theta_r\\ \cos 2\big(\theta_r + \frac{\pi}{3}\big) & \cos 2\,\theta_r & \cos 2\big(\theta_r + \frac{2\pi}{3}\big)\end{bmatrix}\begin{bmatrix}i_a\\ i_b\\ i_c\end{bmatrix}\\
&= \frac{3}{2}L_B\frac{2}{3}(i_a + \mathbf{a}^2 i_b + \mathbf{a}i_c)e^{j2\theta_r}\\
&= \frac{3}{2}L_B\overline{\mathbf{i_s}}e^{j2\theta_r} \qquad (2.52)\\
\Psi_f\frac{2}{3}\boldsymbol{AM} &= \Psi_f\frac{2}{3}\begin{bmatrix}1 & \mathbf{a} & \mathbf{a}^2\end{bmatrix}\begin{bmatrix}\cos\theta_r\\ \cos\big(\theta_r - \frac{2\pi}{3}\big)\\ \cos\big(\theta_r + \frac{2\pi}{3}\big)\end{bmatrix}\\
&= \Psi_f e^{j\theta_r} \qquad (2.53)
\end{aligned}$$

Substituting (2.51)–(2.53) in (2.48), we have:

$$\boldsymbol{\Psi_s} = \left(L_\sigma + \frac{3}{2}L_A\right)\mathbf{i_s} - \frac{3}{2}L_B\overline{\mathbf{i_s}}e^{j2\theta_r} + \Psi_f e^{j\theta_r} \qquad (2.54)$$

Define:

$$L_1 \triangleq L_\sigma + \frac{3}{2}L_A \qquad (2.55)$$

$$L_2 \triangleq \frac{3}{2}L_B \qquad (2.56)$$

The space-vector representation of the PMSM model is thus given by:

$$\mathbf{v_s} = R_s\mathbf{i_s} + \frac{\mathrm{d}\boldsymbol{\Psi}_\mathbf{s}}{\mathrm{d}t} \qquad (2.57)$$

$$\boldsymbol{\Psi}_\mathbf{s} = L_1\mathbf{i_s} - L_2\overline{\mathbf{i_s}}e^{j2\theta_r} + \Psi_f e^{j\theta_r} \qquad (2.58)$$

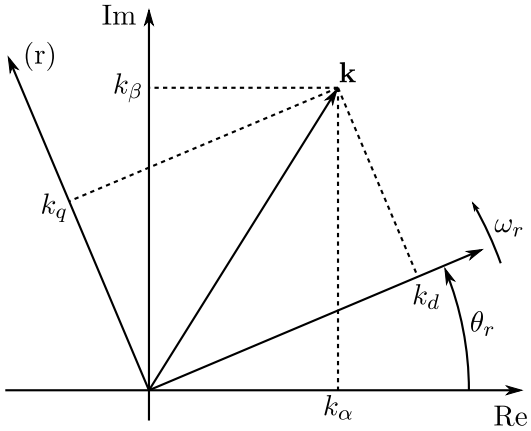


Figure 2.4.: Cartesian coordinates of the space vector $\mathbf{k}$ in a stationary and rotating reference frame with angular velocity $\omega_r$.

### 2.3.1. Relationship to d-q Model

Under the reference frame transformation:

$$\mathbf{k}^{(\mathrm{r})} = k_d + jk_q = \mathbf{k}e^{-j\theta_r} \Leftrightarrow \mathbf{k} = \mathbf{k}^{(\mathrm{r})}e^{j\theta_r} \tag{2.59}$$

where $\mathbf{k}^{(\mathrm{r})}$ is $\mathbf{k}$ as seen from the rotating frame of reference of the rotor, illustrated in Figure 2.4, (2.57) and (2.58) become:

$$\mathbf{v}_\mathbf{s}^{(\mathrm{r})}e^{j\theta_r} = R_s\mathbf{i}_\mathbf{s}^{(\mathrm{r})}e^{j\theta_r} + \frac{\mathrm{d}}{\mathrm{d}t}\left(\mathbf{\Psi}_\mathbf{s}^{(\mathrm{r})}e^{j\theta_r}\right) \tag{2.60}$$

$$\mathbf{\Psi}_\mathbf{s}^{(\mathrm{r})}e^{j\theta_r} = L_1\mathbf{i}_\mathbf{s}^{(\mathrm{r})}e^{j\theta_r} - L_2\overline{\mathbf{i}_\mathbf{s}^{(\mathrm{r})}e^{j\theta_r}}e^{j2\theta_r} + \Psi_f e^{j\theta_r} \tag{2.61}$$

$$\Updownarrow$$

$$\mathbf{v}_\mathbf{s}^{(\mathrm{r})} = R_s\mathbf{i}_\mathbf{s}^{(\mathrm{r})} + \frac{\mathrm{d}\mathbf{\Psi}_\mathbf{s}^{(\mathrm{r})}}{\mathrm{d}t} + j\omega_r\mathbf{\Psi}_\mathbf{s}^{(\mathrm{r})} \tag{2.62}$$

$$\mathbf{\Psi}_\mathbf{s}^{(\mathrm{r})} = L_1\mathbf{i}_\mathbf{s}^{(\mathrm{r})} - L_2\overline{\mathbf{i}_\mathbf{s}^{(\mathrm{r})}} + \Psi_f \tag{2.63}$$

where $\omega_r$ is the electrical angular velocity of the rotor.

We have further, assuming $L_1$ and $L_2$ does not vary in time, substituting (2.63) in (2.62):

$$\begin{aligned}\mathbf{v}_\mathbf{s}^{(\mathrm{r})} &= R_s\mathbf{i}_\mathbf{s}^{(\mathrm{r})} + \frac{\mathrm{d}}{\mathrm{d}t}\left(L_1\mathbf{i}_\mathbf{s}^{(\mathrm{r})} - L_2\overline{\mathbf{i}_\mathbf{s}^{(\mathrm{r})}} + \Psi_f\right) + j\omega_r\left(L_1\mathbf{i}_\mathbf{s}^{(\mathrm{r})} - L_2\overline{\mathbf{i}_\mathbf{s}^{(\mathrm{r})}} + \Psi_f\right) \\ &= R_s\mathbf{i}_\mathbf{s}^{(\mathrm{r})} + L_1\frac{\mathrm{d}\mathbf{i}_\mathbf{s}^{(\mathrm{r})}}{\mathrm{d}t} - L_2\frac{\mathrm{d}\overline{\mathbf{i}_\mathbf{s}^{(\mathrm{r})}}}{\mathrm{d}t} + j\omega_r L_1\mathbf{i}_\mathbf{s}^{(\mathrm{r})} - j\omega_r L_2\overline{\mathbf{i}_\mathbf{s}^{(\mathrm{r})}} + j\omega_r\Psi_f\end{aligned} \tag{2.64}$$

The Cartesian form of (2.64) is given by:

$$v_d + jv_q = R_s(i_d + ji_q) + L_1\frac{\mathrm{d}}{\mathrm{d}t}(i_d + ji_q) - L_2\frac{\mathrm{d}}{\mathrm{d}t}(i_d - ji_q) + j\omega_r L_1(i_d + ji_q) - j\omega_r L_2(i_d - ji_q) + j\omega_r\Psi_f \tag{2.65}$$

Separating the real and imaginary parts of (2.65), we have:

$$v_d = R_s i_d + (L_1 - L_2)\frac{\mathrm{d}i_d}{\mathrm{d}t} - \omega_r(L_1 + L_2)i_q \tag{2.66}$$

$$v_q = R_s i_q + (L_1 + L_2)\frac{\mathrm{d}i_q}{\mathrm{d}t} + \omega_r(L_1 - L_2)i_d + \omega_r\Psi_f \tag{2.67}$$

With:

$$L_d \triangleq L_1 - L_2 \tag{2.68}$$

$$L_q \triangleq L_1 + L_2 \tag{2.69}$$

Eq. (2.66) and (2.67) become:

$$v_d = R_s i_d + L_d\frac{\mathrm{d}i_d}{\mathrm{d}t} - \omega_r L_q i_q \tag{2.70}$$

$$v_q = R_s i_q + L_q\frac{\mathrm{d}i_q}{\mathrm{d}t} + \omega_r L_d i_d + \omega_r\Psi_f \tag{2.71}$$

Eq. (2.70) and (2.71) represent the now-widely utilized d-q model of the PMSM. See, for instance, Harnefors and Nee (1998), Mobarakeh, Meibody-Taba, and Sargos (2000), and Morimoto et al. (2001).

Additionally, from (2.68) and (2.69), we have:

$$L_1 = \frac{L_d + L_q}{2} \tag{2.72}$$

$$L_2 = \frac{L_q - L_d}{2} \tag{2.73}$$

### 2.3.2. Utility of a Complex Representation

One might ask as to why represent the PMSM model in terms of complex-valued space vectors instead of, for instance, the real-valued components of the Clarke transform?

For one thing, when interpreted as vectors in the complex plane, complex numbers provide a compact and, arguably, very convenient form for manipulating the geometry

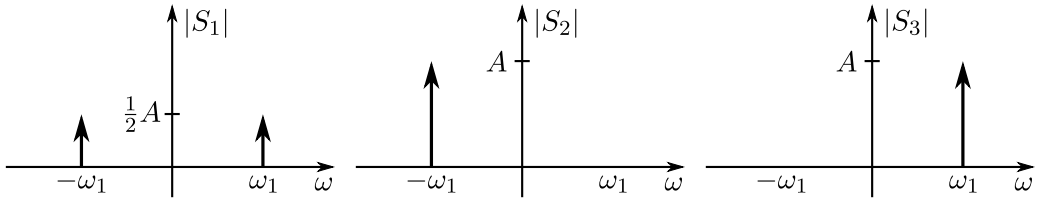


(a) $s_1 = A\cos(\omega_1 t)$ $= \frac{1}{2}A\left(e^{-j\omega_1 t} + e^{j\omega_1 t}\right)$ (b) $s_2 = Ae^{-j\omega_1 t}$ (c) $s_3 = Ae^{j\omega_1 t}$

Figure 2.5.: Examples of magnitude plots of the Fourier transform of real- and complex-valued signals.

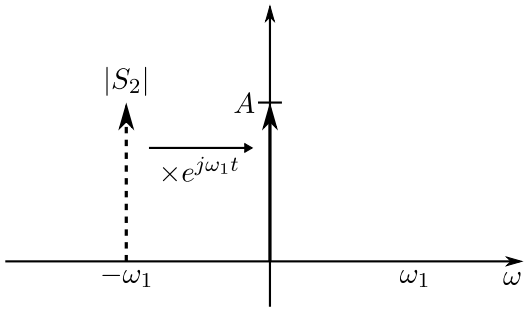


Figure 2.6.: Frequency shifting of the complex signal $s_2 = Ae^{-j\omega_1 t}$.

of vectors. Compare, for instance, the rotation operator in terms of complex and linear algebra[2]:

$$\underbrace{R(\theta) = e^{j\theta}}_{\text{Complex algebra}} \qquad \underbrace{R(\theta) = \begin{bmatrix} \cos(\theta) & -\sin(\theta) \\ \sin(\theta) & \cos(\theta) \end{bmatrix}}_{\text{Linear algebra}} \tag{2.74}$$

The processing of complex-valued signals is also a very well-developed and rich field. The Fourier transform and its discrete counterpart, one of the cornerstones of modern signal processing, is defined for both real- and complex-valued signals. As illustrated with the examples of Figure 2.5, the Fourier transform of a complex signal is not constrained by symmetry. Components at positive frequencies are distinct from those at negative frequencies.

An interesting property of working with complex signals is the ease at which frequency shifting is handled. Multiplying a complex signal by $e^{j\omega_s t}$ shifts the magnitude plot of its Fourier transform by $\omega_s$. If we were interested in determining the amplitude of, for instance, the signal in Figure 2.5b, we could shift it by $\omega_s = \omega_1$:

$$s_2 e^{j\omega_1 t} = Ae^{-j\omega_1 t}e^{j\omega_1 t} = Ae^{j(-\omega_1+\omega_1)t} = Ae^{0t} = A \tag{2.75}$$

[2] $R\boldsymbol{V}$ rotates the point given by the column vector $\boldsymbol{V} \in \mathbb{R}^2$.

Which leaves us with a DC component, as illustrated in Figure 2.6, that is directly proportional to the amplitude $A$ of the signal.

## 2.4. Electromechanical Torque

The instantaneous power supplied to the PMSM is given by:

$$P(t) = v_a i_a + v_b i_b + v_c i_c \tag{2.76}$$

Using the definition in (2.30), it can be readily verified by algebraic expansion that space vectors have the general property:

$$\frac{3}{2}\operatorname{Re}\left(\mathbf{k_1}\overline{\mathbf{k_2}}\right) + 3k_{10}k_{20} = k_{1a}k_{2a} + k_{1b}k_{2b} + k_{1c}k_{2c} \tag{2.77}$$

Thus:

$$P(t) = \frac{3}{2}\operatorname{Re}\left(\mathbf{v_s}\overline{\mathbf{i_s}}\right) + 3v_0 i_0 \tag{2.78}$$

Since the isolated neutral of the PMSM forms the constraint $i_0 = 0$, (2.78) reduces to:

$$P(t) = \frac{3}{2}\operatorname{Re}\left(\mathbf{v_s}\overline{\mathbf{i_s}}\right) = \frac{3}{2}\operatorname{Re}\left(\mathbf{v_s}^{(\mathrm{r})} e^{j\theta_r}\overline{\mathbf{i_s}^{(\mathrm{r})} e^{j\theta_r}}\right) = \frac{3}{2}\operatorname{Re}\left(\mathbf{v_s}^{(\mathrm{r})}\overline{\mathbf{i_s}^{(\mathrm{r})}}\right) \tag{2.79}$$

Substituting (2.62) in (2.79), we have:

$$\begin{aligned} P(t) &= \frac{3}{2}\operatorname{Re}\left[\left(R_s\mathbf{i_s}^{(\mathrm{r})} + \frac{\mathrm{d}\boldsymbol{\Psi}_\mathbf{s}^{(\mathrm{r})}}{\mathrm{d}t} + j\omega_r\boldsymbol{\Psi}_\mathbf{s}^{(\mathrm{r})}\right)\overline{\mathbf{i_s}^{(\mathrm{r})}}\right] \\ &= \frac{3}{2}\operatorname{Re}\left(R_s|\mathbf{i_s}^{(\mathrm{r})}|^2 + \frac{\mathrm{d}\boldsymbol{\Psi}_\mathbf{s}^{(\mathrm{r})}}{\mathrm{d}t}\overline{\mathbf{i_s}^{(\mathrm{r})}} + j\omega_r\boldsymbol{\Psi}_\mathbf{s}^{(\mathrm{r})}\overline{\mathbf{i_s}^{(\mathrm{r})}}\right) \end{aligned} \tag{2.80}$$

The number of ways to derive an expression for the electromechanical torque produced are many and can vary a great deal in terms of complexity[3]. We will derive it qualitatively from (2.80) using a few key observations:

- The PMSM model has:
  - A single loss mechanism in terms of power dissipated in the stator winding resistance. Denote it $P_{\mathrm{res}}$.
  - A single storage mechanism in terms of power supplied to change the energy stored in the magnetic field of the stator. Denote it $P_{\mathrm{mag}}$.

[3] See, for instance, Vas (1992).

- The electromechanical power supplied by the motor, denote it $P_e$, is directly proportional to its angular velocity.

Since energy is a conserved quantity, it follows that:

$$P(t) = P_{\text{res}} + P_{\text{mag}} + P_e \tag{2.81}$$

Based on our observations, we can then decompose (2.80) as:

$$P_{\text{res}} = \frac{3}{2} R_s |\mathbf{i_s}^{(\text{r})}|^2 \tag{2.82}$$

$$P_{\text{mag}} = \frac{3}{2} \operatorname{Re}\left( \frac{\mathrm{d}\boldsymbol{\Psi}_\mathbf{s}^{(\text{r})}}{\mathrm{d}t} \overline{\mathbf{i}_\mathbf{s}^{(\text{r})}} \right) \tag{2.83}$$

$$P_e = \frac{3}{2} \operatorname{Re}\left( j\omega_r \boldsymbol{\Psi}_\mathbf{s}^{(\text{r})} \overline{\mathbf{i}_\mathbf{s}^{(\text{r})}} \right) \tag{2.84}$$

The electromechanical torque produced by the PMSM, denote it $T_e$, is then given by:

$$P_e = \omega_{\text{mech}} T_e = \frac{\omega_r}{n_{pp}} T_e \Leftrightarrow \tag{2.85}$$

$$T_e = \frac{n_{pp}}{\omega_r} P_e = \frac{3}{2} \frac{n_{pp}}{\omega_r} \operatorname{Re}\left( j\omega_r \boldsymbol{\Psi}_\mathbf{s}^{(\text{r})} \overline{\mathbf{i}_\mathbf{s}^{(\text{r})}} \right) = -\frac{3}{2} n_{pp} \operatorname{Im}\left( \boldsymbol{\Psi}_\mathbf{s}^{(\text{r})} \overline{\mathbf{i}_\mathbf{s}^{(\text{r})}} \right) \tag{2.86}$$

where:

- $\omega_{\text{mech}}$ is the mechanical angular velocity of the rotor,
- $n_{pp}$ is the number of pole pairs of the PMSM.

Substituting (2.63) in (2.86):

$$\begin{aligned} T_e &= -\frac{3}{2} n_{pp} \operatorname{Im}\left[ \left( L_1 \mathbf{i}_\mathbf{s}^{(\text{r})} - L_2 \overline{\mathbf{i}_\mathbf{s}^{(\text{r})}} + \Psi_f \right) \overline{\mathbf{i}_\mathbf{s}^{(\text{r})}} \right] \\ &= -\frac{3}{2} n_{pp} \operatorname{Im}\left( L_1 |\mathbf{i}_\mathbf{s}^{(\text{r})}|^2 - L_2 \overline{\mathbf{i}_\mathbf{s}^{(\text{r})}}^2 + \Psi_f \overline{\mathbf{i}_\mathbf{s}^{(\text{r})}} \right) \\ &= \underbrace{\frac{3}{2} n_{pp} L_2 \operatorname{Im}\left( \overline{\mathbf{i}_\mathbf{s}^{(\text{r})}}^2 \right)}_{\text{Reluctance torque}} + \underbrace{\frac{3}{2} n_{pp} \Psi_f \operatorname{Im}\left( \mathbf{i}_\mathbf{s}^{(\text{r})} \right)}_{\text{Interaction torque}} \end{aligned} \tag{2.87}$$

Recall that $L_2$ and $\Psi_f$ represent the peak spatial amplitude of inductance and PM flux linkage, respectively. With no spatial variance in inductance, $L_2 = 0$, and no PM field, $\Psi_f = 0$, the PMSM would develop no reluctance- or interaction torque[4], respectively. Since $L_2$ and $\Psi_f$ appear as a factors in the terms of (2.87), the reluctance and interaction torque components are readily separated, as shown.

[4]Torque produced by the interaction of the rotor field and winding current.

# 3. Hardware Platform

The measurement results presented in this thesis are from experiments performed on the hardware platform that is schematically illustrated in Figure 3.1 and implemented with the products listed in Table 3.1. Motor parameters are given in Table 3.2.

The PMSM is fed from a standard IGBT voltage source inverter with phase currents $i_a$, $i_b$ and $i_c$ and DC-link voltage $V_{\mathrm{DC}}$ measured by isolated current and voltage transducers, respectively. A single-pole RC anti-aliasing filter with cut-off frequency $f_c$ filters these signals and a digital signal processor samples them at a frequency $f_s$, calculates $\mathbf{v_s}$ according to its control algorithm and determines, using space-vector modulation, the duty cycles $d_a$, $d_b$ and $d_c$ required to synthesize it.

$$d'_a = 1 - d_a \tag{3.1a}$$
$$d'_b = 1 - d_b \tag{3.1b}$$
$$d'_c = 1 - d_c \tag{3.1c}$$

The IGBT gate drivers protect against shoot-through by implementing a dead time $T_{\mathrm{DT}}$. The parameters for the hardware platform are listed in Table 3.3.

A schematic of the interconnection of the VSI and the wye-connected motor is shown in Figure 3.2. We have thus:

$$v_a = v_{an} \tag{3.2a}$$
$$v_b = v_{bn} \tag{3.2b}$$
$$v_c = v_{cn} \tag{3.2c}$$

| Product | Vendor | Model |
|---|---|---|
| Voltage source inverter | Danfoss | VLT AutomationDrive FC302 |
| Voltage transducer | LEM | LV 25-P |
| Current transducer | LEM | LA 100-P |
| Digital signal processor | Texas Instruments | TMS320F28335 |
| SMPMSM | Siemens | 1FT6084 |
| SMPMSM | SEM | HR92C4-64S |

Table 3.1.: Hardware platform implementation.

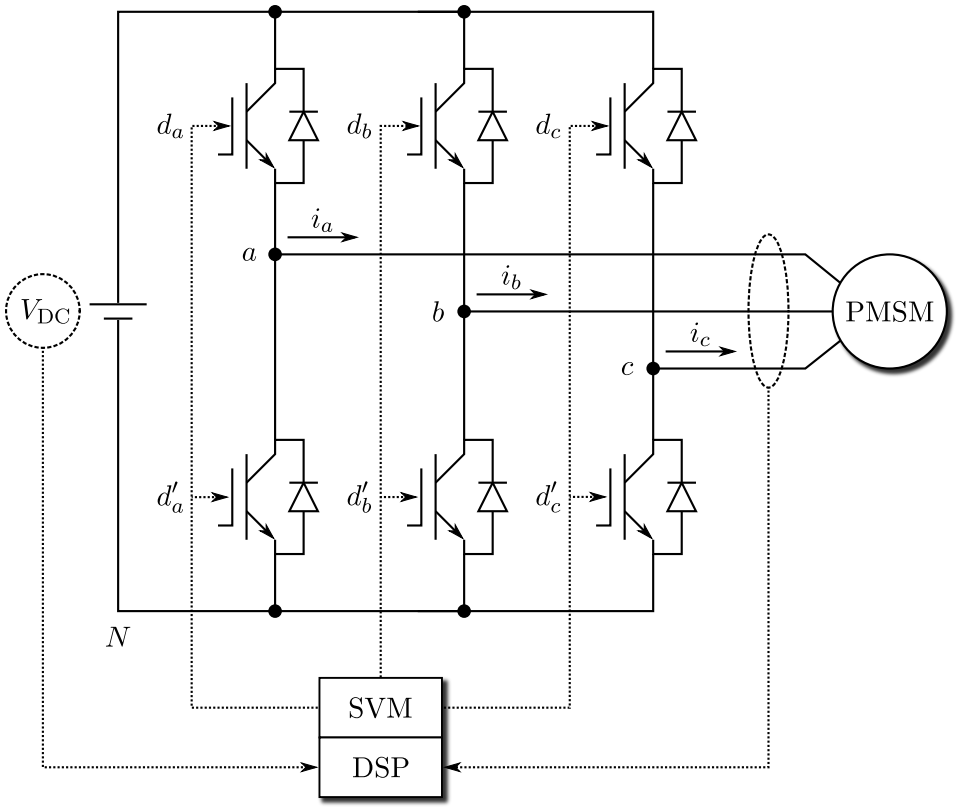


Figure 3.1.: Schematic of hardware platform.

| Parameter | Symbol | Value (Siemens) | Value (SEM) | Unit |
|---|---|---|---|---|
| Rated power | $P_n$ | 9.42 | 0.47 | kW |
| Rated speed | $n_n$ | 4500 | 2850 | RPM |
| Rated torque | $T_n$ | 20 | 1.58 | N m |
| Rated current | $I_n$ | 19.5 | 2.9 | A |
| Stator winding resistance | $R_s$ | 0.18 | 2.35 | Ω |
| Direct-axis inductance | $L_d$ | 2.0 | 10.0 | mH |
| Quadrature-axis inductance | $L_q$ | 2.2 | 15.4 | mH |
| PM flux linkage | $\Psi_f$ | 0.123 | 0.132 | Wb |
| No. of pole pairs | $n_{pp}$ | 4 | 2 | · |

Table 3.2.: Motor parameters.

| Parameter | Symbol | Value | Unit |
|---|---|---|---|
| Filter frequency | $f_c$ | 20 | kHz |
| Switching frequency | $f_s$ | 10 | kHz |
| Inverter dead time | $T_{\mathrm{DT}}$ | 4 | µs |
| Quantization step size | $Q$ | 15.8 | mA/LSB |

Table 3.3.: Hardware platform parameters.

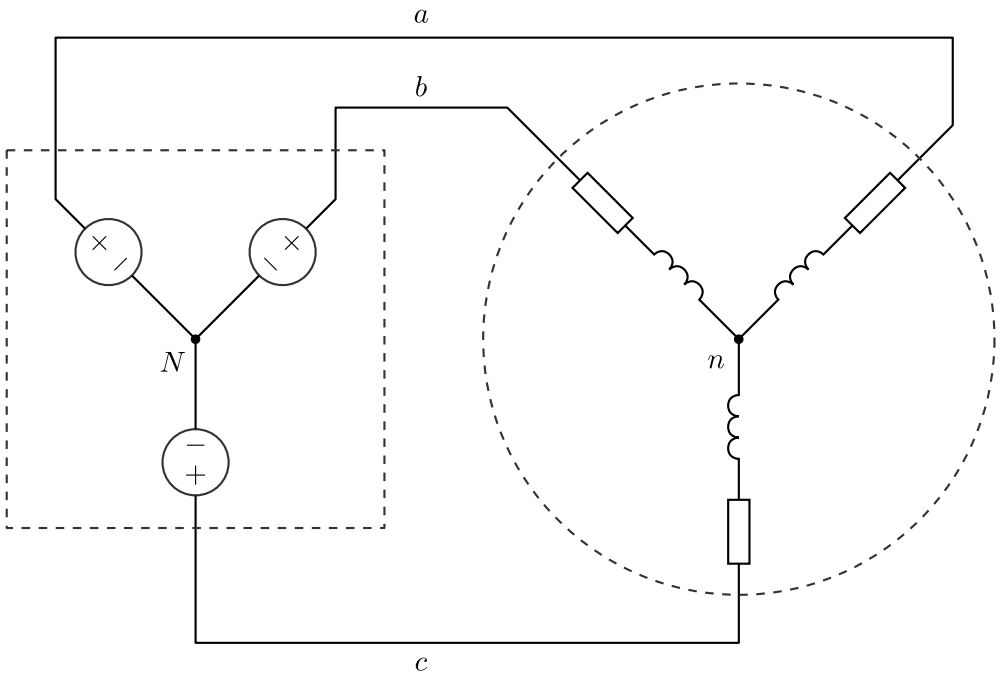


Figure 3.2.: Interconnection of VSI and wye-connected motor.

Further, we have that:

$$v_{aN} = v_{an} + v_{nN} \tag{3.3a}$$
$$v_{bN} = v_{bn} + v_{nN} \tag{3.3b}$$
$$v_{cN} = v_{cn} + v_{nN} \tag{3.3c}$$

Applying the space-vector transformation:

$$\begin{aligned}
\mathbf{v_{pN}} &= v_{aN} + \mathbf{a}v_{bN} + \mathbf{a^2}v_{cN} \\
&= v_{an} + v_{nN} + \mathbf{a}\left(v_{bn} + v_{nN}\right) + \mathbf{a^2}\left(v_{cn} + v_{nN}\right) \\
&= \left(v_{an} + \mathbf{a}v_{bn} + \mathbf{a^2}v_{cn}\right) + \left(v_{nN} + \mathbf{a}v_{nN} + \mathbf{a^2}v_{nN}\right) \\
&= v_{an} + \mathbf{a}v_{bn} + \mathbf{a^2}v_{cn} \\
&= \mathbf{v_s}
\end{aligned} \tag{3.4}$$

since:

$$c + \mathbf{a}c + \mathbf{a^2}c = 0, \quad c \in \mathbb{R} \tag{3.5}$$

From (3.4), we see that, even though we do not directly control the phase voltages $v_a$, $v_b$ and $v_c$, it does not matter since the space vectors $\mathbf{v_{pN}}$ and $\mathbf{v_s}$ can be used interchangeably.

## 3.1. Inverter Voltage Error

Figure 3.3 shows a schematic of a single leg of the inverter and its voltage waveforms for $i_p > 0$ and $i_p < 0$. The schematic includes the capacitance of the IGBT and any snubber as a lumped element. For the case of $i_p > 0$, at:

- $t_1$: $g_L$ goes low and the leg enters dead time. $\mathrm{D_L}$ continues to conduct.
- $t_2$: $g_U$ goes high and $\mathrm{T_U}$ starts conducting, which rapidly charges the lower capacitance through the DC-link.
- $t_3$: $g_U$ goes low and the leg enters dead time again. Now $i_p$ must switch from $\mathrm{T_U}$ to $\mathrm{D_L}$, but $\mathrm{D_L}$ cannot be forward-biased until the lower capacitance is discharged. $i_p$ instead flows through the capacitances and $v_{pN}$ is determined by how quickly the load current can charge/discharge the upper/lower capacitance.
- $t_4$: $g_L$ goes high and $\mathrm{T_L}$ starts conducting, which rapidly charges the upper capacitance through the DC-link.

During the dead time, $v_{pN}$ is thus determined by the load current. If $i_p$ is large in magnitude, the magnitude of the average voltage error introduced by the dead time over a switching period $T_s$ is approximately $\frac{T_{\mathrm{DT}}}{T_s} V_{\mathrm{DC}}$.

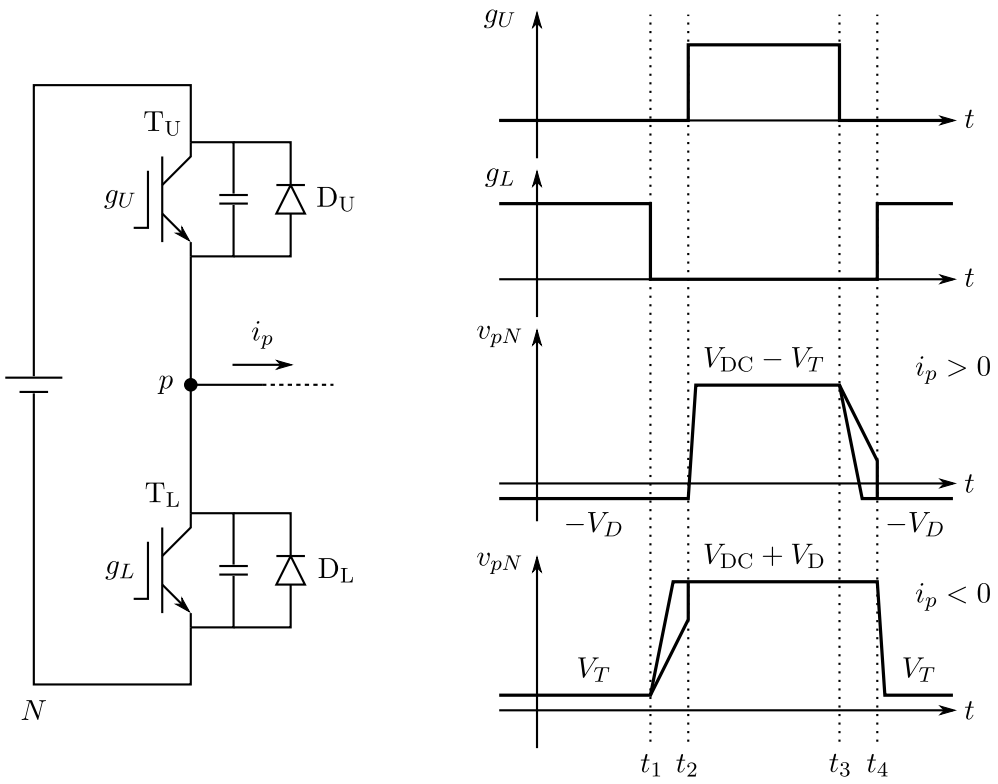


(a) Single leg (b) Switching waveforms

Figure 3.3.: Low-side voltage of a single inverter leg.

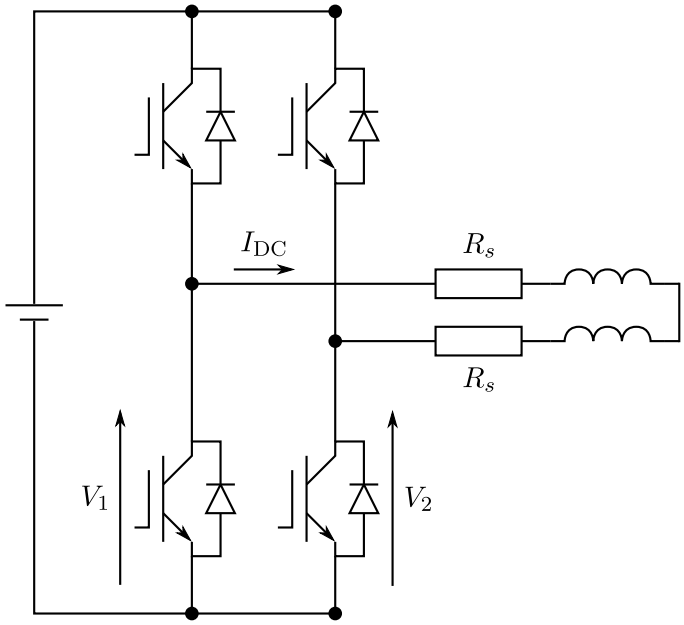


Figure 3.4.: Configuration for measuring the inverter voltage error.

### 3.1.1. Measuring the Voltage Error

Consider the configuration in Figure 3.4, where two phases of the PMSM is connected between two legs of the VSI. For a DC current $I_{\mathrm{DC}}$, we have:

$$\langle V_1 \rangle = 2R_s I_{\mathrm{DC}} + \langle V_2 \rangle \tag{3.6}$$

where $\langle V_1 \rangle$ and $\langle V_2 \rangle$ are the average values of $V_1$ and $V_2$, respectively.

The inverter voltage error can then be characterized offline with the procedure:

1. Fix the duty cycle of the left leg.
2. Adjust the duty cycle of the right leg until $I_{\mathrm{DC}}$ is at its target value.
3. Measure $\langle V_1 \rangle$ with the DC-link voltage transducer[1].
4. Iterate as required.

[1]The bandwidth of the sensor is not a concern since it just has to pass the DC-component of $V_1$ at unity gain.

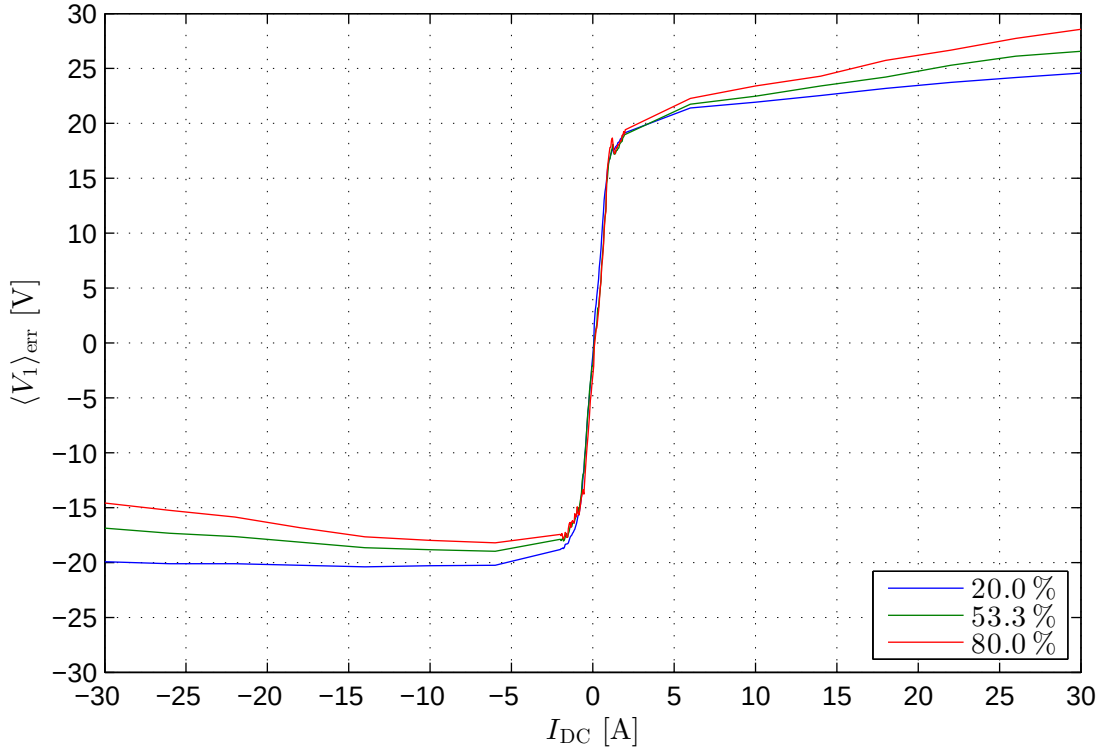


Figure 3.5.: Map of the inverter voltage error for a selection of duty cycles.

### 3.1.2. Measurement Results

If we define the voltage error as:

$$\langle V_1 \rangle_{\mathrm{err}} = \langle V_1 \rangle^* - \langle V_1 \rangle \tag{3.7}$$

where $\langle V_1 \rangle^*$ is the reference value of $V_1$.

Figure 3.5 shows the result of automating the procedure of Section 3.1.1 for the Siemens motor. For currents below approximately 1 A, the inverter has the property that its voltage error is directly proportional to the load current. In this current range, the inverter effectively acts as a voltage source with a large internal resistance. The slope of $\langle V_1 \rangle_{\mathrm{err}}$ gives it a value of approximately 17.5 Ω.

# 4. High-Frequency Voltage Injection

Recall the space-vector representation of the PMSM model:

$$\mathbf{v_s} = R_s \mathbf{i_s} + \frac{\mathrm{d}\boldsymbol{\Psi_s}}{\mathrm{d}t} \qquad \text{(2.57 revisited)}$$

$$\boldsymbol{\Psi_s} = L_1 \mathbf{i_s} - L_2 \overline{\mathbf{i_s}} e^{j2\theta_r} + \Psi_f e^{j\theta_r} \qquad \text{(2.58 revisited)}$$

Substituting (2.58) in (2.57), we have:

$$\begin{aligned} \mathbf{v_s} &= R_s \mathbf{i_s} + \frac{\mathrm{d}}{\mathrm{d}t}\Big( L_1 \mathbf{i_s} - L_2 \overline{\mathbf{i_s}} e^{j2\theta_r} + \Psi_f e^{j\theta_r} \Big) \\ &= R_s \mathbf{i_s} + \frac{\mathrm{d}}{\mathrm{d}t}(L_1 \mathbf{i_s}) - \underbrace{\frac{\mathrm{d}}{\mathrm{d}t}\big(L_2 \overline{\mathbf{i_s}}\big)\, e^{j2\theta_r}}_{(1)} - \underbrace{j2\omega_r L_2 \overline{\mathbf{i_s}} e^{j2\theta_r}}_{(2)} + \underbrace{j\omega_r \Psi_f e^{j\theta_r}}_{(3)} \end{aligned} \qquad (4.1)$$

If we are interested in determining the angular position $\theta_r$ of the rotor without direct feedback, the terms (1), (2) and (3) in (4.1) are of particular interest. For low-speed operation, the terms (2) and (3) present us a problem, though, since they are directly proportional to the angular velocity of the rotor $\omega_r$. We can then assume, if we are interested in continued operation down to zero angular velocity, that the signal-to-noise ratio of estimating $\theta_r$ from terms (2) and (3) will, at some point, become too low to yield valid results. We are then left with term (1) as our basis for robustly estimating $\theta_r$ when operating from low speed to standstill. The dependence of term (1) on $L_2$ suggests that it is the spatial variation in inductance, introduced by the magnetic field of the rotor, that allows us to estimate its angular position.

For low-speed operation, we will consider terms (2) and (3) in (4.1) to be of negligible magnitude due to their scaling by $\omega_r$. $L_2$ is also generally small in magnitude for a SMPMSM. We can then instead work with the low-speed model:

$$\mathbf{v_s} = \underbrace{R_s \mathbf{i_s}}_{(1)} + \underbrace{\frac{\mathrm{d}}{\mathrm{d}t}(L_1 \mathbf{i_s})}_{(2)} - \underbrace{\frac{\mathrm{d}}{\mathrm{d}t}\big(L_2 \overline{\mathbf{i_s}}\big)\, e^{j2\theta_r}}_{(3)} \qquad (4.2)$$

## 4.1. High-Frequency Model

With the low-speed model (4.2) in hand, it becomes a question of how to extract $\theta_r$ from it. A useful strategy relies on a further simplification:

Let us make sure that terms (2) and (3) in (4.2) are large in magnitude compared to term (1). Consider the case of:

$$\mathbf{v_s} = \mathbf{v_c} = V_c e^{j(\omega_c t + \phi_m)} \tag{4.3}$$

where $\phi_m$ is the possible phase shift introduced by modulation[1].

For pulse-width modulation, the fundamental is delayed by half a switching period. Assuming use of a digital control system, we can additionally factor in the update delay of its output, which we will consider to be limited to one sample period. For synchronous sampling, we have then:

$$\frac{T_s/2 + T_s}{T_c} = \frac{\phi_m}{2\pi} \Leftrightarrow \phi_m = 3\pi\frac{T_s}{T_c} = 3\pi\frac{f_c}{f_s} \tag{4.4}$$

where:

- $T_c$ and $f_c$ is the period and frequency of $\mathbf{v_c}$, respectively.
- $T_s$ and $f_s$ is the switching period and frequency, respectively.

If we were to make $\mathbf{v_c}$ rotate with a very high frequency $\omega_c$, intuitively, we would expect the machine to respond with a very high-frequency current $\mathbf{i_c}$. We should thus be able to make the sum of terms (2) and (3) in (4.2) approximately equal the applied voltage $\mathbf{v_c}$ by assuring that $\omega_c$ is sufficiently high in value. How high exactly depends on machine parameters, but for now we will simply consider term (1) in (4.2) to be of negligible magnitude. The effect of the stator winding resistance $R_s$ will be treated in Section 4.4.

By injecting the high-frequency voltage $\mathbf{v_c}$, (4.2) then simplifies to the high-frequency model:

$$\mathbf{v_c} = \frac{\mathrm{d}}{\mathrm{d}t}(L_1\mathbf{i_c}) - \frac{\mathrm{d}}{\mathrm{d}t}\left(L_2\overline{\mathbf{i_c}}\right)e^{j2\theta_r} \tag{4.5}$$

The subscript $c$ refers to *carrier*, which stems from a telecommunications viewpoint that a voltage carrier signal $\mathbf{v_c}$ is modulated by the machine itself and measured as the current $\mathbf{i_c}$.

Eq. (4.5) gives us a simplified model to work with, but it does not directly allow us any way to extract $\theta_r$. Thankfully, (4.5) is a relatively simple differential equation to solve,

[1] The phase shift of, for instance, an anti-aliasing filter, if significant, should be included in $\phi_m$.

so we do have the means to determine the current response to an applied high-frequency voltage. Note that the following derivation applies whether $L_1$ and $L_2$ are constant or vary in time.

Define:

$$\boldsymbol{\Psi}_{\mathbf{si}} \triangleq L_1 \mathbf{i}_{\mathbf{c}} + L_2 \overline{\mathbf{i}_{\mathbf{c}}} e^{j2\theta_r} \tag{4.6}$$

Since $\theta_r$ varies very slowly at low speed, we will consider the variable to be constant in time, so we have:

$$\int \mathbf{v}_{\mathbf{c}} \, \mathrm{d}t = \frac{V_c}{j\omega_c} e^{j(\omega_c t + \phi_m)} = \boldsymbol{\Psi}_{\mathbf{si}} + C \tag{4.7}$$

where $C$ is a constant of integration.

We can further express (4.6) as:

$$\begin{aligned}
\boldsymbol{\Psi}_{\mathbf{si}} &= L_1 \mathbf{i}_{\mathbf{c}} + L_2 \overline{\mathbf{i}_{\mathbf{c}}} e^{j2\theta_r} \\
&= L_1 (i_\alpha + j i_\beta) + L_2 (i_\alpha - j i_\beta) \left[ \mathrm{Re}\left(e^{j2\theta_r}\right) + j \, \mathrm{Im}\left(e^{j2\theta_r}\right) \right] \\
&= \left[ L_1 - L_2 \, \mathrm{Re}\left(e^{j2\theta_r}\right) \right] i_\alpha - L_2 \, \mathrm{Im}\left(e^{j2\theta_r}\right) i_\beta \\
&\quad - j L_2 \, \mathrm{Im}\left(e^{j2\theta_r}\right) i_\alpha + j \left[ L_1 + L_2 \, \mathrm{Re}\left(e^{j2\theta_r}\right) \right] i_\beta
\end{aligned} \tag{4.8}$$

Separating the real and imaginary parts of (4.8), we have:

$$\begin{aligned}
\mathrm{Re}(\boldsymbol{\Psi}_{\mathbf{si}}) &= \frac{1}{2} \left( \boldsymbol{\Psi}_{\mathbf{si}} + \overline{\boldsymbol{\Psi}_{\mathbf{si}}} \right) \\
&= \left[ L_1 - L_2 \, \mathrm{Re}\left(e^{j2\theta_r}\right) \right] i_\alpha - L_2 \, \mathrm{Im}\left(e^{j2\theta_r}\right) i_\beta \\
&= \left[ L_1 - \frac{L_2}{2} \left( e^{j2\theta_r} + e^{-j2\theta_r} \right) \right] i_\alpha - \frac{L_2}{2} \left( e^{j2\theta_r} - e^{-j2\theta_r} \right) i_\beta
\end{aligned} \tag{4.9}$$

$$\begin{aligned}
\mathrm{Im}(\boldsymbol{\Psi}_{\mathbf{si}}) &= \frac{1}{j2} \left( \boldsymbol{\Psi}_{\mathbf{si}} - \overline{\boldsymbol{\Psi}_{\mathbf{si}}} \right) \\
&= -L_2 \, \mathrm{Im}\left(e^{j2\theta_r}\right) i_\alpha + \left[ L_1 + L_2 \, \mathrm{Re}\left(e^{j2\theta_r}\right) \right] i_\beta \\
&= -\frac{L_2}{2} \left( e^{j2\theta_r} - e^{-j2\theta_r} \right) i_\alpha + \left[ L_1 + \frac{L_2}{2} \left( e^{j2\theta_r} + e^{-j2\theta_r} \right) \right] i_\beta
\end{aligned} \tag{4.10}$$

The system of (4.9) and (4.10) is solved in terms of $i_\alpha$ and $i_\beta$ by:

$$i_\alpha = \frac{1}{2} \frac{1}{L_1^2 - L_2^2} \left( L_1 \boldsymbol{\Psi}_{\mathbf{si}} + L_2 \overline{\boldsymbol{\Psi}_{\mathbf{si}}} e^{j2\theta_r} + L_1 \overline{\boldsymbol{\Psi}_{\mathbf{si}}} + L_2 \boldsymbol{\Psi}_{\mathbf{si}} e^{-j2\theta_r} \right) \tag{4.11}$$

$$i_\beta = \frac{1}{j2} \frac{1}{L_1^2 - L_2^2} \left( L_1 \boldsymbol{\Psi}_{\mathbf{si}} + L_2 \overline{\boldsymbol{\Psi}_{\mathbf{si}}} e^{j2\theta_r} - L_1 \overline{\boldsymbol{\Psi}_{\mathbf{si}}} - L_2 \boldsymbol{\Psi}_{\mathbf{si}} e^{-j2\theta_r} \right) \tag{4.12}$$

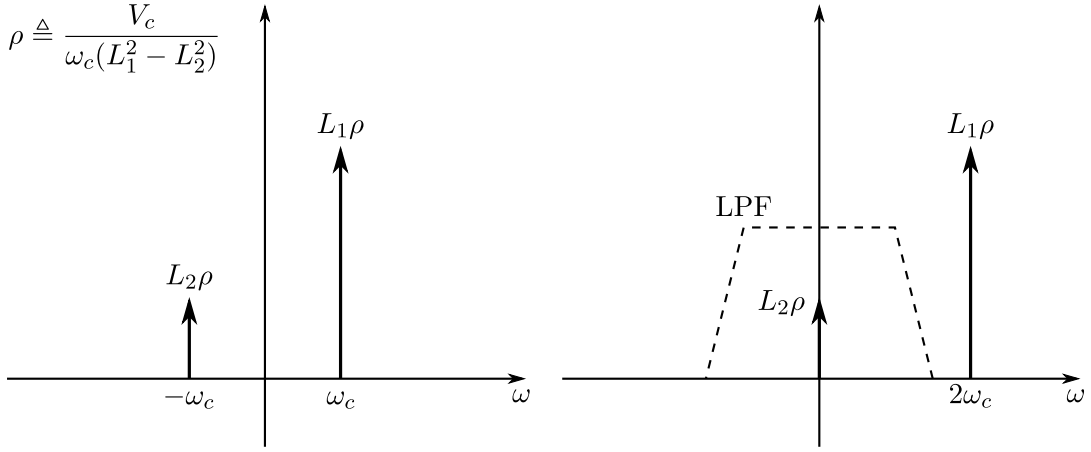


(a) Magnitude spectrum of $\mathbf{i_c}$ (b) Magnitude spectrum of $\mathbf{i_c}e^{j\omega_c t}$

Figure 4.1.: Signal processing of current response $\mathbf{i_c}$ to voltage $\mathbf{v_c}$.

We have then:

$$\begin{aligned}
\mathbf{i_c} &= i_\alpha + j i_\beta \\
&= \frac{1}{2}\frac{1}{L_1^2 - L_2^2}\left(L_1\mathbf{\Psi_{si}} + L_2\overline{\mathbf{\Psi_{si}}}e^{j2\theta_r} + L_1\overline{\mathbf{\Psi_{si}}} + L_2\mathbf{\Psi_{si}}e^{-j2\theta_r}\right) \\
&\quad + \frac{1}{2}\frac{1}{L_1^2 - L_2^2}\left(L_1\mathbf{\Psi_{si}} + L_2\overline{\mathbf{\Psi_{si}}}e^{j2\theta_r} - L_1\overline{\mathbf{\Psi_{si}}} - L_2\mathbf{\Psi_{si}}e^{-j2\theta_r}\right) \\
&= \frac{1}{L_1^2 - L_2^2}\left(L_1\mathbf{\Psi_{si}} + L_2\overline{\mathbf{\Psi_{si}}}e^{j2\theta_r}\right)
\end{aligned} \tag{4.13}$$

Substituting (4.7) in (4.13) with $C = 0$:

$$\begin{aligned}
\mathbf{i_c} &= \frac{1}{L_1^2 - L_2^2}\left[L_1\left(\frac{V_c}{j\omega_c}e^{j(\omega_c t + \phi_m)}\right) + L_2\overline{\frac{V_c}{j\omega_c}e^{j(\omega_c t + \phi_m)}}e^{j2\theta_r}\right] \\
&= \frac{V_c}{j\omega_c(L_1^2 - L_2^2)}\left[L_1 e^{j(\omega_c t + \phi_m)} - L_2 e^{j(-\omega_c t - \phi_m + 2\theta_r)}\right]
\end{aligned} \tag{4.14}$$

With (4.14) we have determined the current response $\mathbf{i_c}$ to the applied high-frequency voltage $\mathbf{v_c}$. We see that the complex signal $\mathbf{i_c}$ has frequency components at $-\omega_c$ and $\omega_c$, which is illustrated in Figure 4.1a.

If the objective is to extract $\theta_r$, the component at $-\omega_c$ is of particular interest. We are specifically interested in determining the phase of this component. Shifting the magnitude spectrum of $\mathbf{i_c}$ by $\omega_c$:

$$\begin{aligned}\mathbf{i_c}e^{j\omega_c t} &= \frac{V_c}{j\omega_c(L_1^2 - L_2^2)}\left[L_1 e^{j(\omega_c t+\phi_m)} - L_2 e^{j(-\omega_c t-\phi_m+2\theta_r)}\right] e^{j\omega_c t} \\ &= \frac{V_c}{j\omega_c(L_1^2 - L_2^2)}\left[L_1 e^{j(2\omega_c t+\phi_m)} - L_2 e^{j(-\phi_m+2\theta_r)}\right] \end{aligned} \tag{4.15}$$

we are left with frequency components at DC and $2\omega_c$, which is illustrated in Figure 4.1b. The component at DC encodes $\theta_r$ in its phase and is readily separated with a linear low-pass filter:

$$\mathrm{LPF}\big(\mathbf{i_c}e^{j\omega_c t}\big) = -\frac{V_c L_2}{j\omega_c(L_1^2 - L_2^2)} e^{j(-\phi_m+2\theta_r)} = j\frac{V_c L_2}{\omega_c(L_1^2 - L_2^2)} e^{j(-\phi_m+2\theta_r)} \tag{4.16}$$

We have then:

$$\arg\Big[\mathrm{LPF}\big(\mathbf{i_c}e^{j\omega_c t}\big)\Big] = -\phi_m + 2\theta_r + 90^\circ \Leftrightarrow \tag{4.17}$$

$$\theta_r = \frac{1}{2}\left(\arg\Big[\mathrm{LPF}\big(\mathbf{i_c}e^{j\omega_c t}\big)\Big] + \phi_m - 90^\circ\right) \tag{4.18}$$

where arg gives the principal value with range $[-180^\circ; 180^\circ]$[2].

## 4.2. Four-Quadrant Estimation of Rotor Position

From (4.18), we see that:

$$\theta_r \in [-135^\circ + \frac{1}{2}\phi_m; 45^\circ + \frac{1}{2}\phi_m] \tag{4.19}$$

Which gives $\theta_r$ a two-quadrant span of 180°. We can interpret this as the ability of the algorithm to estimate the position of the magnetic axis of the rotor but not the polarity of its field. Consider, for instance, the example given in Figure 4.2: It is the spatial variation in inductance, produced by saturation of the stator iron by the PM flux, that provides us with information on the angular position of the rotor. Since the PM flux saturates the stator iron equally in Figures 4.2a and 4.2b, we have no basis for determining the polarity of the PM field. This poses a problem, since $\theta_r$ at a time $t$ and $t + \delta t$ might give opposite directions for the PM field, which, in the case of FOC, would case the torque control loop to reverse in direction.

The ambiguity of $\theta_r$ is illustrated in Figure 4.3. In order to avoid a reversal of polarity, we must somehow extend the range of tracking to all four quadrants. Let $\theta_r^{4q}$ denote a version capable of four-quadrant operation.

[2] A complex number $z = a + jb$ is commonly stored in Cartesian form in computer memory with $\arg(z) = \mathrm{atan2}(b, a)$. The return value of atan2 in, for instance, the C and C++ standard libraries is the principal value with range $[-\pi; \pi]$.

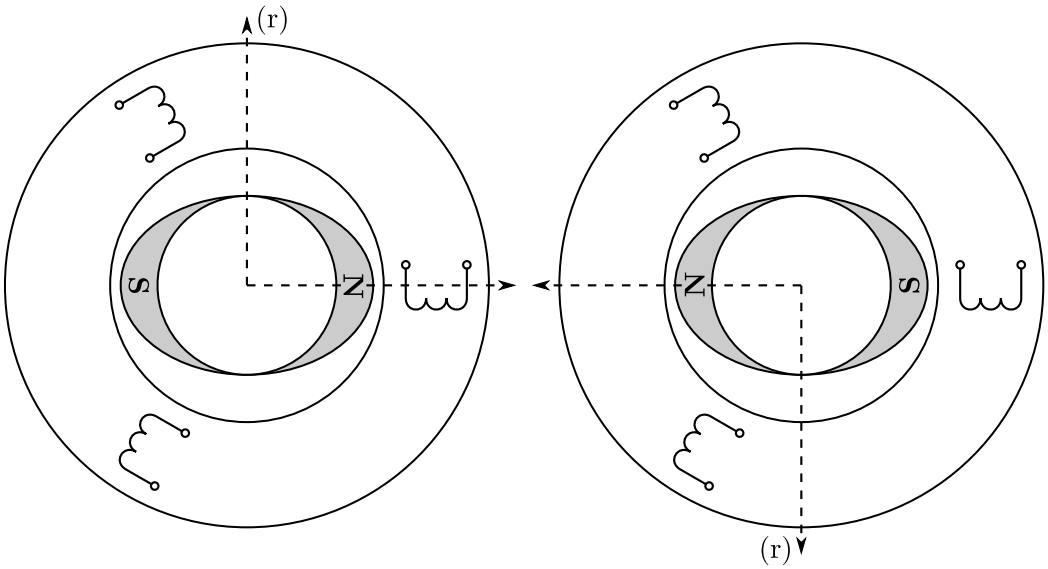


(a) $\theta_r = 0°$ (b) $\theta_r = 180°$

Figure 4.2.: Examples of magnetically identical systems in terms of saturation of the stator iron by the PM flux.

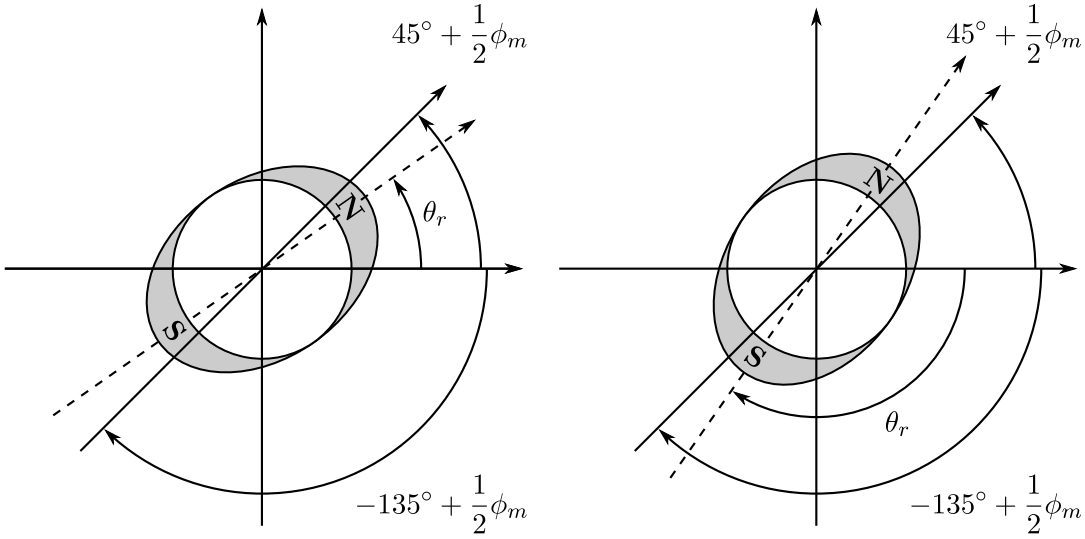


Figure 4.3.: Example of how $\theta_r$ tracks the magnetic axis of the PM field but not its polarity.

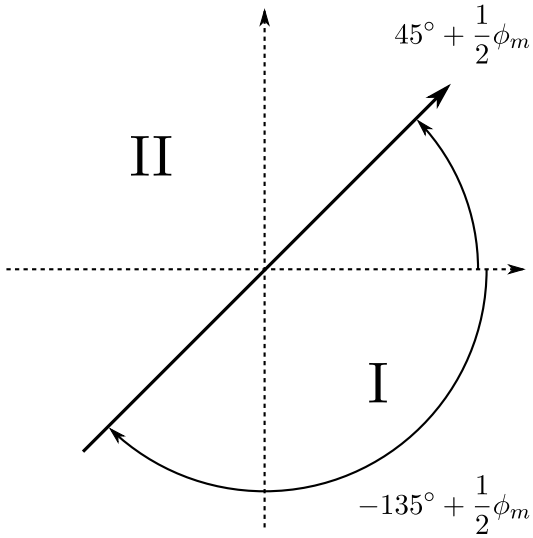


Figure 4.4.: Subdivision of the range of $\theta_r^{4q}$ into 180° sectors I and II.

$\theta_r$ is limited by (4.19), but if we keep track of its state from sample to sample, we can detect any large difference in value of $\theta_r(t)$ and $\theta_r(t - T_s)$. If we subdivide the plane as shown in Figure 4.4, such a signal would indicate a change of sector for $\theta_r^{4q}$. If $|\theta_r(t) - \theta_r(t - T_s)| > 90°$, it would be highly unlikely for the actual position of the rotor, from one sample to the next, to have changed by more than 90°. Such a change would require a very low sampling frequency and/or a very high angular rotor velocity.

With this in mind, Algorithm 1 implements a very simple state machine to monitor sector transitions and calculate $\theta_r^{4q}$ accordingly, thus effectively extending the range of tracking to all four quadrants. It does, however, require a choice of sector to initialize with, since the estimation algorithm has no intrinsic knowledge of the polarity of the PM field.

## 4.3. Polarity Detection of PM Field

With an initial estimate from (4.18) of the angular position of the PM field axis, denote it $\hat{\theta}_r$, a relatively simple strategy to determine its polarity relies on purposefully driving the iron of the machine into deep saturation.

Consider the example shown in Figure 4.5: Voltage pulses are sequenced in diametrically opposite directions on the estimated rotor axis. Since the machine is already partially saturated along this path by the PM flux, driving current in the same direction as the PM field can fully saturate the machine, thus decreasing its inductance significantly (Lu et al. 2010). However, driving current in the opposite direction of the PM field can bring the machine fully out of saturation, thus increasing its inductance. Assuming the

**Algorithm 1** Calculate the four-quadrant angular position of the rotor

**Require:** Initialize sector to the correct PM field polarity
**Ensure:** Four-quadrant position is given by $\theta_r^{4q}$

```
if |θ_r(t) − θ_r(t − T_s)| > 90° then
    if sector = I then
        sector ← II
    else
        sector ← I
    end if
end if
if sector = I then
    θ_r^{4q}(t) = θ_r(t)
else
    θ_r^{4q}(t) = θ_r(t) + 180°
end if
```

resulting current pulses are large enough in magnitude to impact the saturation level of the machine[3], their peak magnitudes should show a significant difference (Holtz 2008), as illustrated in Figure 4.6. Whichever current pulse has the largest peak magnitude corresponds to the voltage pulse with the same direction as the PM field.

Combining the estimate $\hat{\theta}_r$, the state machine to determine $\hat{\theta}_r^{4q}$, polarity detection and a FOC topology yields the algorithm shown in Figure 4.7. The lower section depicts the estimation part, which ultimate goal is to determine $\hat{\theta}_r^{4q}$ in order of:

1. Calculate an estimate $\hat{\theta}_r$ from (4.18).

2. If uninitialized, detect field polarity by voltage pulse injection. Skip otherwise.

3. Process Algorithm 1 to determine $\hat{\theta}_r^{4q}$.

The top section is a standard FOC topology with a few alterations to accommodate the high-frequency voltage injection:

- A low-pass filter separates the fundamental machine current $\mathbf{i_f}$ from the high-frequency carrier signal.

- The high-frequency voltage $\mathbf{v_c}$ is added to the fundamental component $\mathbf{v_f}$.

- The bandwidth of the current controller must be below the frequency of $\mathbf{v_c}$.

[3]Current magnitudes several times the rated value of the machine are commonly used. Care should be taken not to surpass the demagnetization current of the permanent magnets.

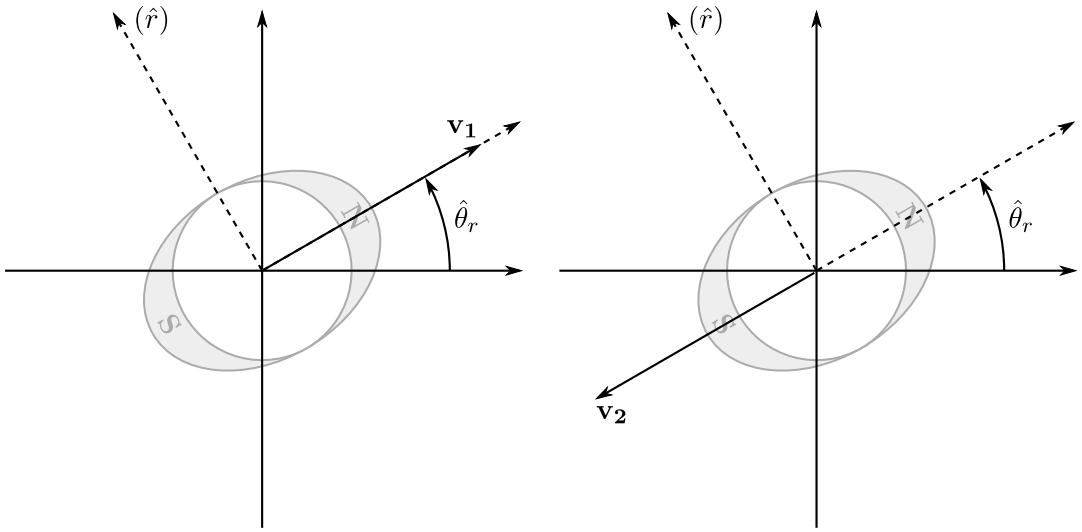


(a) $\mathbf{v_1} = |\mathbf{v_1}|e^{j\hat{\theta}_r}$ (b) $\mathbf{v_2} = -\mathbf{v_1} = |\mathbf{v_1}|e^{j(\hat{\theta}_r+180°)}$

Figure 4.5.: Injection of voltage pulses on estimated rotor axis.

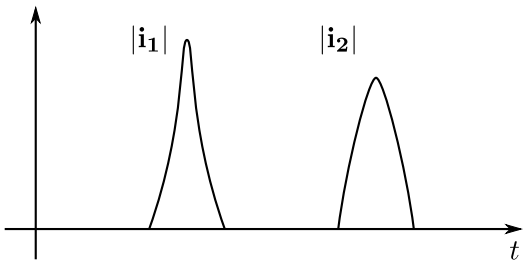


Figure 4.6.: Current response to injection of voltage pulses on estimated rotor axis as shown in Figure 4.5.

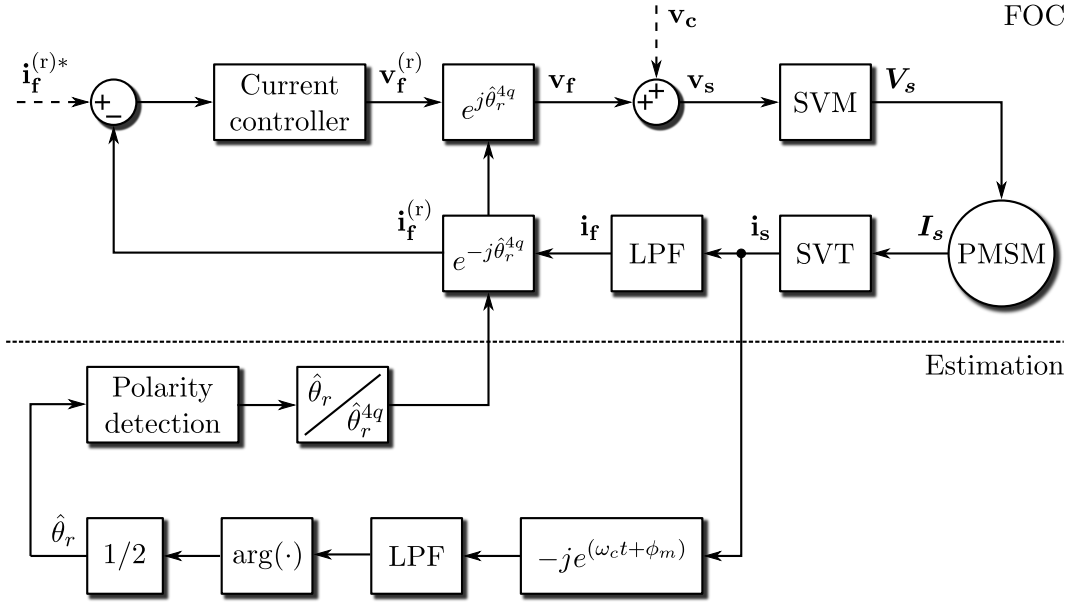


Figure 4.7.: Complete topology of the high-frequency voltage injection algorithm.

## 4.4. Effect of Stator Winding Resistance

If we are to evaluate the effect the stator resistance has on the current response $\mathbf{i_c^{R4}}$ to an applied high-frequency voltage $\mathbf{v_c}$, we must, instead of the high-frequency model (4.5), work directly with the low-speed model (4.2):

$$\mathbf{v_c} = V_c e^{j(\omega_c t+\phi_m)} = R_s \mathbf{i_c^R} + \frac{\mathrm{d}}{\mathrm{d}t}\left(L_1 \mathbf{i_c^R}\right) - \frac{\mathrm{d}}{\mathrm{d}t}\left(L_2 \overline{\mathbf{i_c^R}}\right) e^{j2\theta_r} \tag{4.20}$$

Under the assumption that $L_1$, $L_2$ and $\theta_r$ are constant in time, (4.20) can be expressed in Cartesian form as:

$$V_c \cos(\omega_c t + \phi_m) = R_s i_\alpha^{\mathrm{R}} + \left[L_1 - \cos(2\theta_r) L_2\right] \frac{\mathrm{d}i_\alpha^{\mathrm{R}}}{\mathrm{d}t} - \sin(2\theta_r) L_2 \frac{\mathrm{d}i_\beta^{\mathrm{R}}}{\mathrm{d}t} \tag{4.21}$$

$$V_c \sin(\omega_c t + \phi_m) = R_s i_\beta^{\mathrm{R}} + \left[L_1 + \cos(2\theta_r) L_2\right] \frac{\mathrm{d}i_\beta^{\mathrm{R}}}{\mathrm{d}t} - \sin(2\theta_r) L_2 \frac{\mathrm{d}i_\alpha^{\mathrm{R}}}{\mathrm{d}t} \tag{4.22}$$

Eq. (4.21) and (4.22) is a system of coupled linear differential equations that, while solvable, is very cumbersome. Its general solution is extensive and is better suited for

[4] The superscript R is to remind us that $\mathbf{i_c^R}$ is a solution to a system that takes into account the effect of stator resistance. Not to be confused with the superscript (r), which denotes a rotor-fixed reference frame.

the algorithmic engine of a computer algebra system. Its steady-state, zero-state solution is thus given here in complex form without proof[5]:

$$\mathbf{i}_\mathbf{c}^\mathrm{R} = \kappa \left[ z_1 e^{j(\omega_c t + \phi_m)} + z_2 e^{j(-\omega_c t - \phi_m + 2\theta_r)} \right] \tag{4.23}$$

where:

$$\kappa = \frac{V_c}{\left[R_s^2 + \omega_c^2 (L_1 + L_2)^2\right]\left[R_s^2 + \omega_c^2 (L_1 - L_2)^2\right]} \tag{4.24}$$

$$z_1 = R_s^3 + R_s \omega_c^2 L_1^2 + R_s \omega_c^2 L_2^2 + j\left(L_1 L_2^2 \omega_c^3 - \omega_c^3 L_1^3 - \omega_c L_1 R_s^2\right) \tag{4.25}$$

$$z_2 = \omega_c L_2 \left[ 2\omega_c L_1 R_s + j(\omega_c^2 L_1^2 - \omega_c^2 L_2^2 - R_s^2) \right] \tag{4.26}$$

Substituting (4.23) in (4.20) verifies it as a solution, and it is worth noting that (4.23) reduces to (4.14) for $R_s = 0$.

As in Section 4.1, the current $\mathbf{i}_\mathbf{c}^\mathrm{R}$ is frequency shifted and low-pass filtered:

$$\mathrm{LPF}\left(\mathbf{i}_\mathbf{c}^\mathrm{R} e^{j\omega_c t}\right) = \kappa z_2 e^{j(-\phi_m + 2\theta_r)} \tag{4.27}$$

Since $\kappa \in \mathbb{R}, z_2 \in \mathbb{C}$, we have:

$$\arg\left[\mathrm{LPF}\left(\mathbf{i}_\mathbf{c}^\mathrm{R} e^{j\omega_c t}\right)\right] = -\phi_m + 2\theta_r + \arg(z_2) \tag{4.28}$$

Let us instead express (4.28) as:

$$\arg\left[\mathrm{LPF}\left(\mathbf{i}_\mathbf{c}^\mathrm{R} e^{j\omega_c t}\right)\right] = -\phi_m + 2\theta_r + 90^\circ - 2\phi_R \tag{4.29}$$

where:

$$\phi_R = \frac{1}{2}\left[90^\circ - \arg(z_2)\right] \tag{4.30}$$

From (4.29), we have:

$$\theta_r - \phi_R = \frac{1}{2}\left(\arg\left[\mathrm{LPF}\left(\mathbf{i}_\mathbf{c}^\mathrm{R} e^{j\omega_c t}\right)\right] + \phi_m - 90^\circ\right) \tag{4.31}$$

Compare (4.31) to (4.18):

$$\theta_r = \frac{1}{2}\left(\arg\left[\mathrm{LPF}(\mathbf{i}_\mathbf{c} e^{j\omega_c t})\right] + \phi_m - 90^\circ\right) \qquad \text{(4.18 revisited)}$$

[5] A Maple v17.00 worksheet detailing the solution is included as Supplement 1.

We see, then, that the effect of stator winding resistance is to introduce an estimation error $\phi_R$.

Increasing $L_2$ in (4.26) decreases $\mathrm{Im}(z_2)$, decreasing $\arg(z_2)$, which in turn increases $\phi_R$. For a SMPMSM, a saliency ratio above $L_q/L_d = 3/2$ is somewhat atypical, so we will use this as a worst-case condition. For a selection of injection frequencies $f_c$ and machine inductances $L_q$, Figure 4.8 then shows plots of $\phi_R$ as a function of stator resistance $R_s$.

For a machine with $R_s < 5\,\Omega$, an injection frequency of $f_c = 500\,\mathrm{Hz}$ or above is recommended if $\phi_R$ is to remain uncompensated. Adding a nominal value of $\phi_R$ to (4.31) can reduce the estimation error significantly but naturally requires knowledge of machine parameters.

In general, (4.30) should be used to characterize $\phi_R$ for the machine in question.

## 4.5. Measurement Results

The results of Section 3.1.2 showed that the inverter has a linear range of operation below approximately 1 A, where the inverter voltage error is well-modeled as the voltage drop across an additional resistance in series with the stator winding resistance. As a way to validate the results of this chapter, we will initially run the inverter in its linear range as to minimize the impact of the inverter voltage error. Additionally, for the results presented in this section, no load current $\mathbf{i_f}$ is present in the machine.

### 4.5.1. Linear Inverter Range

Operating the inverter in its linear range has the consequence of effectively increasing the stator winding resistance $R_s$ to approximately $17.5\,\Omega$. Since the effect of resistance is to introduce an estimation error $\phi_R$, we should expect $\phi_R$ to increase accordingly. For a selection of injection frequencies $f_c$, Figure 4.9 shows a plot of $\phi_R$ as a function of stator resistance $R_s$ for the Siemens motor specifications listed in Table 3.2.

Recall the solution to the low-speed model (4.20):

$$\mathbf{i}_\mathbf{c}^\mathrm{R} = \kappa \left[ z_1 e^{j(\omega_c t + \phi_m)} + z_2 e^{j(-\omega_c t - \phi_m + 2\theta_r)} \right] \qquad \text{(4.23 revisited)}$$

For $R_s = 17.5\,\Omega, V_c = 20\,\mathrm{V}, f_c = 100\,\mathrm{Hz}$, we have:

$$\kappa|z_1| = 1.14\,\mathrm{A}, \quad \kappa|z_2| = 4.08\,\mathrm{mA}$$

For $R_s = 17.5\,\Omega, V_c = 20\,\mathrm{V}, f_c = 500\,\mathrm{Hz}$, we have:

$$\kappa|z_1| = 1.07\,\mathrm{A}, \quad \kappa|z_2| = 18.0\,\mathrm{mA}$$

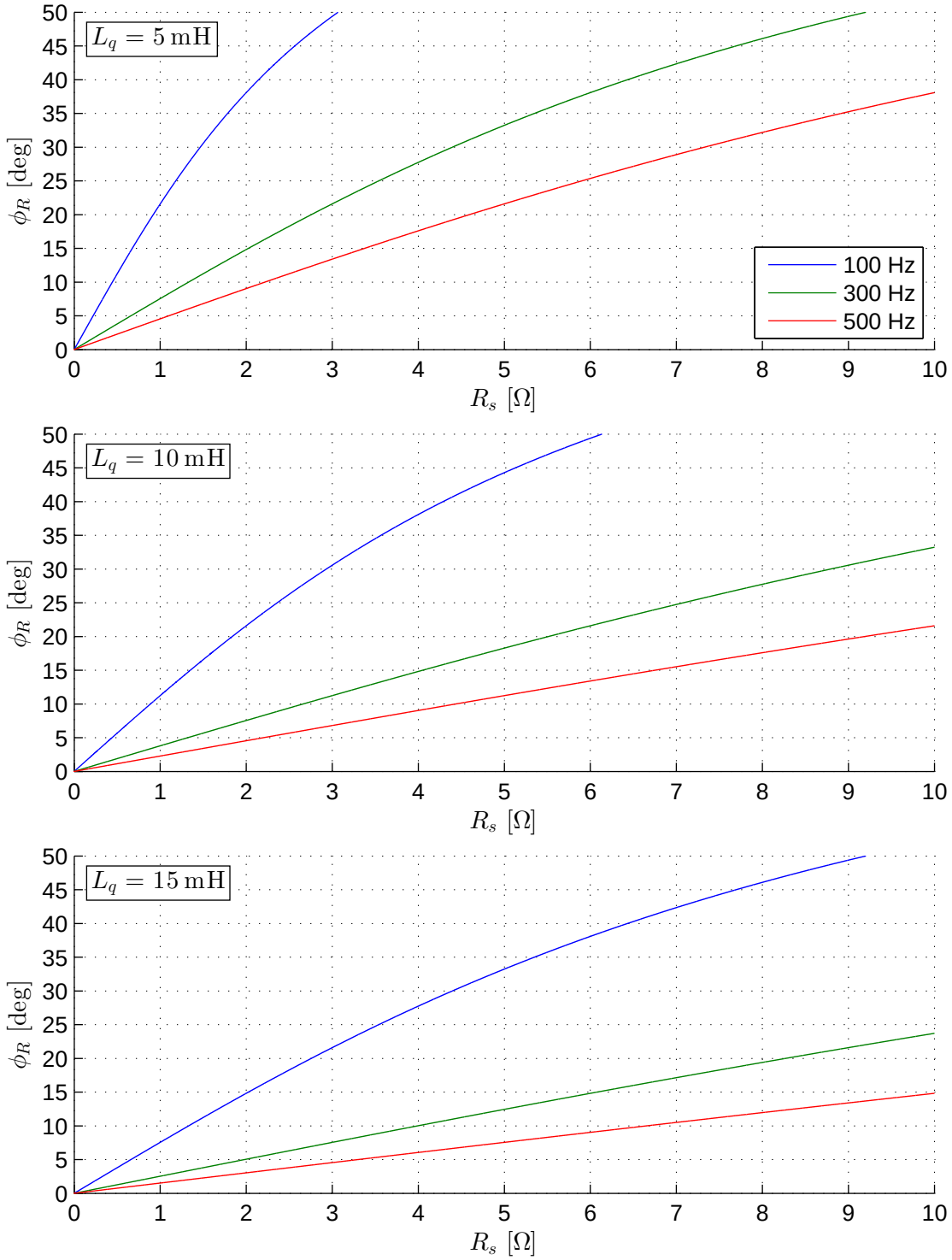


Figure 4.8.: Example plots of estimation error $\phi_R$ for a selection of injection frequencies $f_c = 2\pi\omega_c$ and machine inductances $L_d = \frac{2}{3}L_q$.

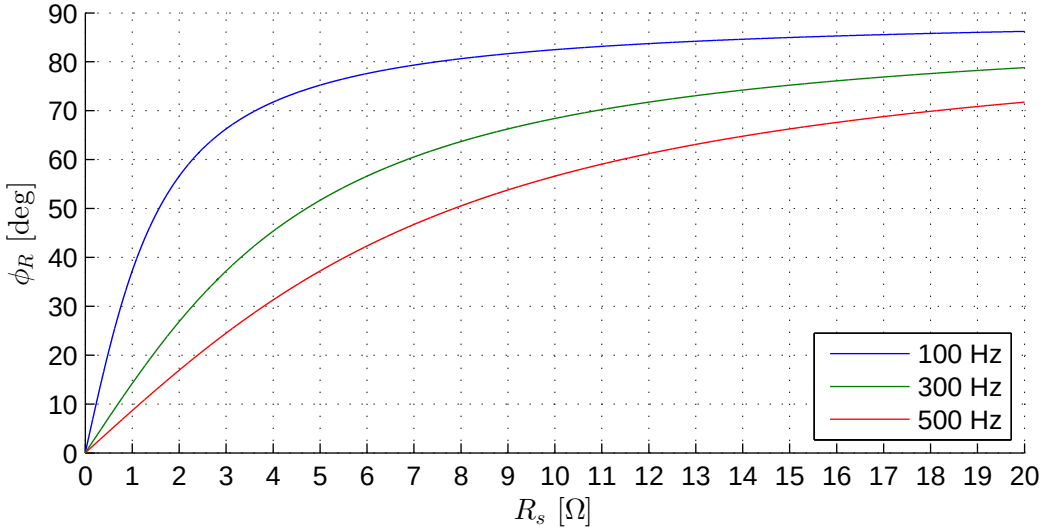


Figure 4.9.: Estimation error $\phi_R$ for the Siemens motor for a selection of injection frequencies $f_c = 2\pi\omega_c$.

Injecting $\mathbf{v_c} = 20e^{j(2\pi 500t)}\,\mathrm{V}$ thus narrowly keeps the inverter in its linear range while increasing the amplitude $\kappa|z_2|$ of the component required for estimation of $\theta_r$. Figure 4.10 shows a measurement of the three-phase current response and the DFT of its equivalent current space vector $\mathbf{i_c}$. Note that the currents are measured with a quantization step size of 488 µA/LSB. Measuring a component with an amplitude of 18.0 mA with a quantization step size of 15.8 mA/LSB would not be feasible due to the quantization noise it introduces.

As seen in Figure 4.10, the components at 500 Hz and −500 Hz have amplitudes of approximately 0 dBA = 1 A and −35 dBA = 17.8 mA, respectively.

Define the angular position estimation error as:

$$\tilde{\theta}_r \triangleq \theta_r - \hat{\theta}_r^{4q} \tag{4.32}$$

Processing the current $\mathbf{i_c}$ according to Figure 4.7 yields the estimate $\hat{\theta}_r^{4q}$ and estimation error $\tilde{\theta}_r$ shown in Figure 4.12. Angles are wrapped to the range $[-\pi;\pi]$ with:

$$\theta_{\text{wrap}} = \theta - 2\pi \left\lfloor \frac{\theta+\pi}{2\pi} \right\rfloor \tag{4.33}$$

For the low-pass filter, a fourth-order Chebyshev Type II filter was used with a stop-band frequency of 100 Hz and 40 dB attenuation[6]. Figure 4.11 shows the gain spectrum and impulse response of the LPF. As seen, any transient state of the filter will have decayed

[6]The digital IIR filter is implemented as a cascade configuration of biquadratic sections to minimize the effects of filter coefficient quantization.

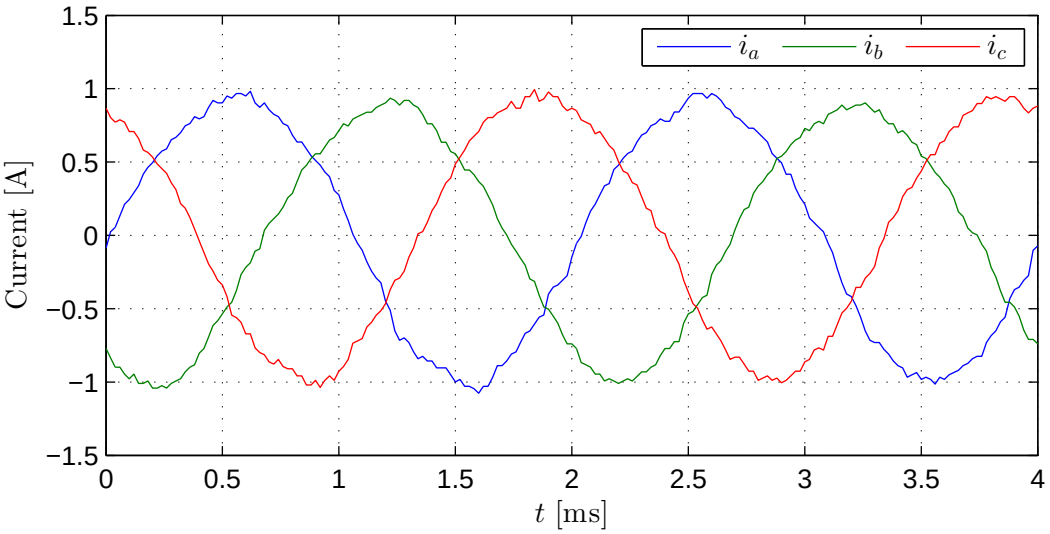


(a) Three-phase currents

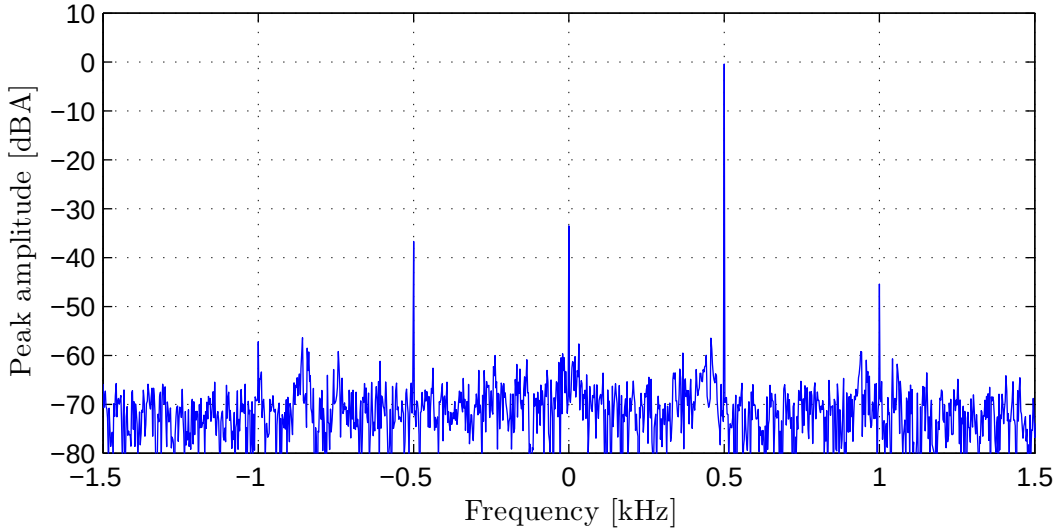


(b) DFT of current space vector $\mathbf{i_c}$, 2.5 Hz/bin

Figure 4.10.: Measured current response for $V_c = 20\,\mathrm{V}$, $f_c = 500\,\mathrm{Hz}$.

fully after approximately 60 ms, though, the bandwidth of the filter is generally not a critical design parameter. The output of the filter does continuously vary in phase as a function of the angular position of the rotor, which might make one consider how the transient performance of the filter affects the position estimate. For low-speed operation, though, the phase changes so slowly that the LPF is effectively always in steady state regardless of filter bandwidth.

Since the only objective of the LPF is to isolate the DC component, the choice of LPF type is also not critical. The Chebyshev Type II filter was only chosen here since its design method allows specifying the order, stop-band frequency and attenuation directly[7], which is useful for prototyping digital filters for a range of applications. An equivalent FIR design would be much more efficient if, for instance, the current is to be downsampled before filtering takes place.

As shown in Figure 4.12, the estimation error is approximately in the range $[-12°; 12°]$ around a mean of $72°$, as predicted by Figure 4.9. Although this result is of little practical use, due to the large estimation bias and restriction on inverter current range, it does verify the derivation that lead to its prediction.

### 4.5.2. Nonlinear Inverter Range

For $R_s = 0.18\,\Omega, V_c = 30\,\mathrm{V}, f_c = 500\,\mathrm{Hz}$, we have:

$$\kappa|z_1| = 4.56\,\mathrm{A}, \quad \kappa|z_2| = 217\,\mathrm{mA} \tag{4.34}$$

Figure 4.13 and Figure 4.14 shows the three-phase current response and DFT of the equivalent current space vector without and with compensation enabled for the inverter voltage error, respectively. As seen, for both cases, the nonlinearity of the inverter adds significant distortion in the 100 Hz filter bandwidth of the component at $-500\,\mathrm{Hz}$.

Figure 4.15 shows the tracking performance for both cases, and, as shown, there is little to no correlation between the measured angular position of the rotor $\theta_r$ and the estimate $\hat{\theta}_r^{4q}$. Decreasing the bandwidth of the LPF gives similar results, which means the inverter voltage error must, for both cases, contain a component at $-500\,\mathrm{Hz}$ that is significant enough in magnitude to completely distort the phase of the component present in Figure 4.10b.

### 4.5.3. Spectrum of Current Response to Inverter Voltage Error

If we decompose the output voltage of the inverter $\mathbf{v_s}$ into a command, or reference, voltage $\mathbf{v_s^*}$ and an error component $\tilde{\mathbf{v}}_\mathbf{s}$, we have:

$$\mathbf{v_s} = \mathbf{v_s^*} + \tilde{\mathbf{v}}_\mathbf{s} \tag{4.35}$$

[7] MATLAB v8.1 with the DSP System Toolbox v8.4 was utilized for digital filter design.

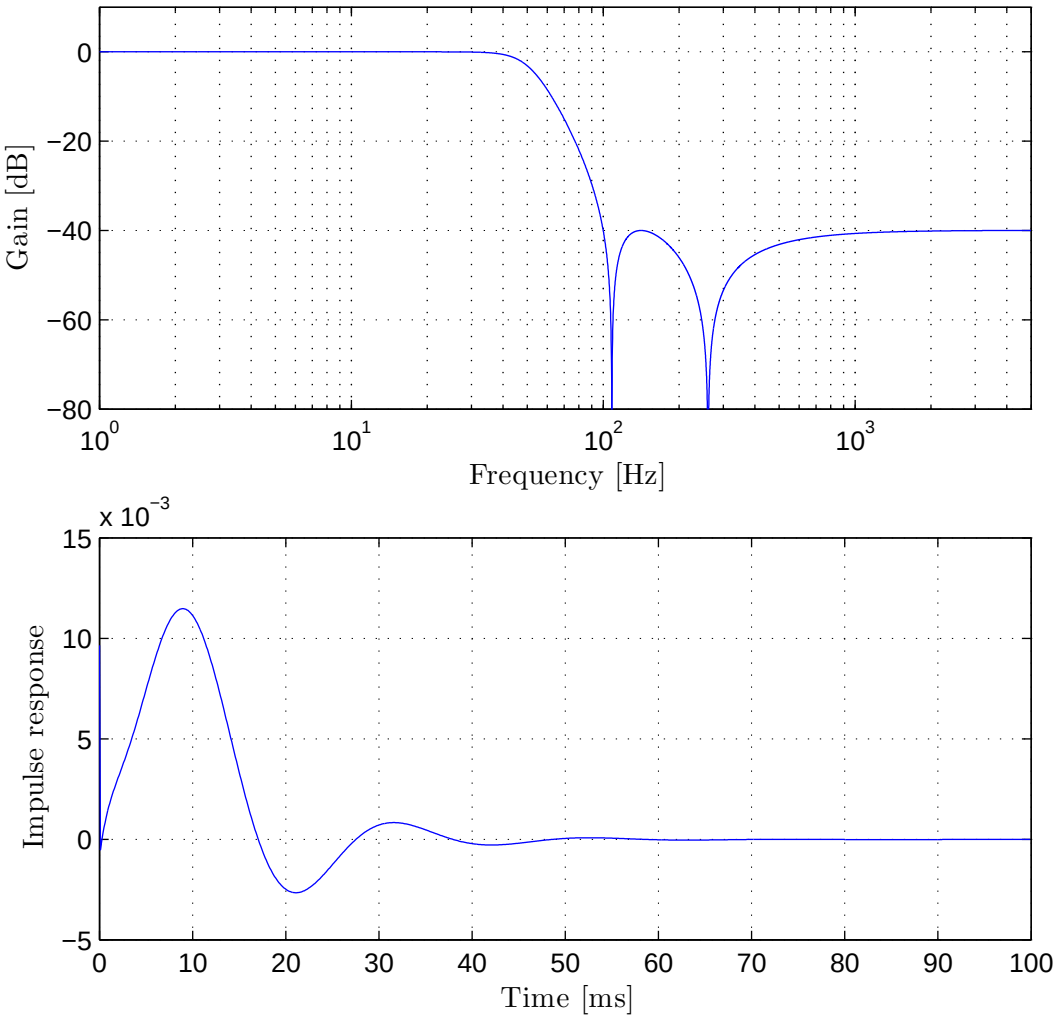


Figure 4.11.: Gain spectrum and impulse response of fourth-order Chebyshev Type II filter with a stop-band frequency of 100 Hz and 40 dB attenuation.

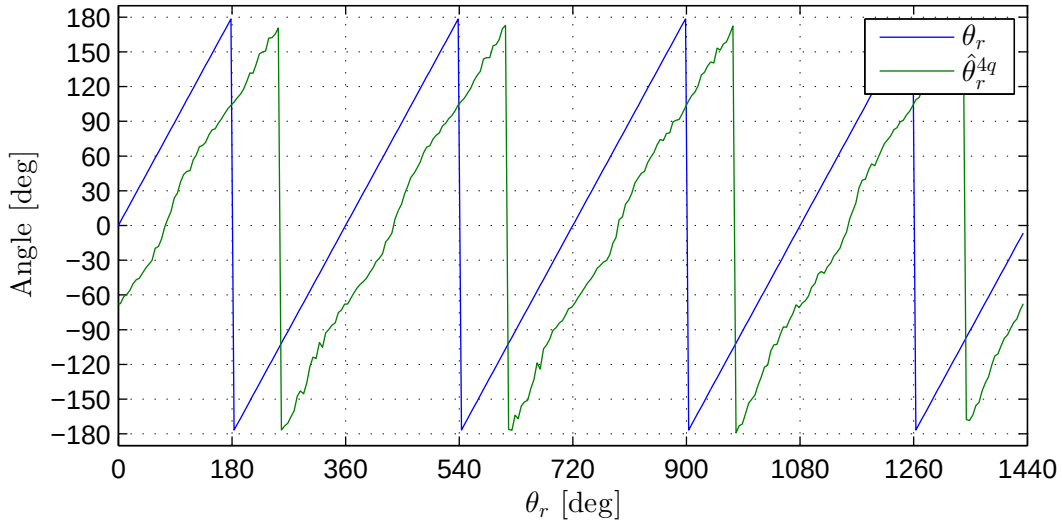


(a) Angular position $\theta_r$ and estimate $\hat{\theta}_r^{4q}$

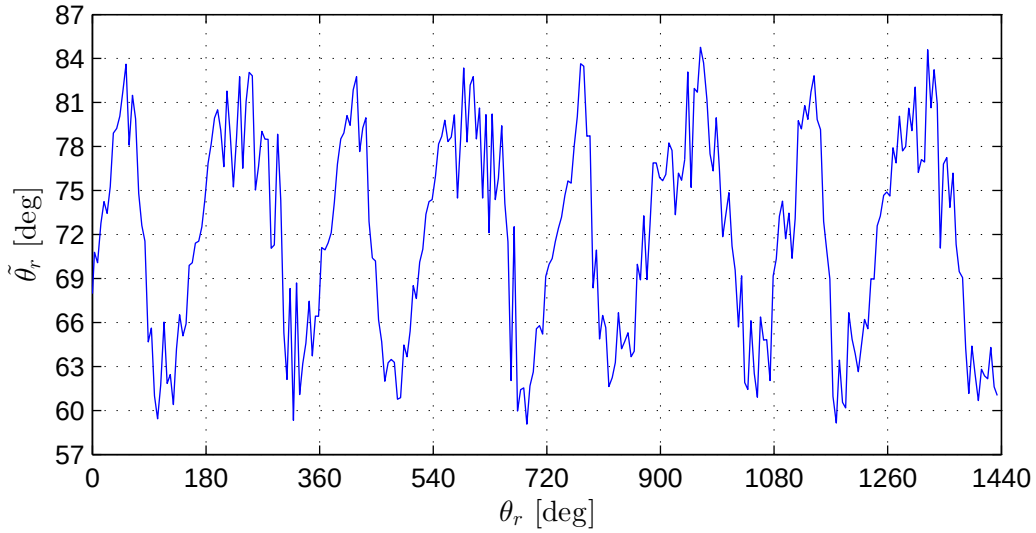


(b) Angular position error $\tilde{\theta}_r$

Figure 4.12.: Measured tracking performance for $V_c = 20\,\mathrm{V}$, $f_c = 500\,\mathrm{Hz}$. Inverter in its linear range.

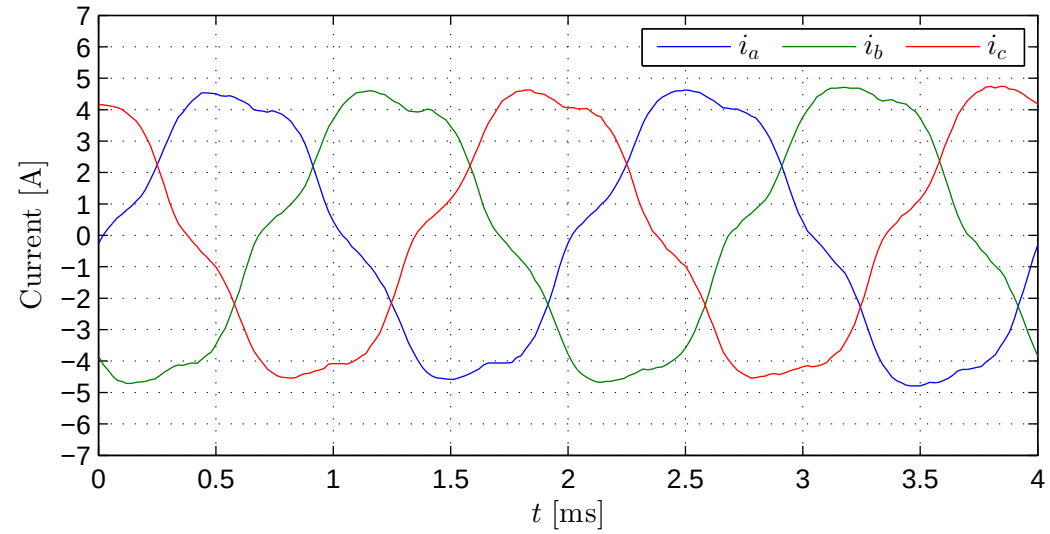


(a) Three-phase currents

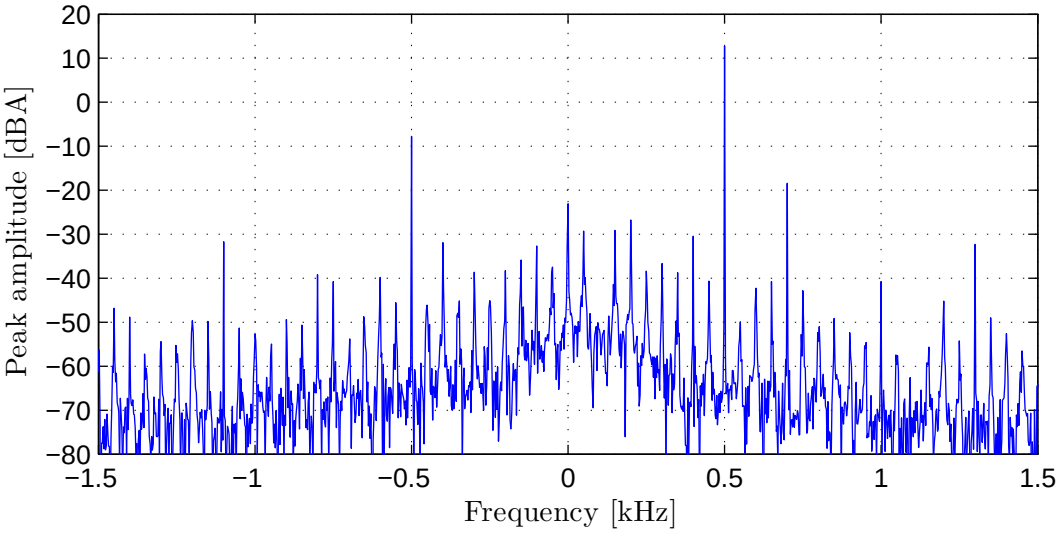


(b) DFT of current space vector $\mathbf{i_c}$, 2.5 Hz/bin

Figure 4.13.: Measured current response for $V_c = 30\,\mathrm{V}$, $f_c = 500\,\mathrm{Hz}$.

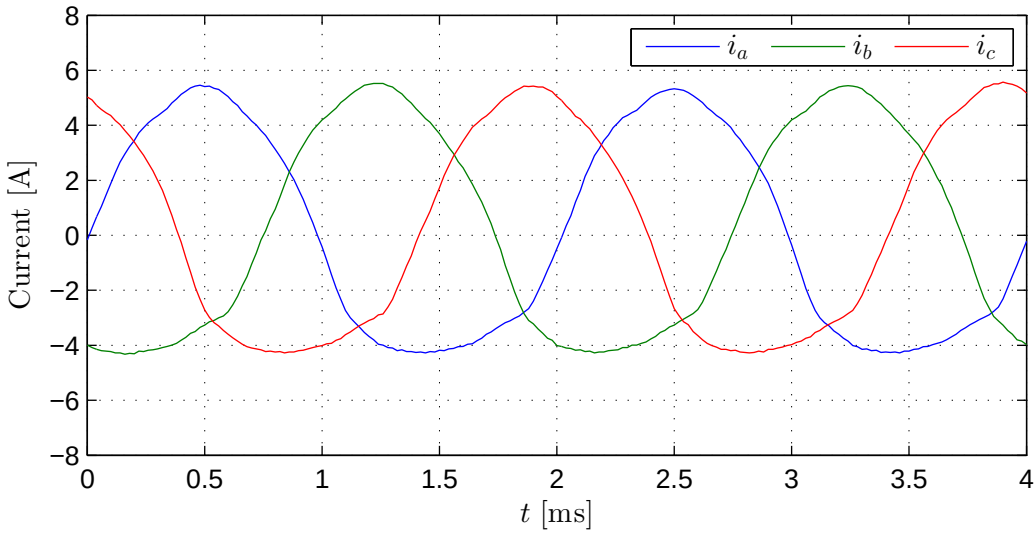


(a) Three-phase currents

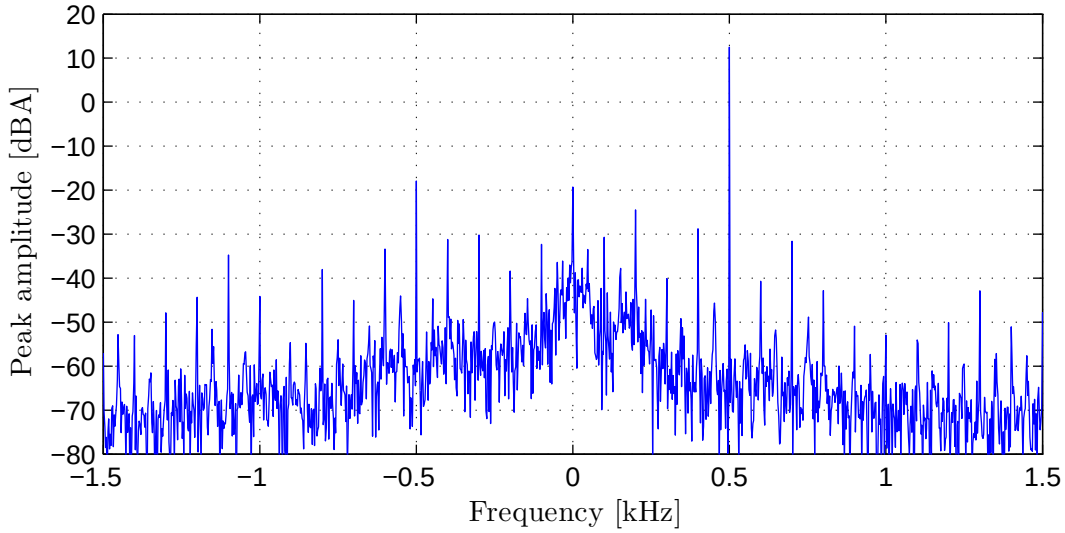


(b) DFT of current space vector $\mathbf{i_c}$, 2.5 Hz/bin

Figure 4.14.: Measured current response for $V_c = 5\,\mathrm{V}$, $f_c = 500\,\mathrm{Hz}$ with compensation for the inverter voltage error enabled.

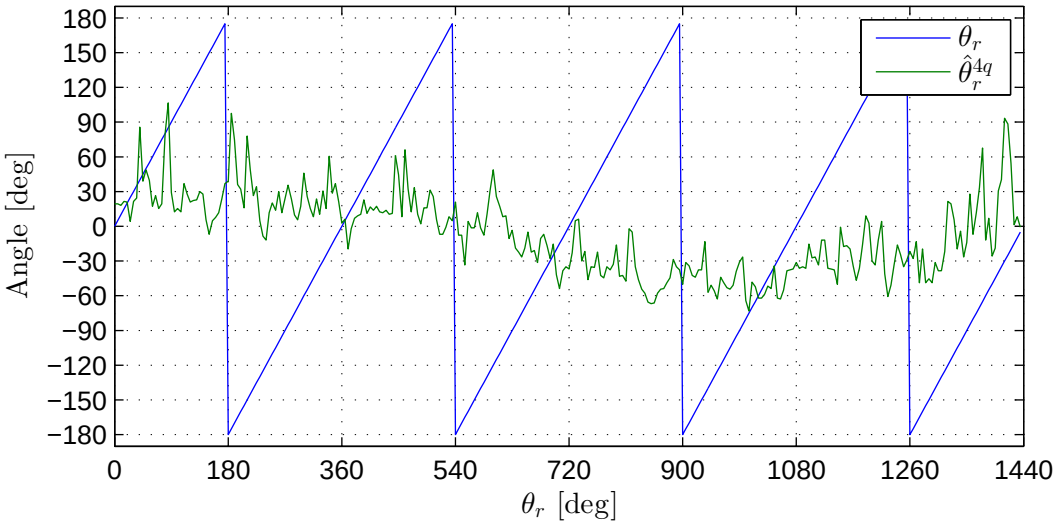


(a) $V_c = 30\,\mathrm{V}$, $f_c = 500\,\mathrm{Hz}$

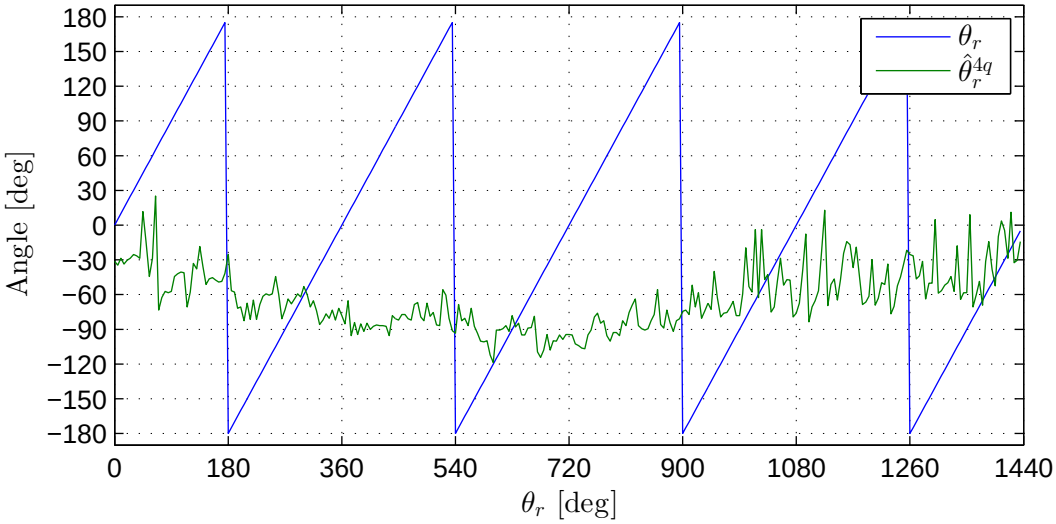


(b) $V_c = 5\,\mathrm{V}$, $f_c = 500\,\mathrm{Hz}$, compensation enabled

Figure 4.15.: Measured tracking performance without and with compensation enabled for the inverter voltage error. Inverter in its nonlinear range.

Assuming a linear system, the machine will respond with a current:

$$\mathbf{i_s} = \mathbf{i_s^*} + \tilde{\mathbf{i}}_\mathbf{s} \tag{4.36}$$

where $\mathbf{i_s^*}$ and $\tilde{\mathbf{i}}_\mathbf{s}$ are the individual current responses to $\mathbf{v_s^*}$ and $\tilde{\mathbf{v}}_\mathbf{s}$, respectively.

If we let $\mathbf{v_s^*} = V_c e^{j\omega_c t}$, where $\omega_c$ is high enough in value for the high-frequency model (4.5) to be a valid approximation, we have:

$$\mathbf{i_s^*} = \frac{V_c}{j\omega_c(L_1^2 - L_2^2)} \left[ L_1 e^{j(\omega_c t + \phi_m)} - L_2 e^{j(-\omega_c t - \phi_m + 2\theta_r)} \right] \tag{4.37}$$

The amplitude of the component of $\mathbf{i_s^*}$ at $-\omega_c$ can be increased by increasing either $V_c$ or $L_2$. For the example in Section 4.5.2, $V_c$ is already large enough in magnitude to yield a significant torque-producing current, and $L_2$, a measure of the effective saliency of the machine, is determined solely by the configuration of the machine itself. The limits, it would seem, have, for the Siemens motor, been reached in an effort to make the estimation of $\theta_r$ function outside the linear range of the inverter.

It would be interesting to be able to answer the question of what, exactly, determines the frequency component of $\tilde{\mathbf{i}}_\mathbf{s}$ at $-\omega_c$? With that knowledge, the circumstances that would allow the estimation of $\theta_r$ to function outside the linear range of the inverter, could be found. This amounts to analytically determining the spectrum of $\tilde{\mathbf{i}}_\mathbf{s}$, which foremost requires an analytical expression for $\tilde{\mathbf{v}}_\mathbf{s}$. From Section 3.1.2 we know that such an expression would have to be a nonlinear function of both $\mathbf{v_s^*}$ and $\mathbf{i_s}$:

$$\tilde{\mathbf{v}}_\mathbf{s} = \tilde{\mathbf{v}}_\mathbf{s}(\mathbf{v_s^*}, \mathbf{i_s}) \tag{4.38}$$

Determining its current response $\tilde{\mathbf{i}}_\mathbf{s}$, a solution to (4.5), would be the next step. If it exists, its Fourier series would then analytically give its spectrum.

If possible, such an analysis would represent in and of itself a significant body of work. We will merely conclude here that the sensitivity of the method presented in this chapter to distortion from the inverter voltage error is something to be aware of, especially for machines with very low saliency ratios, as the Siemens motor tested here. It should be noted that the Siemens machine is built as a high-performance servo motor, and as such, its type of construction is not typically found among standard industrial AC motors. If the sole objective is to reduce the unit price of the motor, it will typically be built with less iron, which tends to enhance its anisotropic properties due to magnetic saturation. Kim and Sul (1994), Xiang and He (2007), and Jianmin and Jianwei (2011) present positive results for machines with higher saliency ratios and/or, presumably, more effective compensation of the inverter voltage error.

## 4.6. Summary

In this chapter, an algorithm to estimate the angular position of the rotor of a SMPMSM, based on its anisotropic magnetic properties, was developed in the framework of space-vectors.

By injecting a balanced set of high-frequency voltages into the machine, signal processing of its current response reveals information about the angular position of the magnetic axis of the PM field, and thereby the angular position of the rotor itself. Tracking the polarity of the PM field requires additional processing, for which a method was developed. Additionally, the effect of stator winding resistance was analytically determined and was found to result in an estimation error of the rotor position, which can be significant for low-inductance machines.

The estimation algorithm was tested on the Siemens servo motor with the specifications listed in Table 3.2. For a current range that keeps the inverter voltage error linear, the measurement results validated the estimation algorithm to within $\pm 10^\circ$. Driving the machine outside this current range, however, which can easily occur while loaded, would cause the algorithm to fail to track the rotor position. This can be seen as an effect of the very low saliency ratio of the Siemens motor and/or poor compensation of the inverter voltage error. The method has been verified in the referenced works to function accurately for machines with higher saliency ratios.

# 5. Voltage Pulse Injection

The measurement results of Chapter 4 showed an example of where very accurate compensation of the inverter voltage error was necessary. In general, the high-frequency injection methods, that estimate the angular position of the rotor by frequency-domain signal processing, require some form of compensation of the voltage error introduced by the inverter (Holtz 2008). This typically requires off-line characterization of the inverter in use, which ties the user of the estimation algorithm to a specific hardware platform and configuration. In an effort to remove this dependency, this chapter will present methods that specifically take into account the effects of the inverter voltage error. In contrast to the method introduced in Chapter 4 and its variants, the methods of this chapter are time-domain based.

## 5.1. Clamping the Voltage Injection Angle

As an example, assume that we want to inject a voltage $\mathbf{v_s}$ with $\arg(\mathbf{v_s}) = 0°$, which makes $\mathbf{v_s}$ purely real:

$$\mathbf{v_s} = v_\alpha + jv_\beta = v_\alpha, \quad v_\beta = 0 \tag{5.1}$$

The equations for SVM synthesis of $\mathbf{v_s}$ are given by:

$$d_a = \frac{1}{2} + \frac{3}{4}\frac{v_\alpha}{V_{\mathrm{DC}}} \tag{5.2a}$$

$$d_b = \frac{1}{2} - \frac{3}{4}\frac{v_\alpha}{V_{\mathrm{DC}}} \tag{5.2b}$$

$$d_c = \frac{1}{2} - \frac{3}{4}\frac{v_\alpha}{V_{\mathrm{DC}}} \tag{5.2c}$$

The duty cycle values (5.2) then ideally produce the reference voltages:

$$\langle v_{aN} \rangle = v_{aN}^* = d_a V_{\mathrm{DC}} = \frac{1}{2}V_{\mathrm{DC}} + \frac{3}{4}v_\alpha \tag{5.3a}$$

$$\langle v_{bN} \rangle = v_{bN}^* = d_b V_{\mathrm{DC}} = \frac{1}{2}V_{\mathrm{DC}} - \frac{3}{4}v_\alpha \tag{5.3b}$$

$$\langle v_{cN} \rangle = v_{cN}^* = d_c V_{\mathrm{DC}} = \frac{1}{2}V_{\mathrm{DC}} - \frac{3}{4}v_\alpha \tag{5.3c}$$

Applying the space-vector transformation:

$$\begin{aligned}
\mathbf{v_s} &= \frac{2}{3}\left[\langle v_{aN}\rangle + \mathbf{a}\langle v_{bN}\rangle + \mathbf{a^2}\langle v_{cN}\rangle\right] \\
&= \frac{2}{3}\left(v^*_{aN} + \mathbf{a}v^*_{bN} + \mathbf{a^2}v^*_{cN}\right) \\
&= \frac{2}{3}\left[\frac{1}{2}V_{\mathrm{DC}} + \frac{3}{4}v_\alpha + \mathbf{a}\left(\frac{1}{2}V_{\mathrm{DC}} - \frac{3}{4}v_\alpha\right) + \mathbf{a^2}\left(\frac{1}{2}V_{\mathrm{DC}} - \frac{3}{4}v_\alpha\right)\right] \\
&= \frac{1}{2}v_\alpha - \mathbf{a}\frac{1}{2}v_\alpha - \mathbf{a^2}\frac{1}{2}v_\alpha \\
&= v_\alpha
\end{aligned} \tag{5.4}$$

Due to the nonideal characteristics of the inverter, the output voltage of each leg will include an error component $\tilde{v}_{pN}$ that is a function of its duty cycle and current:

$$\langle v_{aN}\rangle = v^*_{aN} + \tilde{v}_{aN}(d_a, i_a) \tag{5.5a}$$
$$\langle v_{bN}\rangle = v^*_{bN} + \tilde{v}_{bN}(d_b, i_b) \tag{5.5b}$$
$$\langle v_{cN}\rangle = v^*_{cN} + \tilde{v}_{cN}(d_c, i_c) \tag{5.5c}$$

where:

$$|\tilde{v}_{pN}| \lesssim \frac{T_{\mathrm{DT}}}{T_s}V_{\mathrm{DC}} \tag{5.6}$$

Applying the space-vector transformation again:

$$\begin{aligned}
\mathbf{v_s} &= \frac{2}{3}\left[\langle v_{aN}\rangle + \mathbf{a}\langle v_{bN}\rangle + \mathbf{a^2}\langle v_{cN}\rangle\right] \\
&= \frac{2}{3}\left[v^*_{aN} + \tilde{v}_{aN} + \mathbf{a}\left(v^*_{bN} + \tilde{v}_{bN}\right) + \mathbf{a^2}\left(v^*_{cN} + \tilde{v}_{cN}\right)\right] \\
&= \frac{2}{3}\left(v^*_{aN} + \mathbf{a}v^*_{bN} + \mathbf{a^2}v^*_{cN}\right) + \frac{2}{3}\left(\tilde{v}_{aN} + \mathbf{a}\tilde{v}_{bN} + \mathbf{a^2}\tilde{v}_{cN}\right) \\
&= v_\alpha + \tilde{\mathbf{v}}_\mathbf{s}
\end{aligned} \tag{5.7}$$

where:

$$\tilde{\mathbf{v}}_\mathbf{s} = \frac{2}{3}\left(\tilde{v}_{aN} + \mathbf{a}\tilde{v}_{bN} + \mathbf{a^2}\tilde{v}_{cN}\right) \tag{5.8}$$

For this example, the error component $\tilde{v}_{aN}$ affects only the magnitude of $\mathbf{v_s}$, but $\tilde{v}_{bN}$ and $\tilde{v}_{cN}$ affects its angle. Depending on the magnitude of $v_\alpha$, since $\frac{T_{\mathrm{DT}}}{T_s}V_{\mathrm{DC}}$ can be a significant fraction of $V_{\mathrm{DC}}$, $\tilde{\mathbf{v}}_\mathbf{s}$ can indeed greatly affect the angle of $\mathbf{v_s}$, especially for opposite polarities of $\tilde{v}_{bN}$ and $\tilde{v}_{cN}$.

Consider again synthesizing $\mathbf{v_s} = v_\alpha$, but instead of (5.2), we use the duty cycle values:

$$d_a = \frac{3}{2}\frac{v_\alpha}{V_{\mathrm{DC}}} \tag{5.9a}$$
$$d_b = 0 \tag{5.9b}$$
$$d_c = 0 \tag{5.9c}$$

The reference voltages are then:

$$v^*_{aN} = d_a V_{\mathrm{DC}} = \frac{3}{2} v_\alpha \tag{5.10a}$$
$$v^*_{bN} = d_b V_{\mathrm{DC}} = 0\,\mathrm{V} \tag{5.10b}$$
$$v^*_{cN} = d_c V_{\mathrm{DC}} = 0\,\mathrm{V} \tag{5.10c}$$

And again we have:

$$\begin{aligned}\mathbf{v_s} &= \frac{2}{3}\left[\langle v_{aN}\rangle + \mathbf{a}\langle v_{bN}\rangle + \mathbf{a^2}\langle v_{cN}\rangle\right] \\ &= \frac{2}{3}\left(v^*_{aN} + \mathbf{a}v^*_{bN} + \mathbf{a^2}v^*_{cN}\right) + \frac{2}{3}\left(\tilde{v}_{aN} + \mathbf{a}\tilde{v}_{bN} + \mathbf{a^2}\tilde{v}_{cN}\right) \\ &= v_\alpha + \tilde{\mathbf{v}}_\mathbf{s}\end{aligned} \tag{5.11}$$

For $i_a > 0, i_b > 0, i_c < 0$, Figure 5.1 shows the output voltages of the inverter for both cases (5.2) and (5.10). What is important to note is that, by not switching legs b and c, we are effectively clamping $\tilde{v}_{bN}$ and $\tilde{v}_{cN}$ to $-V_D$ and $V_T$, respectively. Since typically $V_D \ll V_{\mathrm{DC}}, V_T \ll V_{\mathrm{DC}}$, we can consider $\tilde{v}_{bN}$ and $\tilde{v}_{cN}$ to be negligible in magnitude, so we have:

$$\mathbf{v_s} = v_\alpha + \frac{2}{3}\tilde{v}_{aN} \tag{5.12}$$

Thus, by using (5.10) instead of (5.2), we are effectively clamping the voltage injection angle to the axis of phase a. Since we could just as well have constructed the example for phase b or c, we conclude that there are exactly three voltage vectors we can inject, aligned with the phase axes, where the injection angle is accurately controlled, despite the voltage error introduced by the inverter. This requires, however, that we use a switching pattern as shown in Figure 5.1b instead of the de facto standard symmetrical SVM shown in Figure 5.1a.

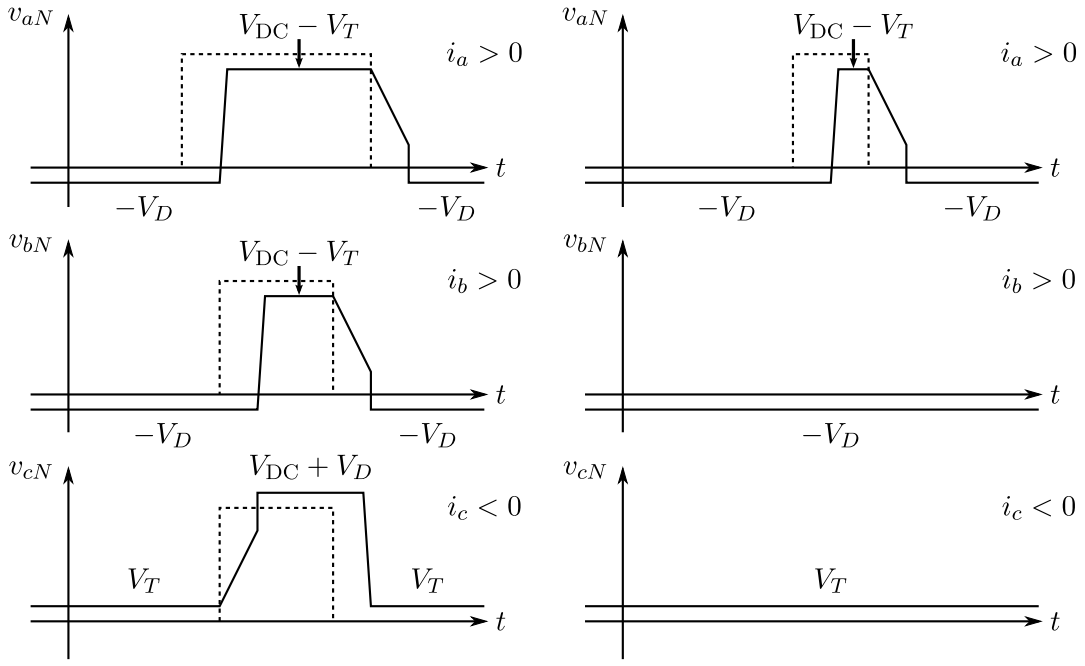


(a) Symmetrical SVM (b) Single-leg switching

Figure 5.1.: Schematic of inverter output voltages for the synthesis of $\mathbf{v_s} = v_\alpha$.

## 5.2. The INFORM Method

The estimation algorithm presented here is based on the 'INdirect Flux detection by On-line Reactance Measurement' method, first published by Schroedl (1992). The name stems from the framework within the method was originally developed, but here we will instead present it in the framework of space vectors and with an emphasis on controlling the influence of the inverter voltage error.

Recall the low-speed model:

$$\mathbf{v_s} = R_s \mathbf{i_s} + \frac{\mathrm{d}}{\mathrm{d}t}(L_1 \mathbf{i_s}) - \frac{\mathrm{d}}{\mathrm{d}t}\left(L_2 \overline{\mathbf{i_s}}\right) e^{j2\theta_r} \qquad \text{(4.2 revisited)}$$

Eq. (4.2) can be expressed as:

$$\mathbf{v_s} = \underbrace{R_s \mathbf{i_s}}_{(1)} + \underbrace{\frac{\mathrm{d}L_1}{\mathrm{d}t}\mathbf{i_s}}_{(2)} + \underbrace{L_1 \frac{\mathrm{d}\mathbf{i_s}}{\mathrm{d}t}}_{(3)} - \underbrace{\frac{\mathrm{d}L_2}{\mathrm{d}t}\overline{\mathbf{i_s}} e^{j2\theta_r}}_{(4)} - \underbrace{L_2 \frac{\mathrm{d}\overline{\mathbf{i_s}}}{\mathrm{d}t} e^{j2\theta_r}}_{(5)} \qquad (5.13)$$

A step change in applied voltage $\mathbf{v_s}$ must be balanced by terms (1)-(5) in (5.13). For $\mathbf{v_s} \gg \mathbf{i_s}$, terms (1), (2) and (4) are typically small in magnitude relative to terms (3) and (5). $R_s$ does not scale $\mathbf{i_s}$ significantly in term (1) and changes in $L_1$ and $L_2$ do not

typically occur abruptly in time unless the machine is being driven into deep saturation. We can then work with the simplified model:

$$\mathbf{v_s} = L_1 \frac{\mathrm{d}\mathbf{i_s}}{\mathrm{d}t} - L_2 \frac{\mathrm{d}\overline{\mathbf{i_s}}}{\mathrm{d}t} e^{j2\theta_r} \tag{5.14}$$

Solving (5.14) for $\frac{\mathrm{d}\mathbf{i_s}}{\mathrm{d}t}$ follows the same derivation as led to (4.13). We have then:

$$\frac{\mathrm{d}\mathbf{i_s}}{\mathrm{d}t} = \frac{1}{L_1^2 - L_2^2} \left( L_1 \mathbf{v_s} + L_2 \overline{\mathbf{v_s}} e^{j2\theta_r} \right) \tag{5.15}$$

Approximating (5.15) with a finite difference, we have:

$$\frac{\Delta\mathbf{i_s}}{\Delta t} = \frac{1}{L_1^2 - L_2^2} \left( L_1 \mathbf{v_s} + L_2 \overline{\mathbf{v_s}} e^{j2\theta_r} \right) \Leftrightarrow \tag{5.16}$$

$$\begin{aligned} \Delta\mathbf{i_s} &= \frac{1}{L_1^2 - L_2^2} \left( L_1 \mathbf{v_s} + L_2 \overline{\mathbf{v_s}} e^{j2\theta_r} \right) \Delta t \\ &= \left( c_1 \mathbf{v_s} + c_2 \overline{\mathbf{v_s}} e^{j2\theta_r} \right) \Delta t \end{aligned} \tag{5.17}$$

where:

$$c_1 = \frac{L_1}{L_1^2 - L_2^2} \tag{5.18}$$

$$c_2 = \frac{L_2}{L_1^2 - L_2^2} \tag{5.19}$$

Section 5.1 showed that we can accurately control the injection angle, if not magnitude, of $\mathbf{v_s}$ as an average over a switching period:

$$\mathbf{v_s} = \frac{2}{3} \left[ \langle v_{aN} \rangle + \mathbf{a} \langle v_{bN} \rangle + \mathbf{a^2} \langle v_{cN} \rangle \right] \tag{5.20}$$

Consider now instead the instantaneous voltage:

$$\mathbf{v_s}(t) = \frac{2}{3} \left[ v_{aN}(t) + \mathbf{a} v_{bN}(t) + \mathbf{a^2} v_{cN}(t) \right] \tag{5.21}$$

For the example shown in Figure 5.2, for $t \in [t_1; t_2]$, we have:

$$\begin{aligned} \mathbf{v_s}(t) &\approx \frac{2}{3} \left[ V_{\mathrm{DC}} + \mathbf{a} \left( 0\,\mathrm{V} \right) + \mathbf{a^2} \left( 0\,\mathrm{V} \right) \right] \\ &= \frac{2}{3} V_{\mathrm{DC}} \end{aligned} \tag{5.22}$$

Thus, for the three, phase-aligned voltage vectors, if we are able to do interperiod sampling, we can accurately control not only the angle, but also the magnitude of the injected voltage.

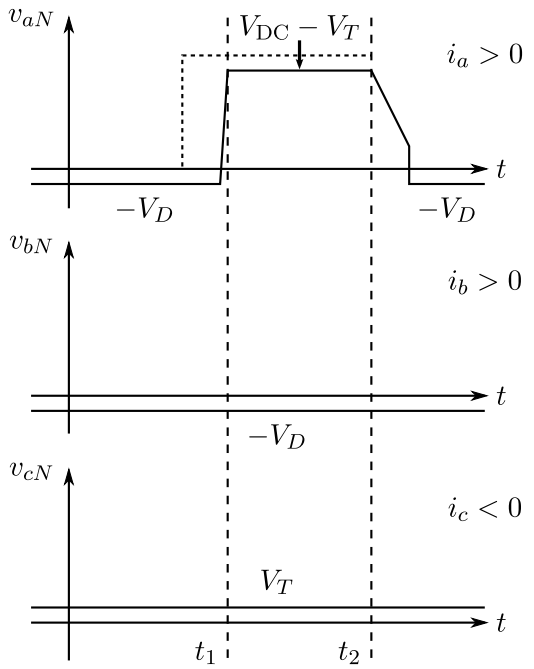


Figure 5.2.: Single-leg switching with $\mathbf{v_s}(t) \approx V_{\mathrm{DC}}$, $t_1 \leq t \leq t_2$.

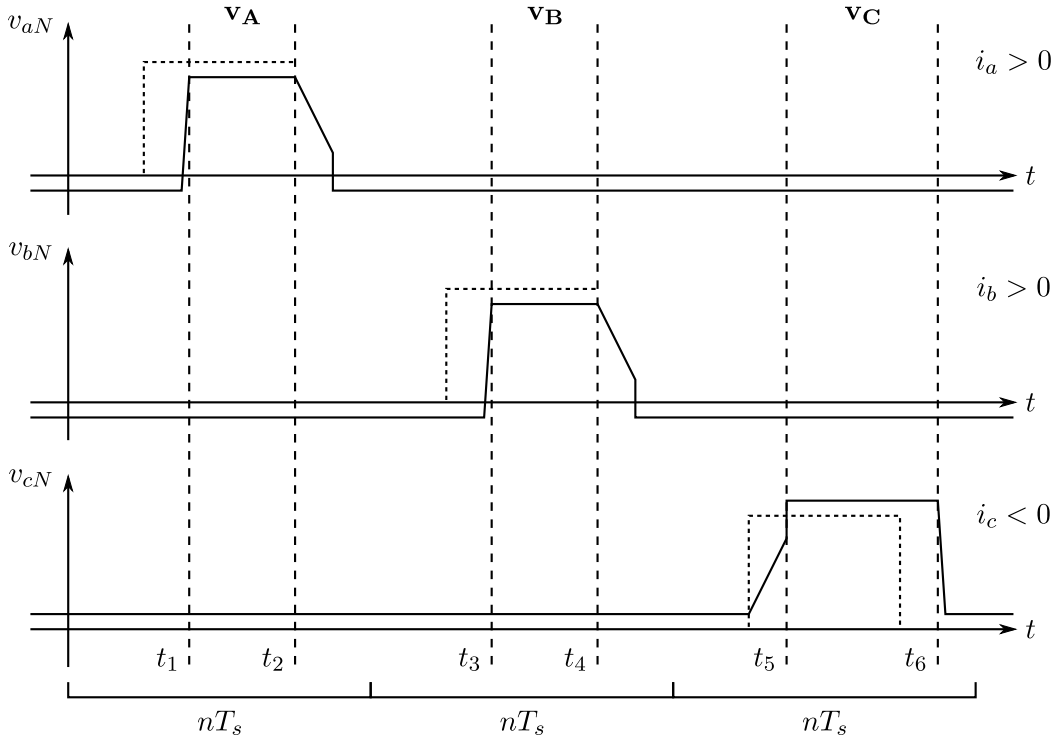


Figure 5.3.: Sequential injection of the three, phase-aligned voltage vectors with inter-period sampling.

If we sequentially inject the three, phase-aligned voltage vectors, as shown in Figure 5.3 with $n \in \mathbb{N}^+$, we have:

$$\mathbf{v_s}(t) = \mathbf{v_A} = \frac{2}{3}V_{\mathrm{DC}}, \qquad t_1 \le t \le t_2 \tag{5.23a}$$

$$\mathbf{v_s}(t) = \mathbf{v_B} = \frac{2}{3}V_{\mathrm{DC}}\mathbf{a}, \qquad t_3 \le t \le t_4 \tag{5.23b}$$

$$\mathbf{v_s}(t) = \mathbf{v_C} = \frac{2}{3}V_{\mathrm{DC}}\mathbf{a^2}, \quad t_5 \le t \le t_6 \tag{5.23c}$$

The current response to (5.23) is then given by:

$$\begin{aligned}\Delta\mathbf{i_A} &= \left(c_1\mathbf{v_A} + c_2\overline{\mathbf{v_A}}e^{j2\theta_r}\right)\Delta t \\ &= \frac{2}{3}V_{\mathrm{DC}}\left(c_1 + c_2e^{j2\theta_r}\right)\Delta t\end{aligned} \tag{5.24a}$$

$$\begin{aligned}\Delta\mathbf{i_B} &= \left(c_1\mathbf{v_B} + c_2\overline{\mathbf{v_B}}e^{j2\theta_r}\right)\Delta t \\ &= \frac{2}{3}V_{\mathrm{DC}}\left(c_1\mathbf{a} + c_2\mathbf{a^2}e^{j2\theta_r}\right)\Delta t\end{aligned} \tag{5.24b}$$

$$\begin{aligned}\Delta\mathbf{i_C} &= \left(c_1\mathbf{v_C} + c_2\overline{\mathbf{v_C}}e^{j2\theta_r}\right)\Delta t \\ &= \frac{2}{3}V_{\mathrm{DC}}\left(c_1\mathbf{a^2} + c_2\mathbf{a}e^{j2\theta_r}\right)\Delta t\end{aligned} \tag{5.24c}$$

Now define:

$$\mathbf{\Gamma} \triangleq \Delta\mathbf{i_A} + \mathbf{a}\Delta\mathbf{i_B} + \mathbf{a^2}\Delta\mathbf{i_C} \tag{5.25}$$

Substituting (5.24) in (5.25), we have:

$$\begin{aligned}\mathbf{\Gamma} &= \Delta\mathbf{i_A} + \mathbf{a}\Delta\mathbf{i_B} + \mathbf{a^2}\Delta\mathbf{i_C} \\ &= \frac{2}{3}V_{\mathrm{DC}}\left(c_1 + c_2e^{j2\theta_r}\right)\Delta t \\ &\quad + \mathbf{a}\frac{2}{3}V_{\mathrm{DC}}\left(c_1\mathbf{a} + c_2\mathbf{a^2}e^{j2\theta_r}\right)\Delta t \\ &\quad + \mathbf{a^2}\frac{2}{3}V_{\mathrm{DC}}\left(c_1\mathbf{a^2} + c_2\mathbf{a}e^{j2\theta_r}\right)\Delta t \\ &= \frac{2}{3}V_{\mathrm{DC}}\left(c_1 + c_1\mathbf{a} + c_1\mathbf{a^2} + 3c_2e^{j2\theta_r}\right)\Delta t \\ &= 2V_{\mathrm{DC}}c_2\Delta te^{j2\theta_r}\end{aligned} \tag{5.26}$$

Finally, we can thus estimate $\theta_r$ with:

$$\theta_r = \frac{1}{2}\arg\mathbf{\Gamma} \tag{5.27}$$

As in Section 4.2, Algorithm 1 extends the tracking range of (5.27) to four quadrants.

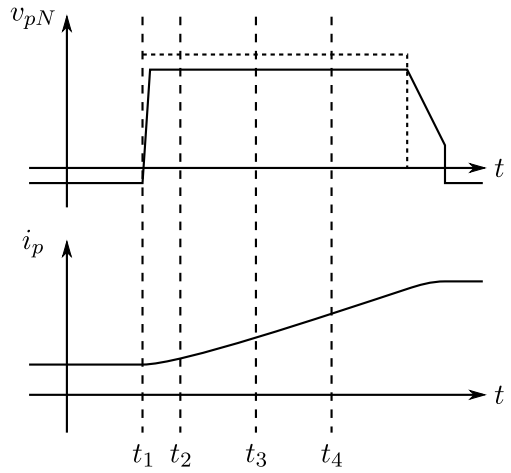


Figure 5.4.: Time division of voltage pulse.

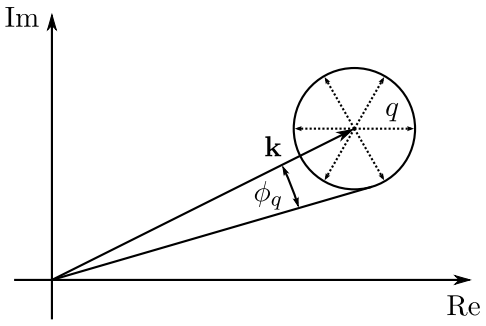


Figure 5.5.: Quantization angle.

### 5.2.1. Interperiod Sampling

Figure 5.4 shows an example of the output voltage and current of a single inverter leg divided into time slices. For:

$t_1 \leq t < t_2$: The inverter is in dead time with its output voltage determined by the load current.

$t_2 \leq t < t_3$: The inverter is in a well-defined state with $v_{pN} \approx V_{\mathrm{DC}}$ and constant current slope. $t_3$ marks the end of the transient response of any prefilter, if present.

$t_3 \leq t < t_4$: The current increment vectors $\Delta\mathbf{i_A}$, $\Delta\mathbf{i_B}$ and $\Delta\mathbf{i_C}$ can be accurately sampled.

We have:

$$T_{\mathrm{DT}} = t_2 - t_1 \tag{5.28}$$

Define also:

$$T_f \triangleq t_3 - t_2 \tag{5.29}$$

$$T_{\mathrm{aq}} \triangleq t_4 - t_3 \tag{5.30}$$

For the prefilter, it is important that it, while in steady state, does not alter the current slope. The steady-state error of the ramp response of, for instance, a single-pole, resistor-capacitor filter, with resistance $R$ and capacitance $C$, is constant in time. After a period of two time constants $\tau_{\mathrm{RC}} = RC$, the transient response of a RC-filter has decayed to approximately 13.5 %. Using this as a criteria to fix $t_3$ in time, we have, for a RC-filter:

$$T_f = 2\tau_{\mathrm{RC}} \tag{5.31}$$

We can determine $T_{\text{aq}}$ by considering the magnitude of $\mathbf{\Gamma}$:

$$|\mathbf{\Gamma}| = 2V_{\text{DC}}c_2\Delta t = 2V_{\text{DC}}c_2T_{\text{aq}} \tag{5.32}$$

Let $Q$ be the quantization step size of the sampling system. Define then:

$$q \triangleq \frac{2}{3}Q \tag{5.33}$$

Consider now the space vector $\mathbf{k}$ shown in Figure 5.5, which we will regard as quantized. Due to quantization, any sampled space vector can exist only at discrete points in the complex plane. For $\mathbf{k}$ in Figure 5.5, its neighbouring quantization points are also shown. Connecting these with a circle with radius $q$, we can, for the *quantization angle*, determine its upper bound $\phi_q$:

$$\tan\phi_q = \frac{q}{|\mathbf{k}|} \tag{5.34}$$

If we assume quantization to be the dominant source of measurement error, we have then:

$$\tan\phi_q = \frac{q}{|\Gamma|} = \frac{q}{2V_{\text{DC}}c_2T_{\text{aq}}} \Leftrightarrow \tag{5.35}$$

$$T_{\text{aq}} = \frac{q}{2V_{\text{DC}}c_2\tan\phi_q} = \frac{Q}{3V_{\text{DC}}c_2\tan\phi_q} \tag{5.36}$$

A lower bound on the required duty cycle $d_p$ for interperiod sampling is then given by:

$$d_p = \frac{T_{\text{DT}} + T_f + T_{\text{aq}}}{nT_s} \tag{5.37}$$

### 5.2.2. Estimation Rate

As shown in Figure 5.6, the INFORM method produces an estimate $\hat{\theta}_r$ by periodically assuming control of the machine and sequencing the three, phase-aligned voltage vectors in order to determine the current increments $\Delta\mathbf{i_A}$, $\Delta\mathbf{i_B}$ and $\Delta\mathbf{i_C}$. Since the average voltage over an INFORM period is approximately zero, the method presents little disturbance to the current loop of, for instance, field-oriented control.

Updates of $\hat{\theta}_r$ arrive then with a period $T_u$. If we require that:

$$|\theta_r(t) - \theta_r(t - T_u)| < \theta_u, \quad \theta_u > 0 \tag{5.38}$$

We must then have:

$$T_u < \frac{\theta_u}{\max|\omega_r|} \tag{5.39}$$

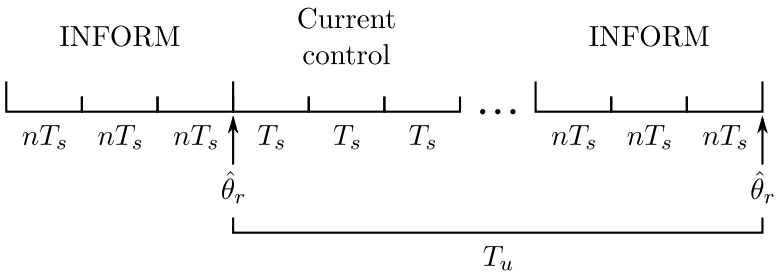


Figure 5.6.: Timing pattern of INFORM periods.

The estimation rate $f_u$ is thus constrained by:

$$f_u > \frac{\max|\omega_r|}{\theta_u} \tag{5.40}$$

Combining again the estimate $\hat{\theta}_r$, the state machine to determine $\hat{\theta}_r^{4q}$, polarity detection and a FOC topology yields the algorithm shown in Figure 5.7. $\hat{\theta}_r^{4q}$ is determined in order of:

1. Calculate an estimate $\hat{\theta}_r$ from (5.27).
2. If uninitialized, detect field polarity by voltage pulse injection as shown in Section 4.3. Skip otherwise.
3. Process Algorithm 1 to determine $\hat{\theta}_r^{4q}$.

Note that the INFORM method requires no filters and therefore introduces no phase lag into the FOC loop.

### 5.2.3. Effect of Magnetic Saturation

In (5.24) we assumed that $c_1$ and $c_2$ did not vary between sampling of $\Delta\mathbf{i_A}$, $\Delta\mathbf{i_B}$ and $\Delta\mathbf{i_C}$. In practice, however, we must allow for the possibility that $c_1$ and $c_2$ vary as a function of the current path followed when sequencing $\mathbf{v_A}$, $\mathbf{v_B}$ and $\mathbf{v_C}$, as shown in Figure 5.8. We could thus have slightly different values for $c_1$ and $c_2$ between sampling of current increments:

$$\Delta\mathbf{i_A} = \left(c_{1A}\mathbf{v_A} + c_{2A}\overline{\mathbf{v_A}}e^{j2\theta_r}\right)\Delta t \tag{5.41a}$$

$$\Delta\mathbf{i_B} = \left(c_{1B}\mathbf{v_B} + c_{2B}\overline{\mathbf{v_B}}e^{j2\theta_r}\right)\Delta t \tag{5.41b}$$

$$\Delta\mathbf{i_C} = \left(c_{1C}\mathbf{v_C} + c_{2C}\overline{\mathbf{v_C}}e^{j2\theta_r}\right)\Delta t \tag{5.41c}$$

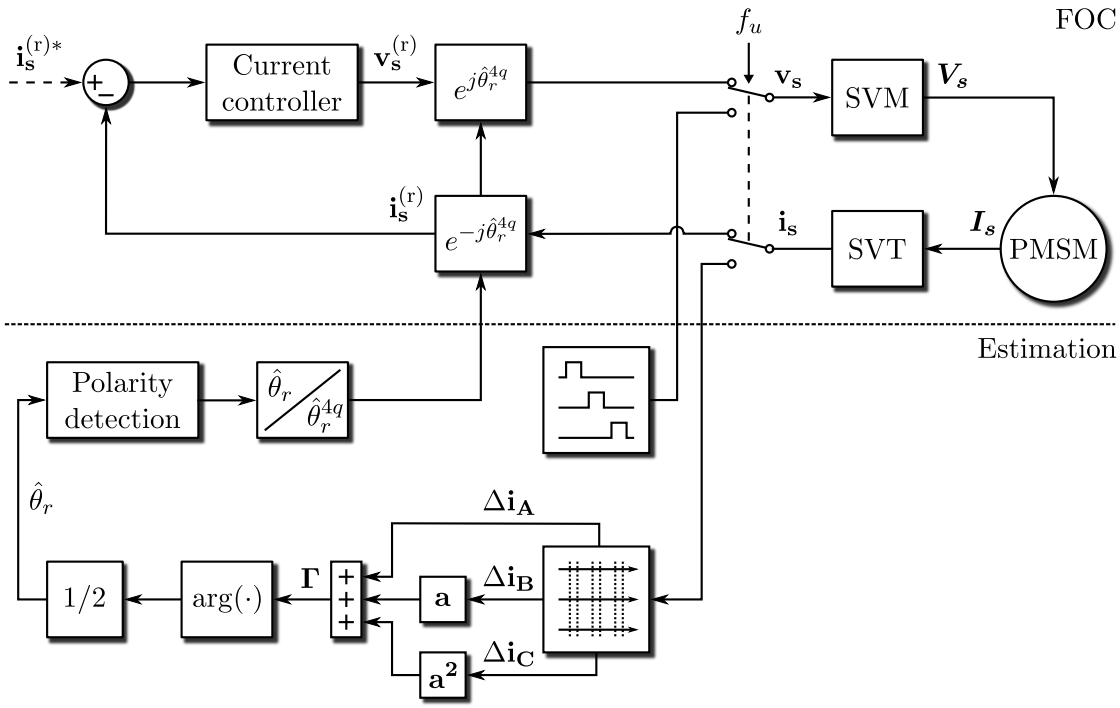


Figure 5.7.: Complete topology of the INFORM algorithm.

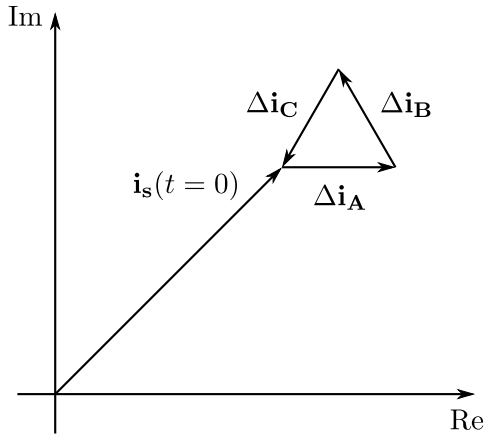


Figure 5.8.: Current path for sequencing $\mathbf{v_A}$, $\mathbf{v_B}$ and $\mathbf{v_C}$.

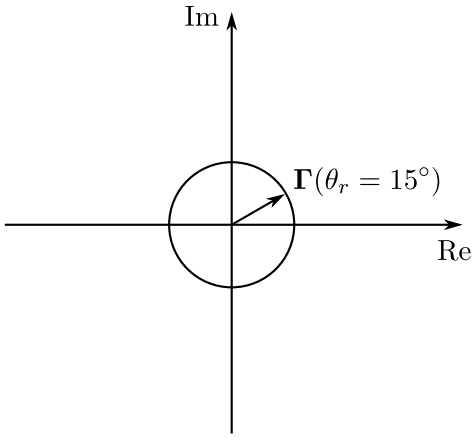


Figure 5.9.: Locus of $\boldsymbol{\Gamma}$ for a linear magnetic system.

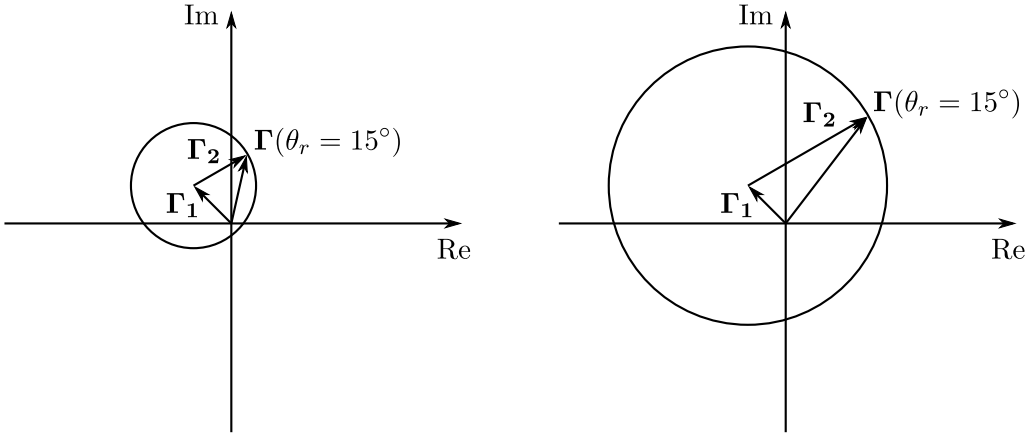


Figure 5.10.: The effect of magnetic saturation on the locus of $\mathbf{\Gamma}$.

We have then instead:

$$\begin{aligned}\mathbf{\Gamma} &= \frac{2}{3}V_{\mathrm{DC}}\Delta t\left(c_{1A} + c_{1B}\mathbf{a} + c_{1C}\mathbf{a^2}\right) \\ &\quad + 2V_{\mathrm{DC}}\Delta t\left(c_{2A} + c_{2B} + c_{2C}\right)e^{j2\theta_r} \\ &= \mathbf{\Gamma_1} + \mathbf{\Gamma_2}\end{aligned} \tag{5.42}$$

where:

$$\mathbf{\Gamma_1} = \frac{2}{3}V_{\mathrm{DC}}\Delta t\left(c_{1A} + c_{1B}\mathbf{a} + c_{1C}\mathbf{a^2}\right) \tag{5.43}$$

$$\mathbf{\Gamma_2} = 2V_{\mathrm{DC}}\Delta t\left(c_{2A} + c_{2B} + c_{2C}\right)e^{j2\theta_r} \tag{5.44}$$

For a linear magnetic system, we have $\mathbf{\Gamma_1} = 0$, but in practice, the components of $\mathbf{\Gamma_1}$ may not exactly sum to zero.

Figure 5.9 shows the locus of $\mathbf{\Gamma}$ for a linear magnetic system as $\theta_r$ traverses 180°. In Figure 5.10, we again show the locus of $\mathbf{\Gamma}$, but for the case where it is offset by $\mathbf{\Gamma_1}$ and scaled by different magnitudes of $\mathbf{\Gamma_2}$. In practice, $|\mathbf{\Gamma_1}|$ and $|\mathbf{\Gamma_2}|$ would vary with $\theta_r$, so the locus of $\mathbf{\Gamma}$ would not be perfectly circular, as depicted. Consider instead Figure 5.10 to be a simple schematic meant to show how the saliency ratio of the machine can mitigate the effect of magnetic saturation. As seen, since $\mathbf{\Gamma_2}$ is scaled by $L_2$, a higher saliency ratio can lessen the impact $\mathbf{\Gamma_1}$ has on $\arg\mathbf{\Gamma}$.

This result is of limited practical use, though, since bounds on the magnitudes of $\mathbf{\Gamma_1}$ and $\mathbf{\Gamma_2}$ are not easily predicted without detailed knowledge of the construction and geometry of the machine in use. Suffice it to say that as the saliency ratio tends to unity, $\arg\mathbf{\Gamma}$, and thereby the estimate $\hat{\theta}_r$, will be determined not by the actual rotor position $\theta_r$, but by $\arg\mathbf{\Gamma_1}$ instead.

| | | |
|---|---|---|
| $c_1$ | 477 | $\mathrm{H}^{-1}$ |
| $c_2$ | 22.7 | $\mathrm{H}^{-1}$ |
| $Q$ | 15.8 | mA/LSB |
| $\phi_q$ | 1 | deg |
| $T_{\mathrm{DT}}$ | 4 | µs |
| $T_f$ | 15.9 | µs |
| $T_{\mathrm{aq}}$ | 23.6 | µs |
| $d_p$ | 43.5 | % |
| $f_u$ | 500 | Hz |

Table 5.1.: Parameters for the INFORM method (Siemens motor).

### 5.2.4. Measurement Results, Siemens Motor

For the Siemens motor, Table 5.1 shows the relevant parameters for the INFORM method. The estimation rate $f_u$ is set to 500 Hz in order to gauge the performance of the estimation algorithm during motor transients. This rate is naturally much higher than would be required for low-speed operation.

**Figure 5.11:** With no load, the motor is manually turned slowly through a mechanical revolution and $\mathbf{\Gamma}$ is sampled at 5° intervals. The figure shows the locus of $\mathbf{\Gamma}$ and the tracking performance of the INFORM algorithm. As seen, the estimation error $\tilde{\theta}_r$ is approximately in the range $[-15°; 15°]$.

**Figure 5.12:** Same test as with Figure 5.11, but with a bias current of $10e^{j0°}$ A, approximately one third of its rated value, present while the motor is turned through a mechanical revolution. The figure shows the measured effect that saturation has on the locus of $\mathbf{\Gamma}$ and the resulting degradation of the tracking performance of the INFORM algorithm. Varying the angle of the bias current gives similar results.

Table 5.1 gives an insight into why the Siemens motor is also ill-suited for sensorless control based on the INFORM algorithm. The relative magnitudes of $c_1$ and $c_2$ determine how great an impact saturation can have on the locus of $\mathbf{\Gamma}$. If $c_1$ is much larger in value than $c_2$, the small relative differences between $c_{1A}$, $c_{1B}$ and $c_{1C}$ can potentially produce a vector $\mathbf{\Gamma_1}$ that is large in magnitude compared to $\mathbf{\Gamma_2}$. For the Siemens motor, the offset produced by $\mathbf{\Gamma_1}$ is considerable, as shown in Figure 5.12, even at a relatively low current level for the machine.

As the algorithm fails to track the rotor position under these static conditions, we conclude that dynamic load testing of the Siemens motor is not possible using the INFORM method presented here.

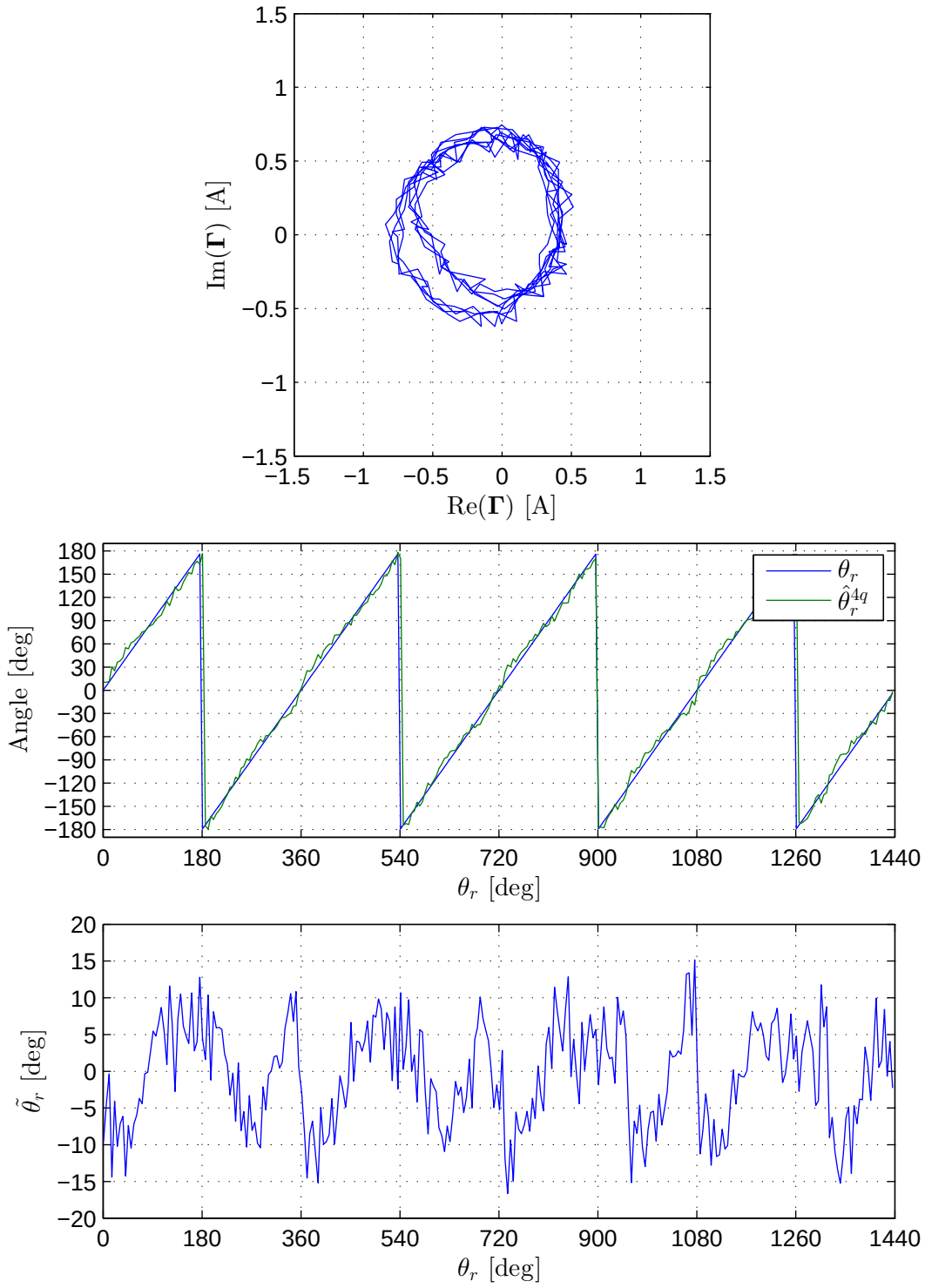


Figure 5.11.: Locus of $\mathbf{\Gamma}$ and resulting tracking performance. No load (INFORM, Siemens motor).

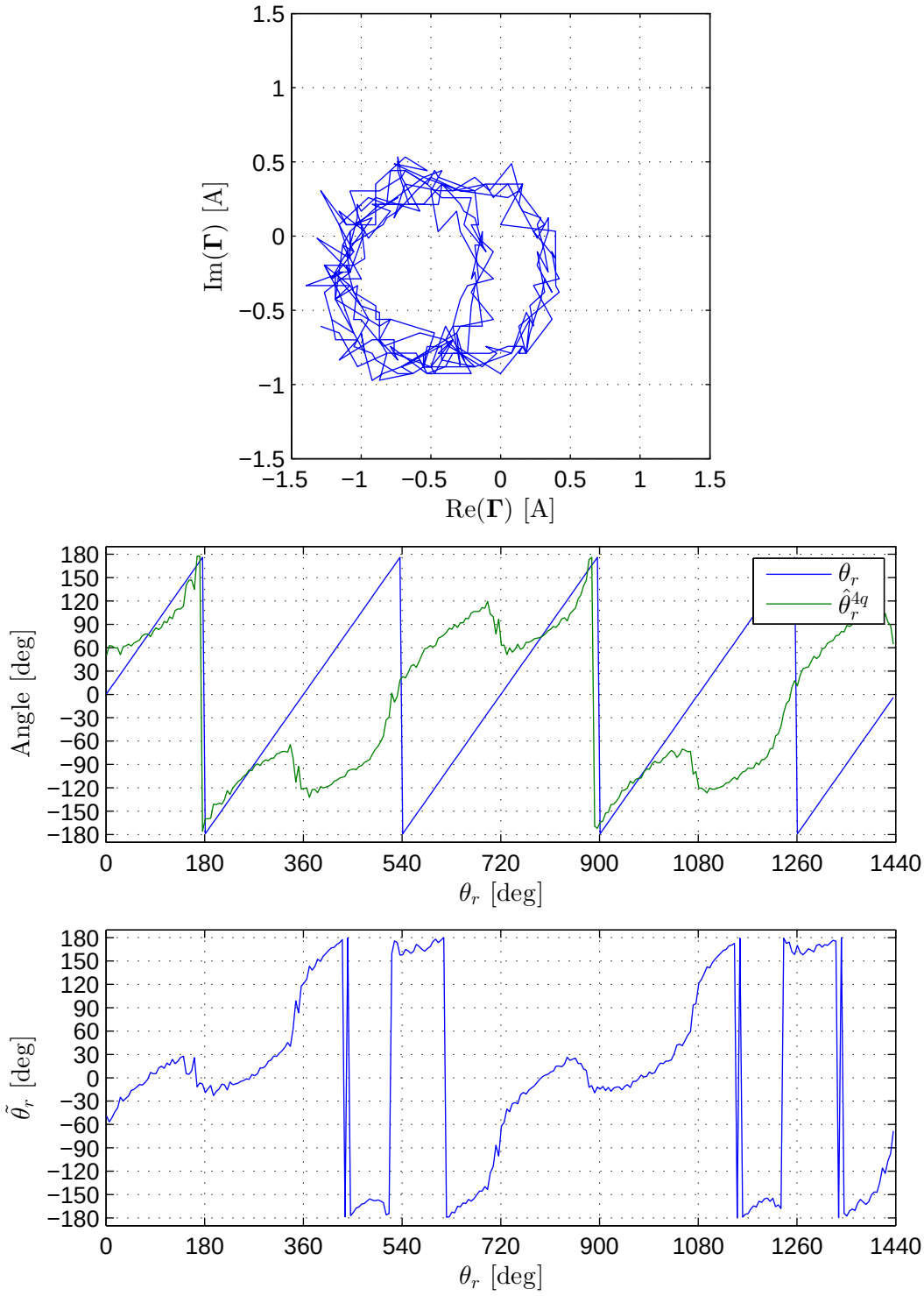


Figure 5.12.: Locus of $\mathbf{\Gamma}$ and resulting tracking performance. Bias current of $10e^{j0^\circ}$A (INFORM, Siemens motor).

| | | |
|---|---|---|
| $c_1$ | 82.5 | $\mathrm{H}^{-1}$ |
| $c_2$ | 17.5 | $\mathrm{H}^{-1}$ |
| $Q$ | 15.8 | mA/LSB |
| $\phi_q$ | 1 | deg |
| $T_{\mathrm{DT}}$ | 4 | µs |
| $T_f$ | 15.9 | µs |
| $T_{\mathrm{aq}}$ | 30.5 | µs |
| $d_p$ | 50.5 | % |
| $f_u$ | 500 | Hz |

Table 5.2.: Parameters for the INFORM method (SEM motor).

### 5.2.5. Measurement Results, SEM Motor

For the SEM motor, Table 5.2 shows the relevant parameters for the INFORM method.

**Figure 5.13:** As with the Siemens motor, with no load, the motor is manually turned slowly through a mechanical revolution and $\mathbf{\Gamma}$ is sampled at 5° intervals. The figure shows the locus of $\mathbf{\Gamma}$ and the tracking performance of the INFORM algorithm. As seen, the estimation error $\tilde{\theta}_r$ is again in the range $[-15°; 15°]$, although the algorithm performs slightly better here than with the Siemens motor.

**Figure 5.14:** Same test as with Figure 5.13, but with a bias current of $1.5e^{j0°}$ A, approximately one third of its rated value, present while the motor is turned through a mechanical revolution. In contrast to the Siemens motor, the locus of $\mathbf{\Gamma}$ is here hardly affected by the bias current, and the estimation error $\tilde{\theta}_r$ remains in the range $[-15°; 15°]$. Varying the angle of the bias current gives similar results. As seen from Table 5.2, for the SEM motor, the difference between $c_1$ and $c_2$ is also significantly lower than for the Siemens motor.

**Figures 5.15 and 5.16:** These figures show the tracking performance of the INFORM algorithm at no load under field-oriented control[1] with a constant velocity reference. Note that the load current peaks are samples from the INFORM periods and are not seen by the FOC loop. The tracking performance at 2 RPM and 50 RPM is similar and is seemingly more accurate than with the static tests of Figures 5.13 and 5.14, but note that only a fraction of a mechanical revolution is traversed in Figures 5.15 and 5.16.

[1] Current control in the FOC loop is implemented, without decoupling, with a pair of proportional-integral controllers for the direct and quadrature current components, respectively. An outer PI loop forms the necessary cascade configuration for velocity control. All controllers are heuristically tuned with the Ziegler-Nichols method for quarter-wave decay.

**Figures 5.17 and 5.18:** From 125 RPM to 175 RPM, the tracking performance of the INFORM algorithm degrades significantly. Recall that the derivation of the INFORM method is based on the low-speed model (4.2). As the name implies, the model is only a valid approximation at low speed, and at some point we should expect the neglected terms of (4.1) to influence the current response. Predicting the extent of this influence would require a general solution of (4.1), which mathematically poses a significantly more difficult problem. We will here, for the SEM motor, consider 125 RPM to be an adequate speed margin for the INFORM algorithm to function correctly.

**Figure 5.19:** This figure shows the tracking performance during the transient state of reversing the velocity of the motor. As seen, for a peak load current of approximately 2 A, the transient has little impact on the estimation error $\tilde{\theta}_r$ of the INFORM algorithm.

**Figure 5.20:** For a load current of approximately 2.5 A, the estimation error $\tilde{\theta}_r$ begins to show the effect of magnetic saturation. For a load current between 2.5 A and 4 A, approximately the rated current of the SEM motor, the estimation error is in the range $[-25°; 25°]$.

**Figure 5.21:** Shifting the load current above the rated current of the SEM motor by approximately 1 A degrades the tracking performance of the INFORM algorithm significantly.

As the measurement results show, compared to that of the Siemens motor, the load current generally affects the tracking performance of the INFORM algorithm to a much lesser extent for the SEM motor, which can be seen as an effect of the large difference in saliency ratios of the motors.

## 5.3. Sector Estimation

With the INFORM method and interperiod sampling, we have an algorithm that can estimate the angular position of the rotor and is robust to the inverter voltage error. Its accuracy, however, is affected by load current, as shown in Section 5.2.5.

Here we will present a new algorithm that makes use of the same fundamentals as the INFORM method, but is not affected by magnetic saturation, and does not require interperiod sampling.

Consider again the current increment:

$$\Delta \mathbf{i_s} = \left( c_1 \mathbf{v_s} + c_2 \overline{\mathbf{v_s}} e^{j2\theta_r} \right) \Delta t \qquad \text{(5.17 revisited)}$$

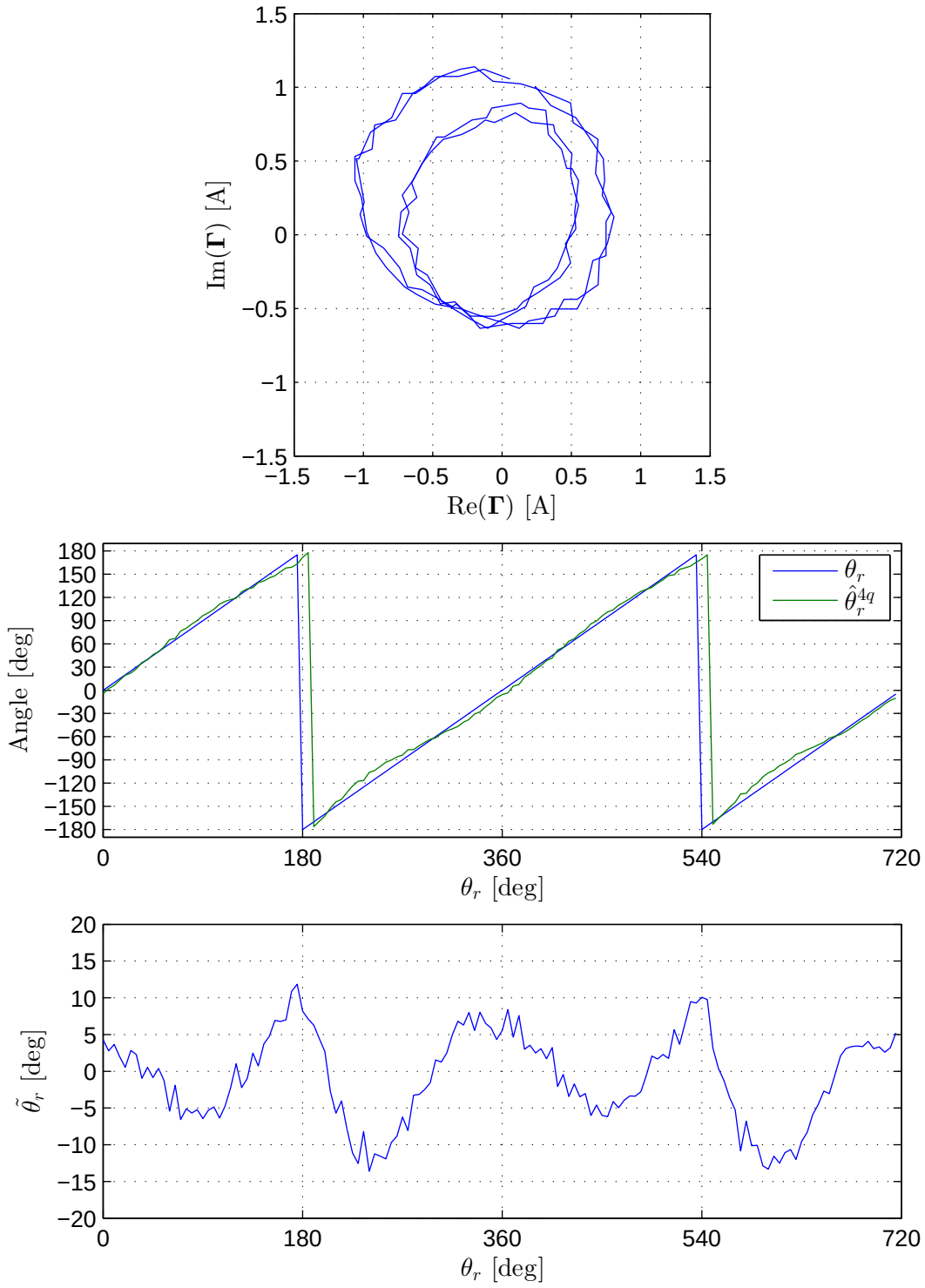


Figure 5.13.: Locus of $\mathbf{\Gamma}$ and resulting tracking performance. No load (INFORM, SEM motor).

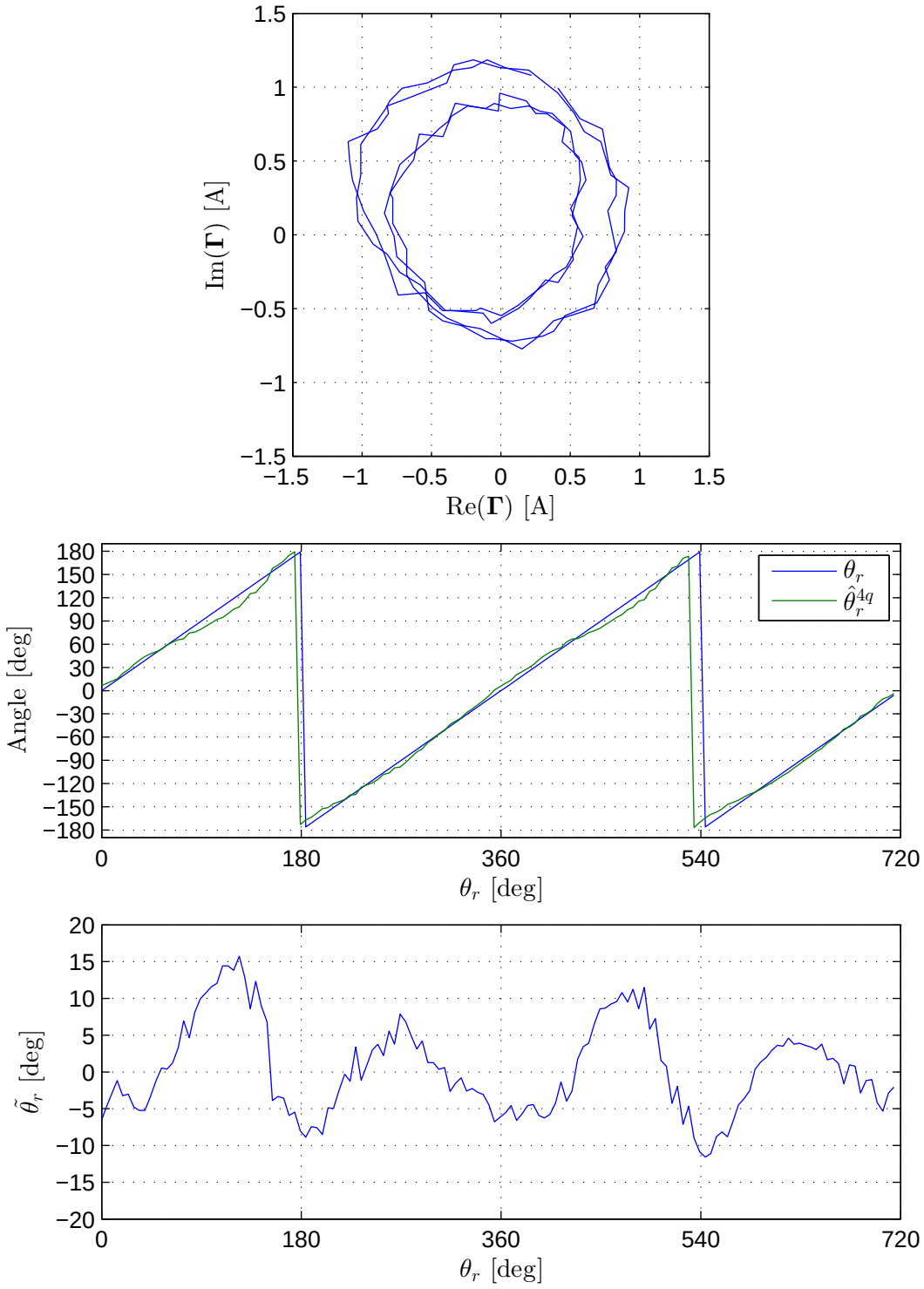


Figure 5.14.: Locus of $\mathbf{\Gamma}$ and resulting tracking performance. Bias current of $1.5e^{j0^\circ}$A (INFORM, SEM motor).

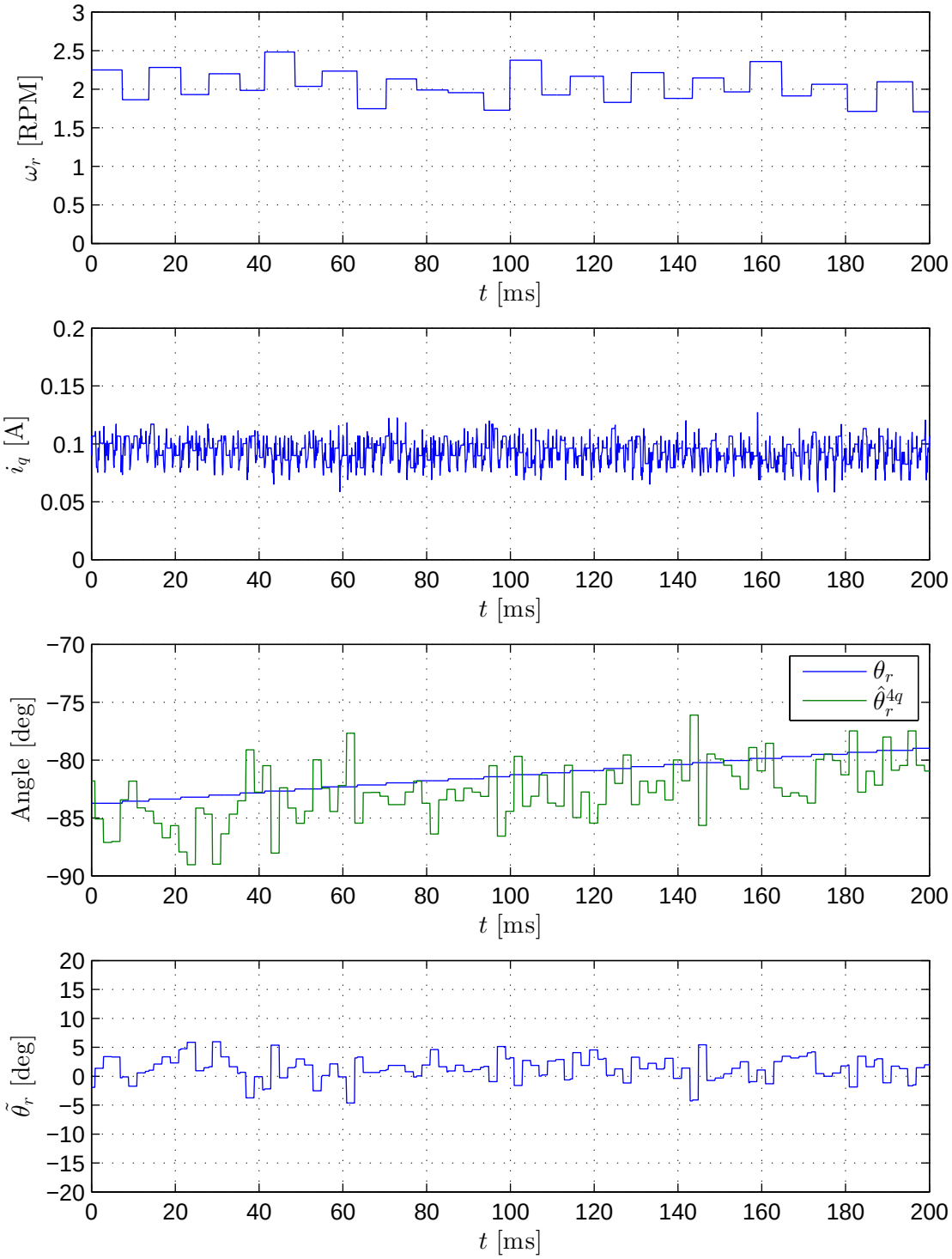


Figure 5.15.: Tracking performance under FOC. Reference velocity of 2 RPM (INFORM, SEM motor).

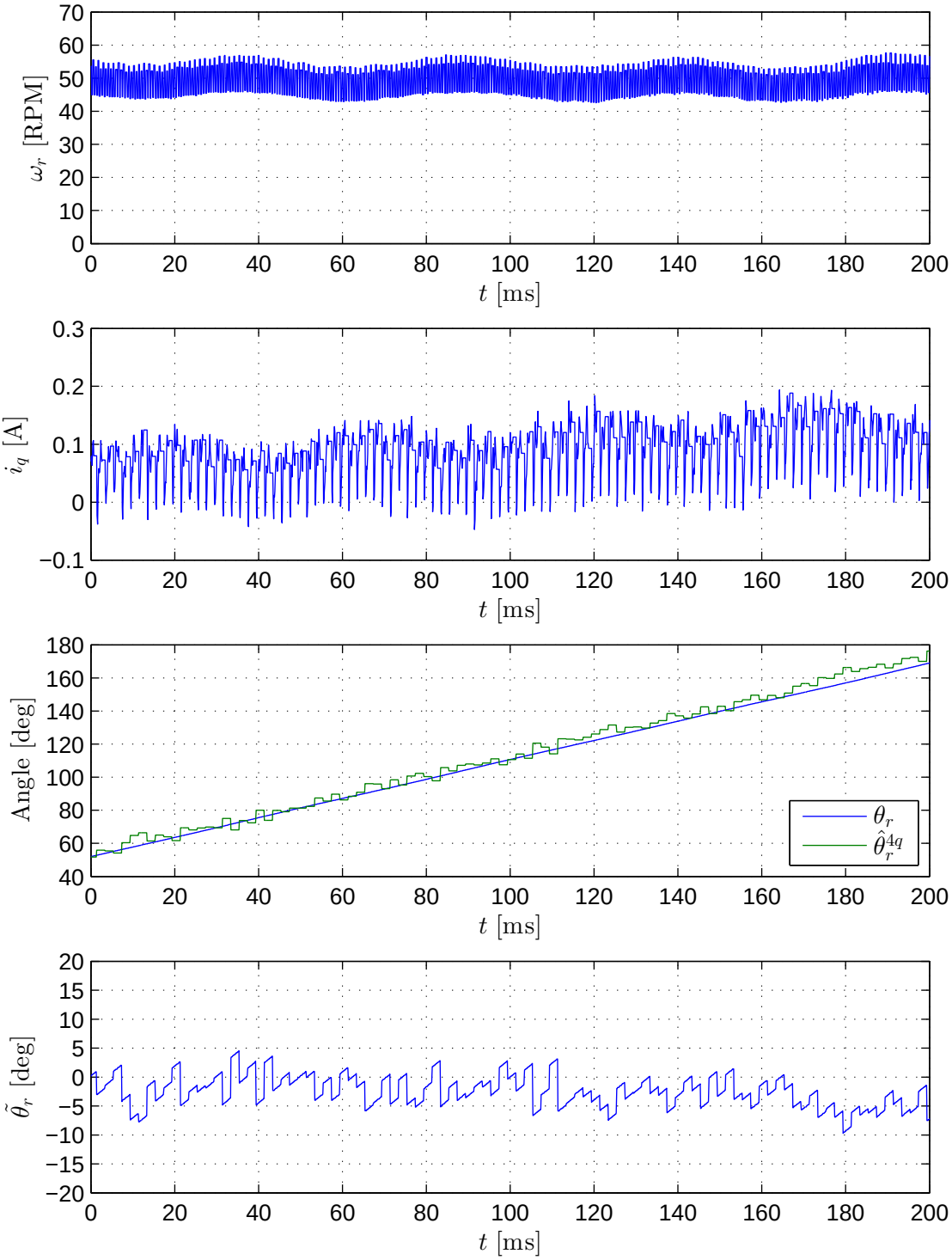


Figure 5.16.: Tracking performance under FOC. Reference velocity of 50 RPM (INFORM, SEM motor).

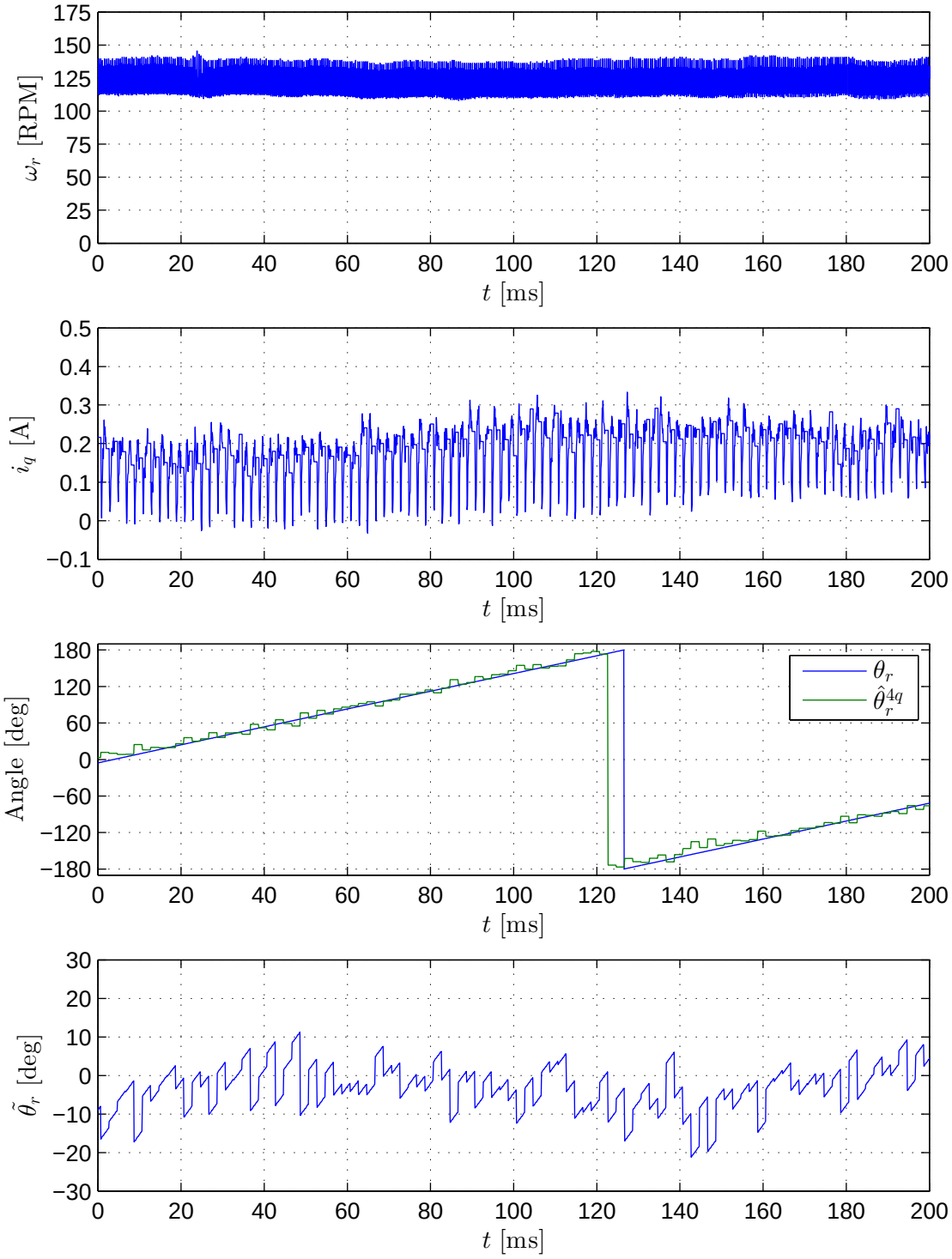


Figure 5.17.: Tracking performance under FOC. Reference velocity of 125 RPM (INFORM, SEM motor).

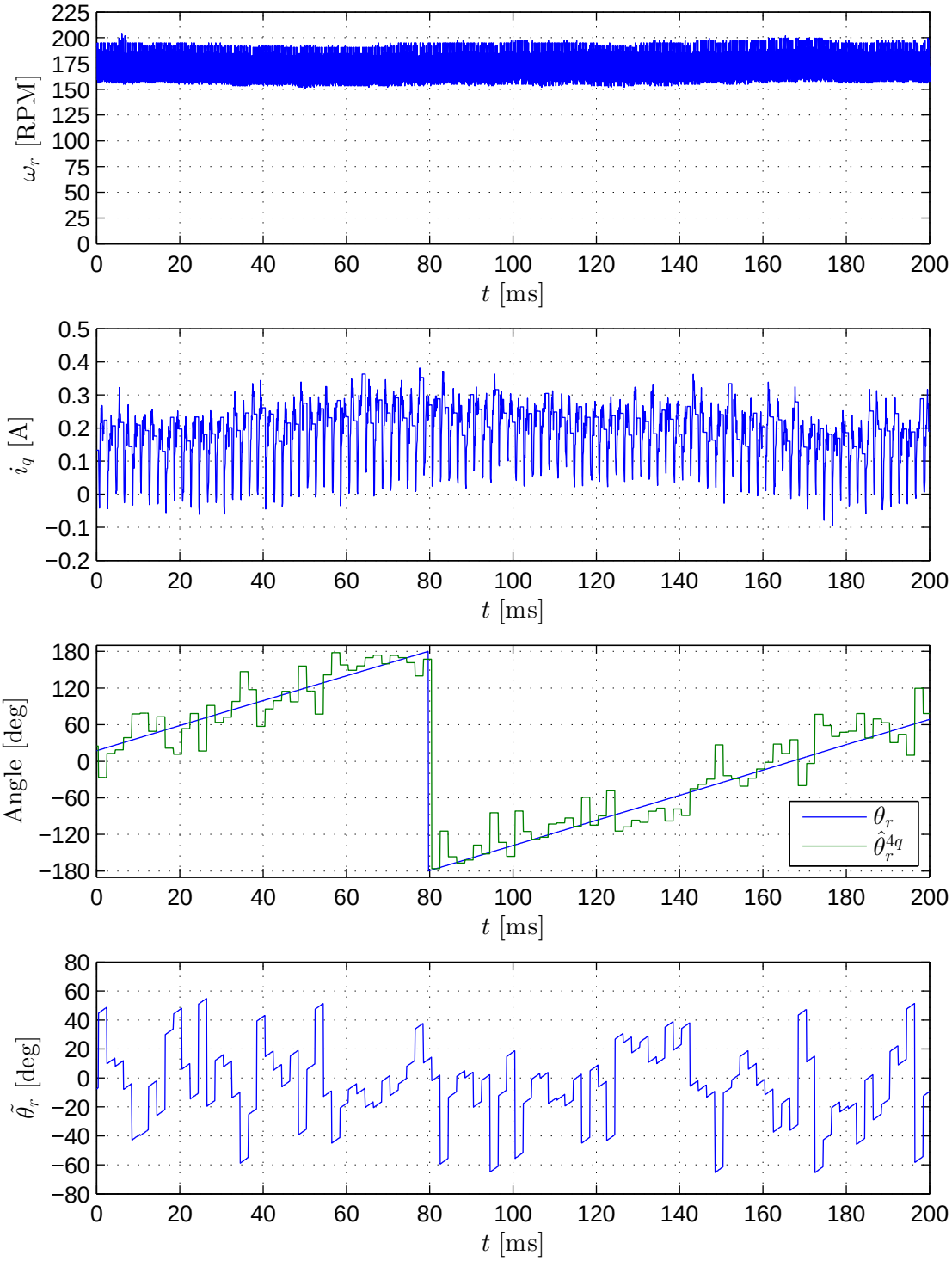


Figure 5.18.: Tracking performance under FOC. Reference velocity of 175 RPM (INFORM, SEM motor).

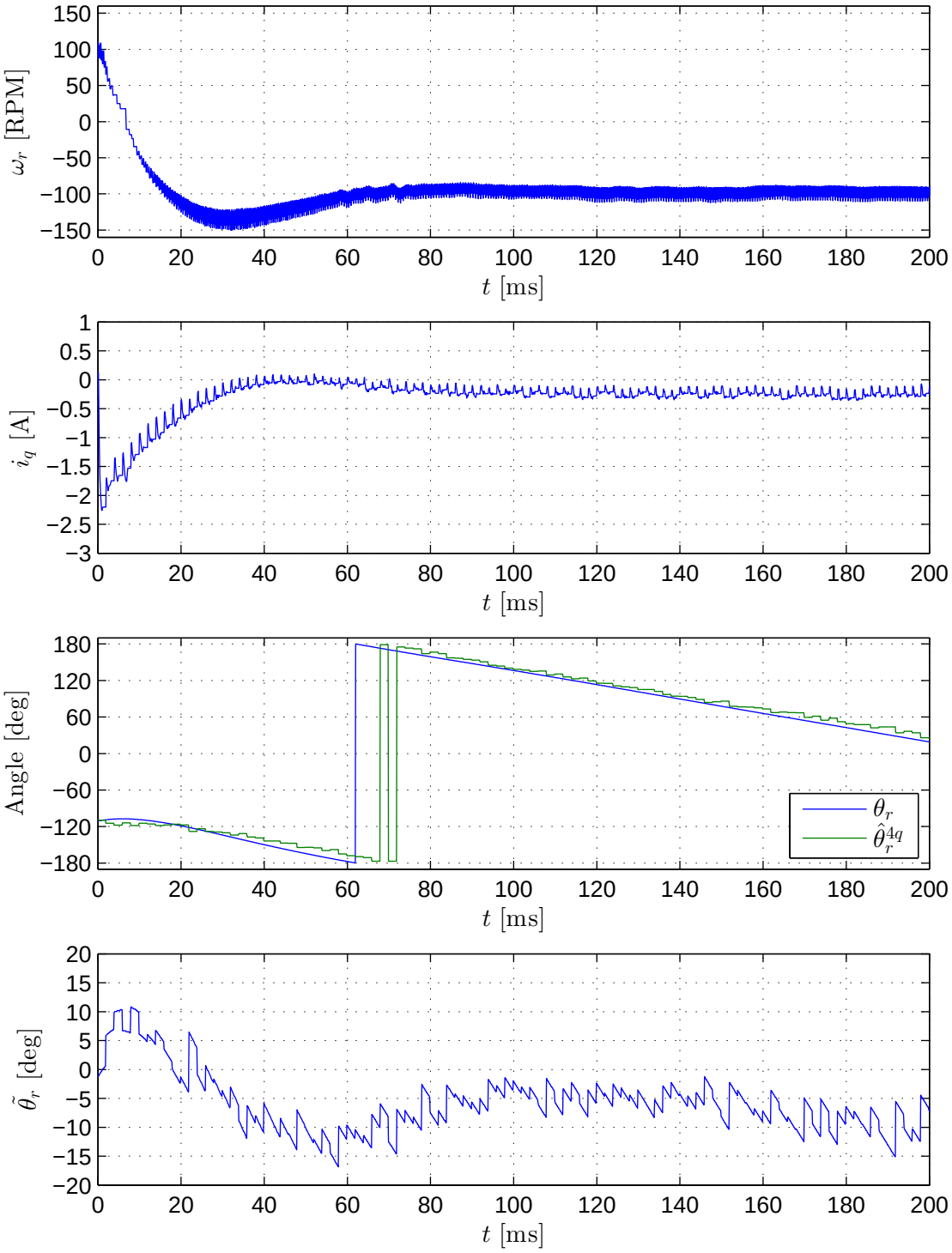


Figure 5.19.: Tracking performance under FOC. Step change in reference velocity of 100 RPM to −100 RPM (INFORM, SEM motor).

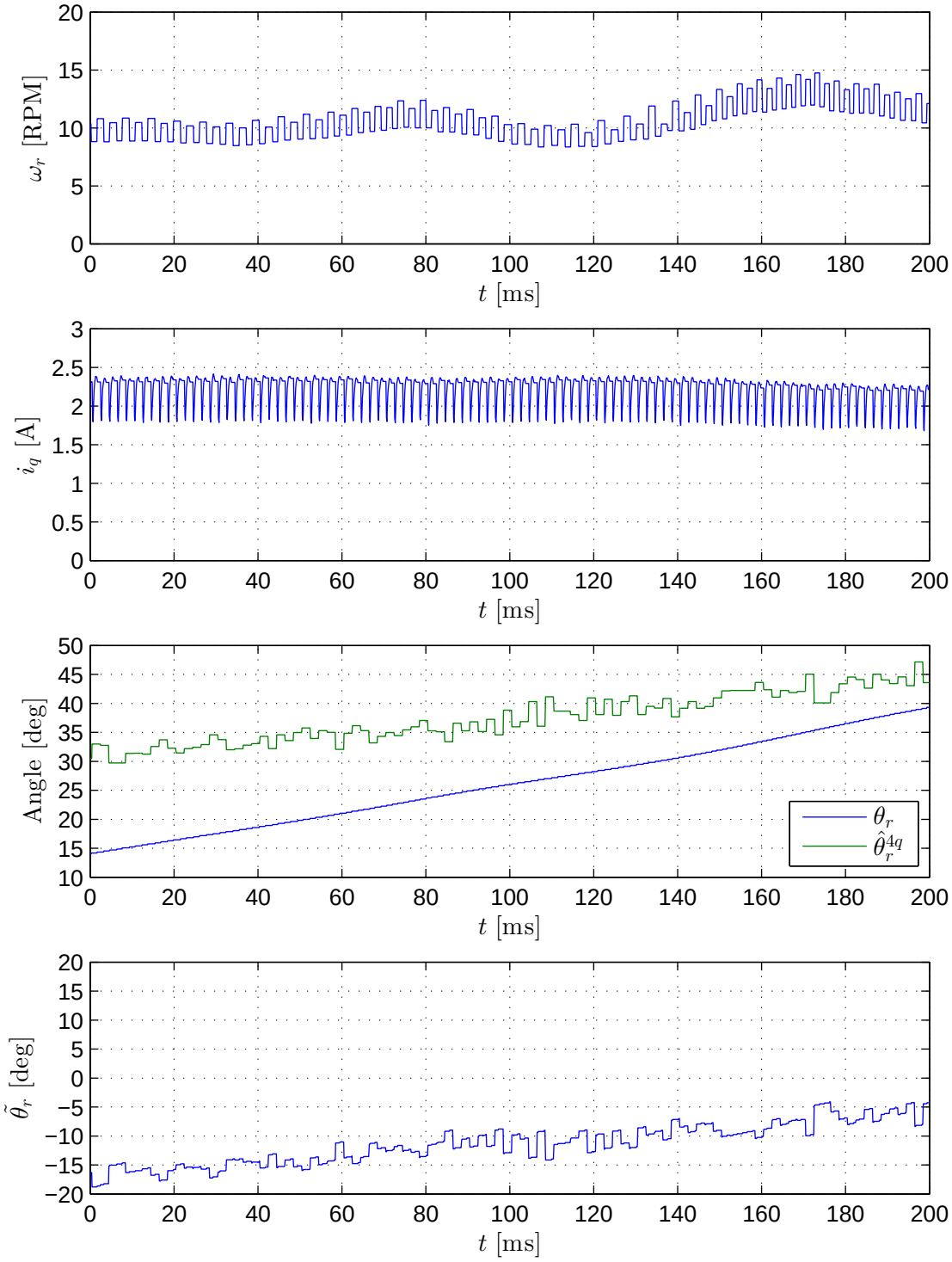


Figure 5.20.: Tracking performance under FOC. Reference velocity of 10 RPM. Load current of approximately 2.5 A (INFORM, SEM motor).

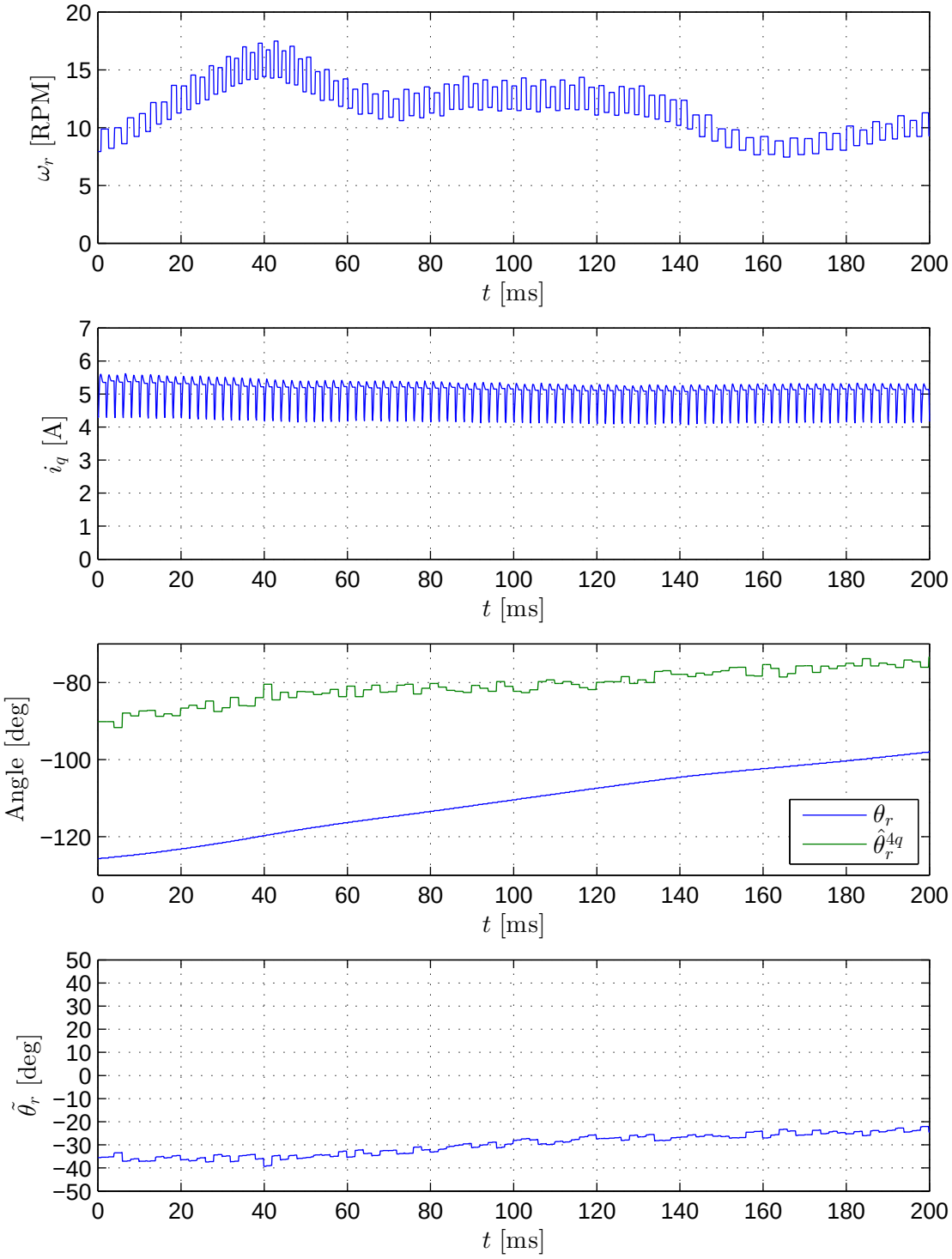


Figure 5.21.: Tracking performance under FOC. Reference velocity of 10 RPM. Load current of approximately 5 A (INFORM, SEM motor).

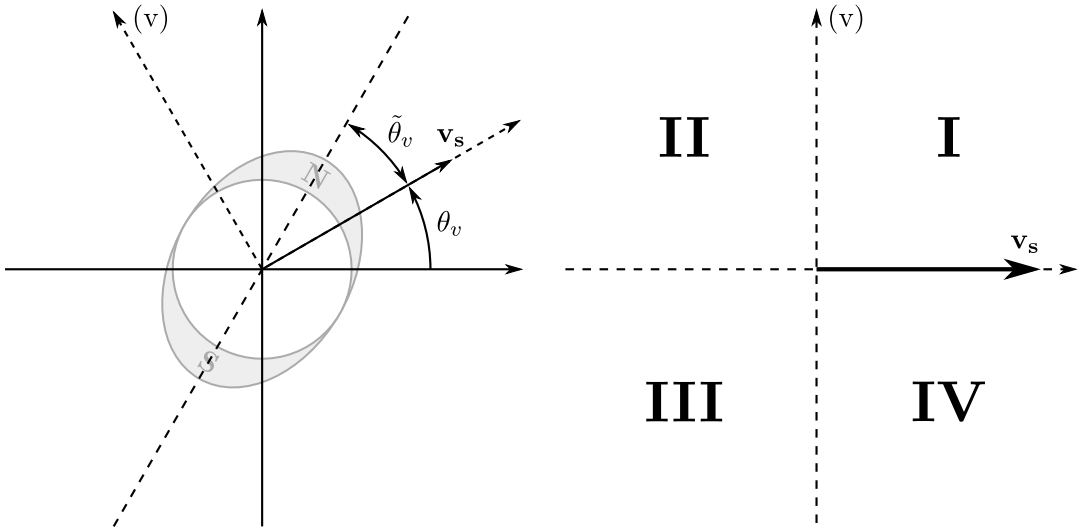


(a) Reference frame (v) (b) Quadrants of (v)

Figure 5.22.: Reference frame of injected voltage $\mathbf{v_s}$.

If we have:

$$\mathbf{v_s} = V_s e^{j\theta_v} \tag{5.45}$$

Then under the reference frame transformation:

$$\mathbf{k}^{(\mathrm{v})} = \mathbf{k} e^{-j\theta_v} \Leftrightarrow \mathbf{k} = \mathbf{k}^{(\mathrm{v})} e^{j\theta_v} \tag{5.46}$$

where $\mathbf{k}^{(\mathrm{v})}$ is $\mathbf{k}$ as seen from the reference frame of the injected voltage, (5.17) becomes:

$$\begin{aligned} \Delta\mathbf{i}_\mathbf{s}^{(\mathrm{v})} e^{j\theta_v} &= \left( c_1 \mathbf{v}_\mathbf{s}^{(\mathrm{v})} e^{j\theta_v} + c_2 \overline{\mathbf{v}_\mathbf{s}^{(\mathrm{v})} e^{j\theta_v}} e^{j2\theta_r} \right) \Delta t \\ &= \left( c_1 V_s e^{j\theta_v} + c_2 V_s e^{-j\theta_v} e^{j2\theta_r} \right) \Delta t \Leftrightarrow \end{aligned} \tag{5.47}$$

$$\begin{aligned} \Delta\mathbf{i}_\mathbf{s}^{(\mathrm{v})} &= V_s \Delta t \left( c_1 + c_2 e^{j2(\theta_r - \theta_v)} \right) \\ &= V_s \Delta t \left( c_1 + c_2 e^{j2\tilde{\theta}_v} \right) \end{aligned} \tag{5.48}$$

where:

$$\tilde{\theta}_v = \theta_r - \theta_v \tag{5.49}$$

Eq. (5.49) is illustrated with an example in Figure 5.22a. For the quadrants of reference frame (v), shown in Figure 5.22b, we have then:

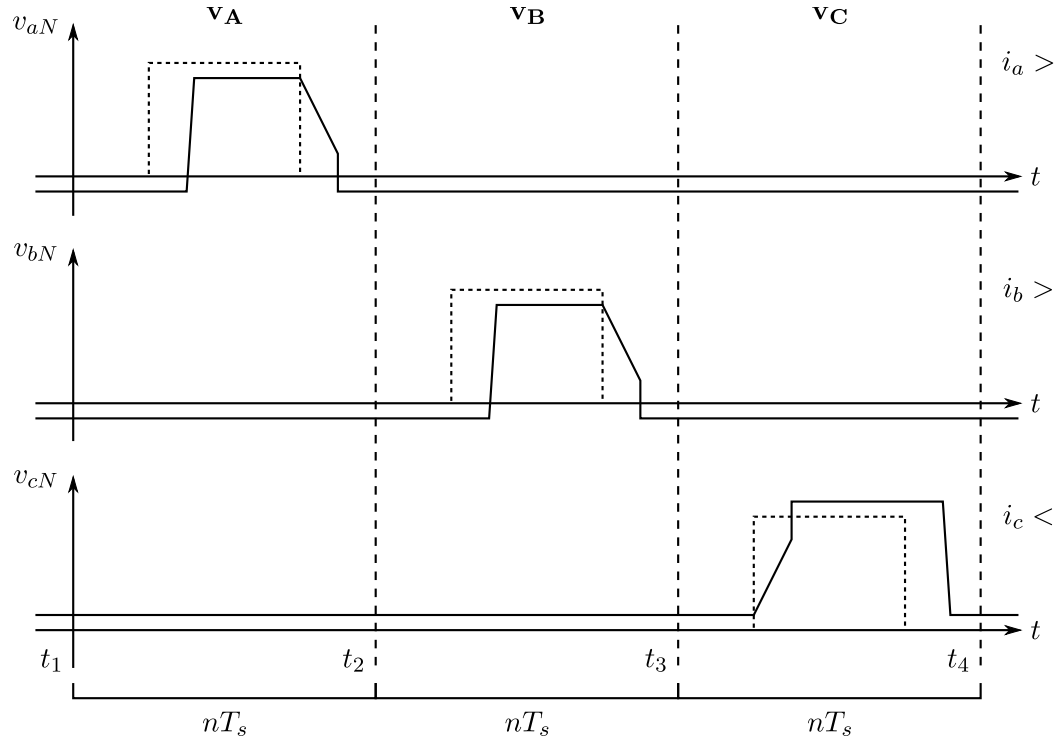


Figure 5.23.: Sequential injection of the three, phase-aligned voltage vectors with sample period $nT_s$.

$$\tilde{\theta}_v \in \mathbf{I} \Rightarrow \arg \Delta \mathbf{i}_\mathbf{s}^{(\mathrm{v})} > 0 \tag{5.50a}$$

$$\tilde{\theta}_v \in \mathbf{II} \Rightarrow \arg \Delta \mathbf{i}_\mathbf{s}^{(\mathrm{v})} < 0 \tag{5.50b}$$

$$\tilde{\theta}_v \in \mathbf{III} \Rightarrow \arg \Delta \mathbf{i}_\mathbf{s}^{(\mathrm{v})} > 0 \tag{5.50c}$$

$$\tilde{\theta}_v \in \mathbf{IV} \Rightarrow \arg \Delta \mathbf{i}_\mathbf{s}^{(\mathrm{v})} < 0 \tag{5.50d}$$

From the sign of $\arg \Delta \mathbf{i}_\mathbf{s}^{(\mathrm{v})}$, we can thus determine if the axis of the rotor is in quadrants **I**,**III** or **II**,**IV** relative to the injection angle $\theta_v$.

Note that the sign of $\arg \Delta \mathbf{i}_\mathbf{s}^{(\mathrm{v})}$ depends only on the rotor position $\theta_r$ and injection angle $\theta_v$, and not $c_1$, $c_2$ and $V_s$. As per Section 5.1, $\theta_v$ is something we can accurately control without the need for interperiod sampling.

If we now sequentially inject the three, phase-aligned voltage vectors, as shown in Figure 5.23, we have:

$$\mathbf{v_s} = \mathbf{v_A} = \frac{2}{3}\left(v_{aN}^* + \tilde{v}_{aN}\right), \qquad t_1 \leq t < t_2 \tag{5.51a}$$

$$\mathbf{v_s} = \mathbf{v_B} = \frac{2}{3}\left(v_{bN}^* + \tilde{v}_{bN}\right)\mathbf{a}, \qquad t_2 \leq t < t_3 \tag{5.51b}$$

$$\mathbf{v_s} = \mathbf{v_C} = \frac{2}{3}\left(v_{cN}^* + \tilde{v}_{cN}\right)\mathbf{a^2}, \quad t_3 \leq t < t_4 \tag{5.51c}$$

The current response to (5.51) is then given by:

$$\Delta\mathbf{i}_{\mathbf{A}}^{(\mathrm{a})} = |\mathbf{v_A}|T_s\left(c_1 + c_2 e^{j2\theta_r}\right) \tag{5.52}$$

$$\Delta\mathbf{i}_{\mathbf{B}}^{(\mathrm{b})} = |\mathbf{v_B}|T_s\left(c_1 + c_2 e^{j2(\theta_r - 120^\circ)}\right) \tag{5.53}$$

$$\Delta\mathbf{i}_{\mathbf{C}}^{(\mathrm{c})} = |\mathbf{v_C}|T_s\left(c_1 + c_2 e^{j2(\theta_r + 120^\circ)}\right) \tag{5.54}$$

where (a), (b) and (c) are reference frames aligned with the phase axes.

If we let:

$$v_{pN}^* = v_{aN}^* = v_{bN}^* = v_{cN}^* = d_p V_{\mathrm{DC}} \tag{5.55}$$

We have:

$$v_{pN}^* + \tilde{v}_{pN} \gtrapprox d_p V_{\mathrm{DC}} - \frac{T_{\mathrm{DT}}}{T_s}V_{\mathrm{DC}} = \left(d_p - \frac{T_{\mathrm{DT}}}{T_s}\right)V_{\mathrm{DC}} \tag{5.56}$$

And for:

$$\begin{aligned}\mathbf{k} &= V_s \Delta t c_2 e^{j2\tilde{\theta}_v} \\ &= \left(v_{pN}^* + \tilde{v}_{pN}\right) n T_s c_2 e^{j2\tilde{\theta}_v} \\ &= \left(d_p - \frac{T_{\mathrm{DT}}}{T_s}\right) V_{\mathrm{DC}} n T_s c_2 e^{j2\tilde{\theta}_v}\end{aligned} \tag{5.57}$$

We can then again determine $d_p$ from a constraint on the quantization angle:

$$\tan\phi_q = \frac{q}{|\mathbf{k}|} = \frac{q}{\left(d_p - \frac{T_{\mathrm{DT}}}{T_s}\right)V_{\mathrm{DC}} n T_s c_2} \Leftrightarrow \tag{5.58}$$

$$\begin{aligned}d_p &= \frac{q}{V_{\mathrm{DC}} n T_s c_2 \tan\phi_q} + \frac{T_{\mathrm{DT}}}{T_s} \\ &= \frac{2}{3}\frac{Q}{V_{\mathrm{DC}} n T_s c_2 \tan\phi_q} + \frac{T_{\mathrm{DT}}}{T_s}\end{aligned} \tag{5.59}$$

Figure 5.24 shows the result of overlaying the quadrants of reference frames (a), (b) and (c). As seen, this effectively divides the plane into twelve, 30° sectors. If we now let $\theta_r$

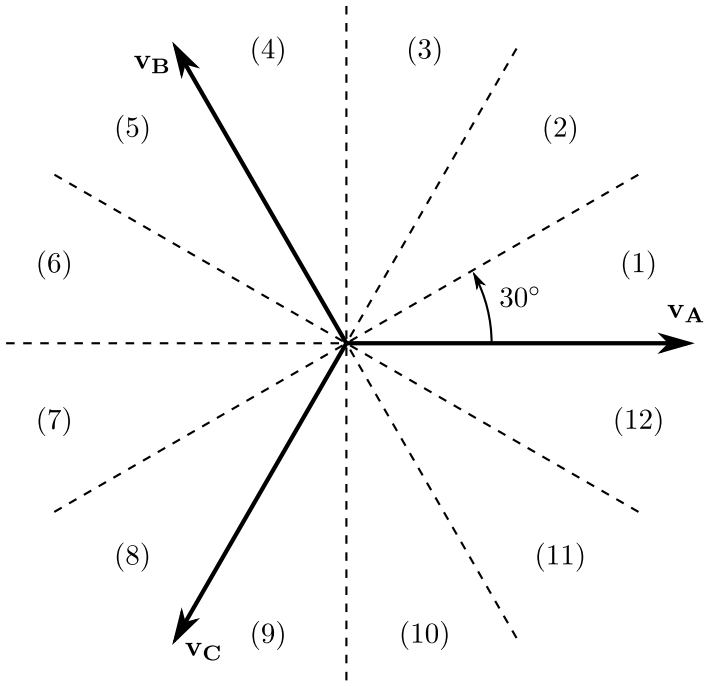


Figure 5.24.: Superposition of quadrants of reference frames (a), (b) and (c).

| $\theta_r$ in sector | Nom. angle [deg] | sgn $\left(\arg \Delta\mathbf{i}_\mathbf{A}^{(a)}\right)$ | sgn $\left(\arg \Delta\mathbf{i}_\mathbf{B}^{(b)}\right)$ | sgn $\left(\arg \Delta\mathbf{i}_\mathbf{C}^{(c)}\right)$ |
|---|---|---|---|---|
| 1 | 15 | 1 | 1 | −1 |
| 2 | 45 | 1 | −1 | −1 |
| 3 | 75 | 1 | −1 | 1 |
| 4 | 105 | −1 | −1 | 1 |
| 5 | 135 | −1 | 1 | 1 |
| 6 | 165 | −1 | 1 | −1 |
| 7 | −165 | 1 | 1 | −1 |
| 8 | −135 | 1 | −1 | −1 |
| 9 | −105 | 1 | −1 | 1 |
| 10 | −75 | −1 | −1 | 1 |
| 11 | −45 | −1 | 1 | 1 |
| 12 | −15 | −1 | 1 | −1 |

Table 5.3.: Sequence of signs of the current increment angles as $\theta_r$ traverses 360°.

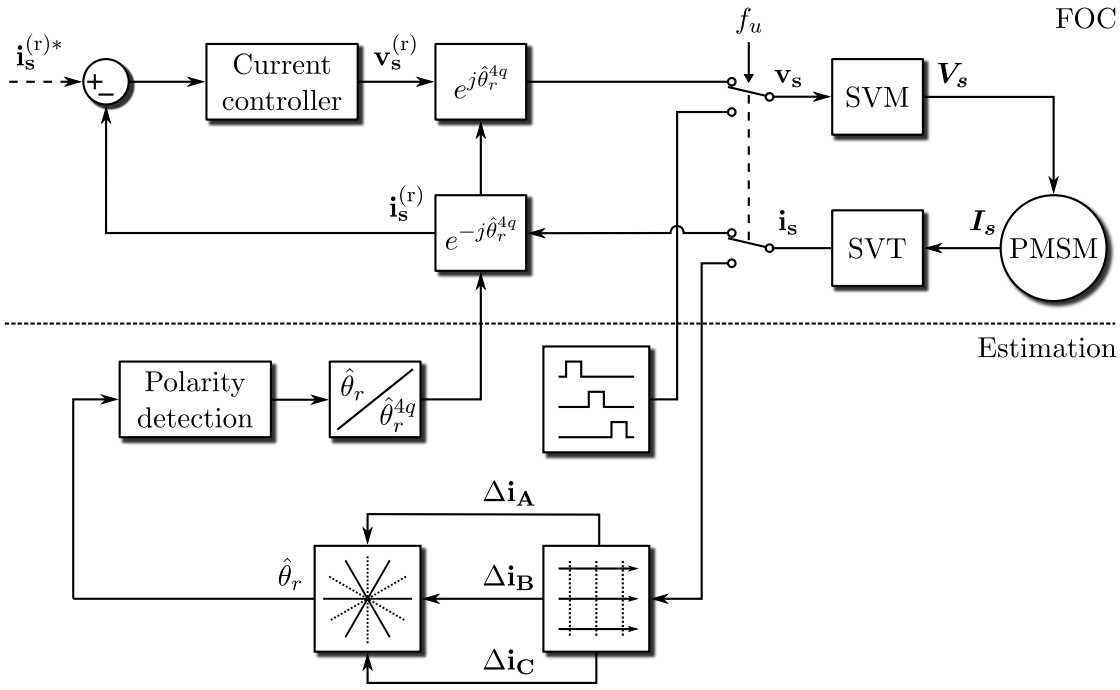


Figure 5.25.: Complete topology of the sector estimation algorithm.

traverse 360° in this plane, we can record the signs of $\arg \Delta\mathbf{i}_\mathbf{A}^{(a)}$, $\arg \Delta\mathbf{i}_\mathbf{B}^{(b)}$ and $\arg \Delta\mathbf{i}_\mathbf{C}^{(c)}$ as $\theta_r$ moves between sectors. Table 5.3 shows the result along with nominal angles for the sectors.

As seen in Table 5.3, as $\theta_r$ traverses 360°, a pattern emerges with a period of six sectors, or 180°, and within these six sectors the combination of signs of $\arg \Delta\mathbf{i}_\mathbf{A}^{(a)}$, $\arg \Delta\mathbf{i}_\mathbf{B}^{(b)}$ and $\arg \Delta\mathbf{i}_\mathbf{C}^{(c)}$ is unique. As expected, the combination only allows us to determine the position of the magnetic axis of the rotor. If the pattern did not repeat itself every 180°, we would be able to determine the polarity of the PM field as well.

Combining yet again the estimate $\hat{\theta}_r$, the state machine to determine $\hat{\theta}_r^{4q}$, polarity detection and a FOC topology yields the algorithm shown in Figure 5.25. $\hat{\theta}_r^{4q}$ is determined in order of:

1. Resolve the sector of $\theta_r$ from the combination of signs of the current increment angles[2]. The nominal angle of the sector gives an estimate $\hat{\theta}_r$ with a maximum estimation error of $\pm 15°$.

2. If uninitialized, detect field polarity by voltage pulse injection as shown in Section 4.3. Skip otherwise.

[2]The process of determining the sector from the combination of the current increment angles can be conveniently implemented as a simple lookup table.

| | | |
|---|---|---|
| $c_1$ | 477 | $\mathrm{H}^{-1}$ |
| $c_2$ | 22.7 | $\mathrm{H}^{-1}$ |
| $Q$ | 15.8 | mA/LSB |
| $\phi_q$ | 1 | deg |
| $T_{\mathrm{DT}}$ | 4 | µs |
| $nT_s$ | 100 | µs |
| $d_p$ | 51.1 | % |
| $f_u$ | 500 | Hz |

Table 5.4.: Parameters for sector estimation (Siemens motor).

| | | |
|---|---|---|
| $c_1$ | 82.5 | $\mathrm{H}^{-1}$ |
| $c_2$ | 17.5 | $\mathrm{H}^{-1}$ |
| $Q$ | 15.8 | mA/LSB |
| $\phi_q$ | 1 | deg |
| $T_{\mathrm{DT}}$ | 4 | µs |
| $nT_s$ | 100 | µs |
| $d_p$ | 65.1 | % |
| $f_u$ | 500 | Hz |

Table 5.5.: Parameters for sector estimation (SEM motor).

3. Process Algorithm 1 to determine $\hat{\theta}_r^{4q}$.

As with the INFORM method, sector estimation requires no filters.

### 5.3.1. Measurement Results, Siemens Motor

For the Siemens motor, Table 5.4 shows the relevant parameters for sector estimation.

From Figure 5.24 and Table 5.3, we have that, if $\theta_r$ starts out in a sector and moves counterclockwise, the current increments $\arg \Delta\mathbf{i}_{\mathbf{A}}^{(\mathrm{a})}$, $\arg \Delta\mathbf{i}_{\mathbf{B}}^{(\mathrm{b})}$ and $\arg \Delta\mathbf{i}_{\mathbf{C}}^{(\mathrm{c})}$ changes sign in sequence and is separated, ideally, by 30°. This is the basis for the sector estimation algorithm.

Figure 5.26 shows $\arg \Delta\mathbf{i}_{\mathbf{A}}^{(\mathrm{a})}$, $\arg \Delta\mathbf{i}_{\mathbf{B}}^{(\mathrm{b})}$ and $\arg \Delta\mathbf{i}_{\mathbf{C}}^{(\mathrm{c})}$ as the Siemens motor is manually turned slowly through a mechanical revolution. As seen from the figure, the zero crossings of $\arg \Delta\mathbf{i}_{\mathbf{A}}^{(\mathrm{a})}$, $\arg \Delta\mathbf{i}_{\mathbf{B}}^{(\mathrm{b})}$ and $\arg \Delta\mathbf{i}_{\mathbf{C}}^{(\mathrm{c})}$ have no clear sequence or angular separation and thus cannot provide the required signals for estimating the sector of $\theta_r$.

In general, we must conclude that, for its spatial variation in inductance, the Siemens servo motor does not posses the fundamental component required for the sensorless schemes presented here to function.

### 5.3.2. Measurement Results, SEM Motor

For the SEM motor, Table 5.5 shows the relevant parameters for sector estimation.

Figure 5.27 shows $\arg \Delta\mathbf{i}_{\mathbf{A}}^{(\mathrm{a})}$, $\arg \Delta\mathbf{i}_{\mathbf{B}}^{(\mathrm{b})}$ and $\arg \Delta\mathbf{i}_{\mathbf{C}}^{(\mathrm{c})}$ as the SEM motor is manually turned slowly through a mechanical revolution. Compared to that of the Siemens motor, the profile for the SEM motor shows both the proper sequence of zero crossings and clear angular separation between them.

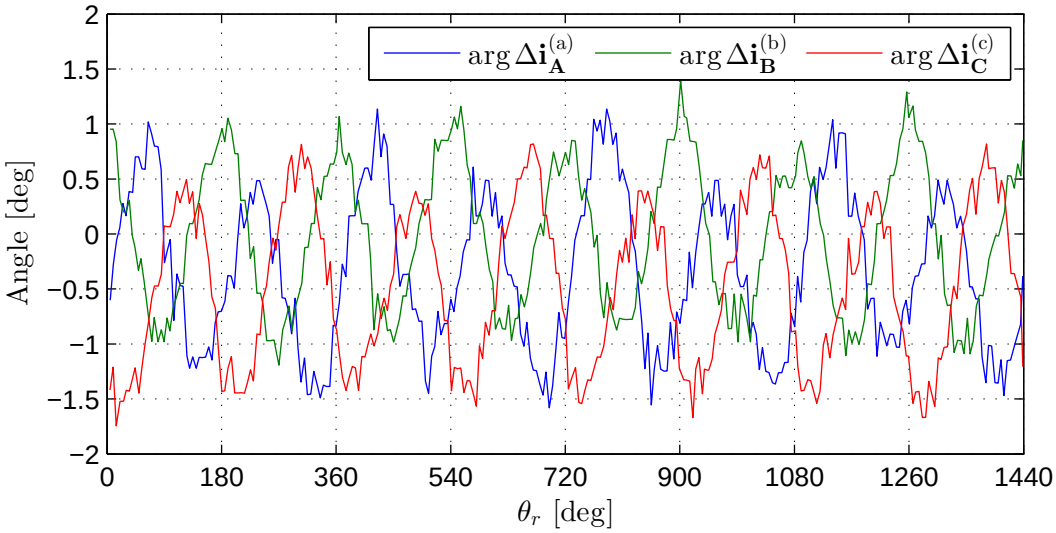


Figure 5.26.: Angle of current increments as $\theta_r$ traverses 360° mechanical (Siemens motor).

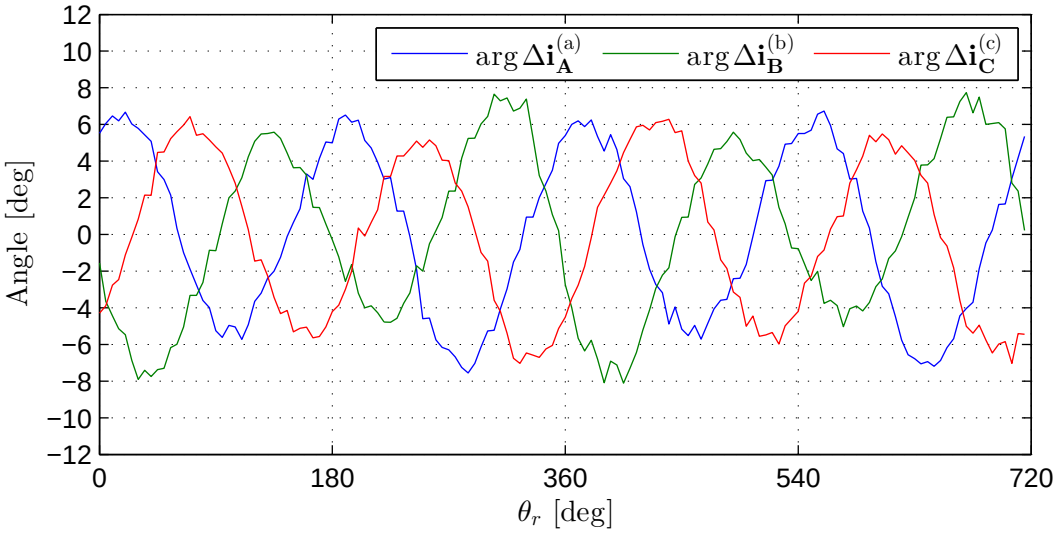


Figure 5.27.: Angle of current increments as $\theta_r$ traverses 360° mechanical (SEM motor).

**Figures 5.28 and 5.29:** The tracking performance of the sector estimation algorithm under field-oriented control is similar at 2 RPM and 50 RPM. The estimation error $\tilde{\theta}_r$ is generally in the range $[-20°; 20°]$. This is outside the range of $[-15°; 15°]$ predicted for an ideal machine, but we must allow for the possibility that, in practice, the machine is not perfectly symmetrical.

**Figures 5.30 and 5.31:** As is the case for the INFORM algorithm, from 125 RPM to 175 RPM, the tracking performance of the sector estimation algorithm degrades significantly.

**Figures 5.32–5.34** : For the velocity reversal transient and both the 2.5 A and 5 A load currents, the tracking performance of the sector estimation algorithm is unaffected. Compared to the INFORM algorithm, this could be a significant advantage.

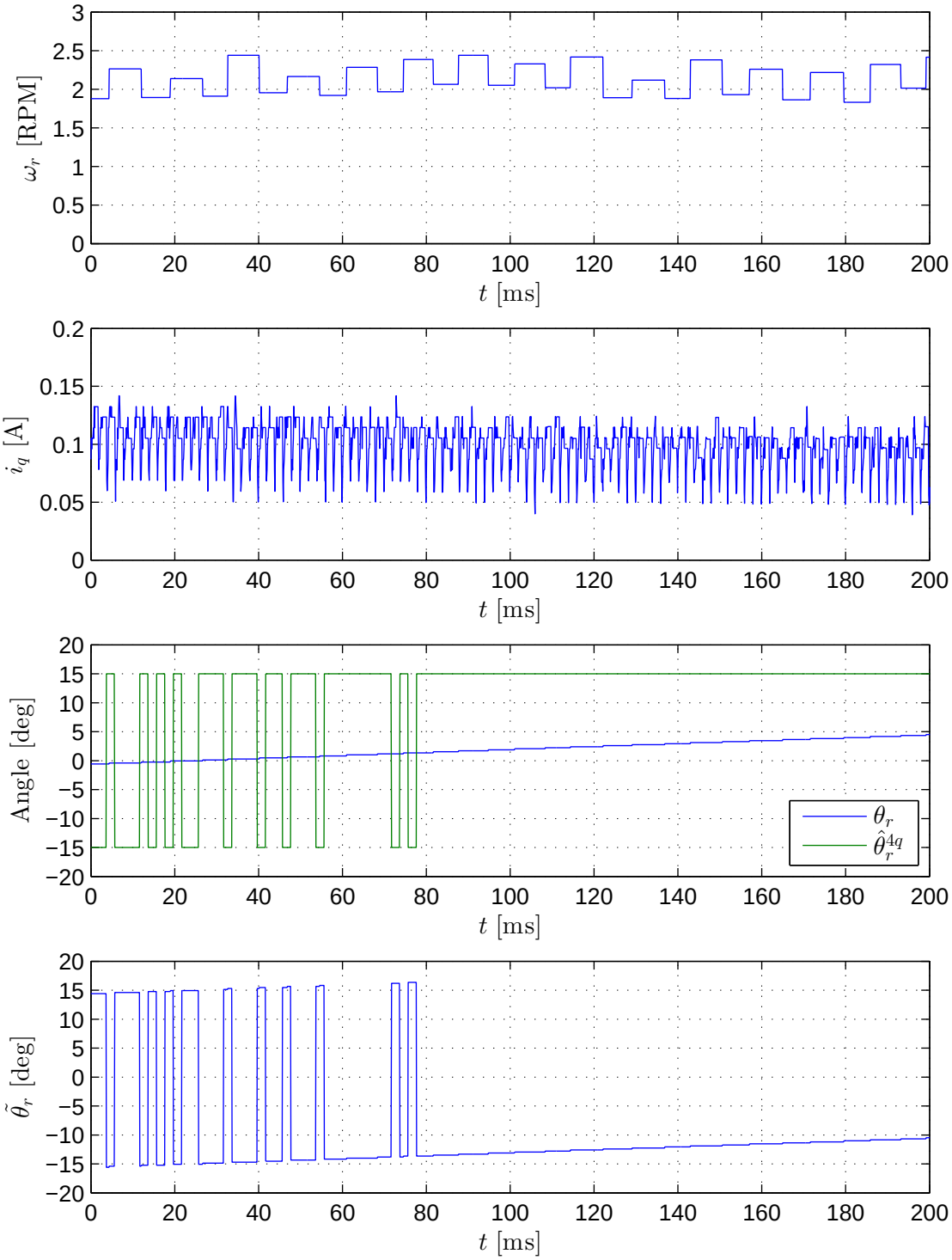


Figure 5.28.: Tracking performance under FOC. Reference velocity of 2 RPM (sector estimation, SEM motor).

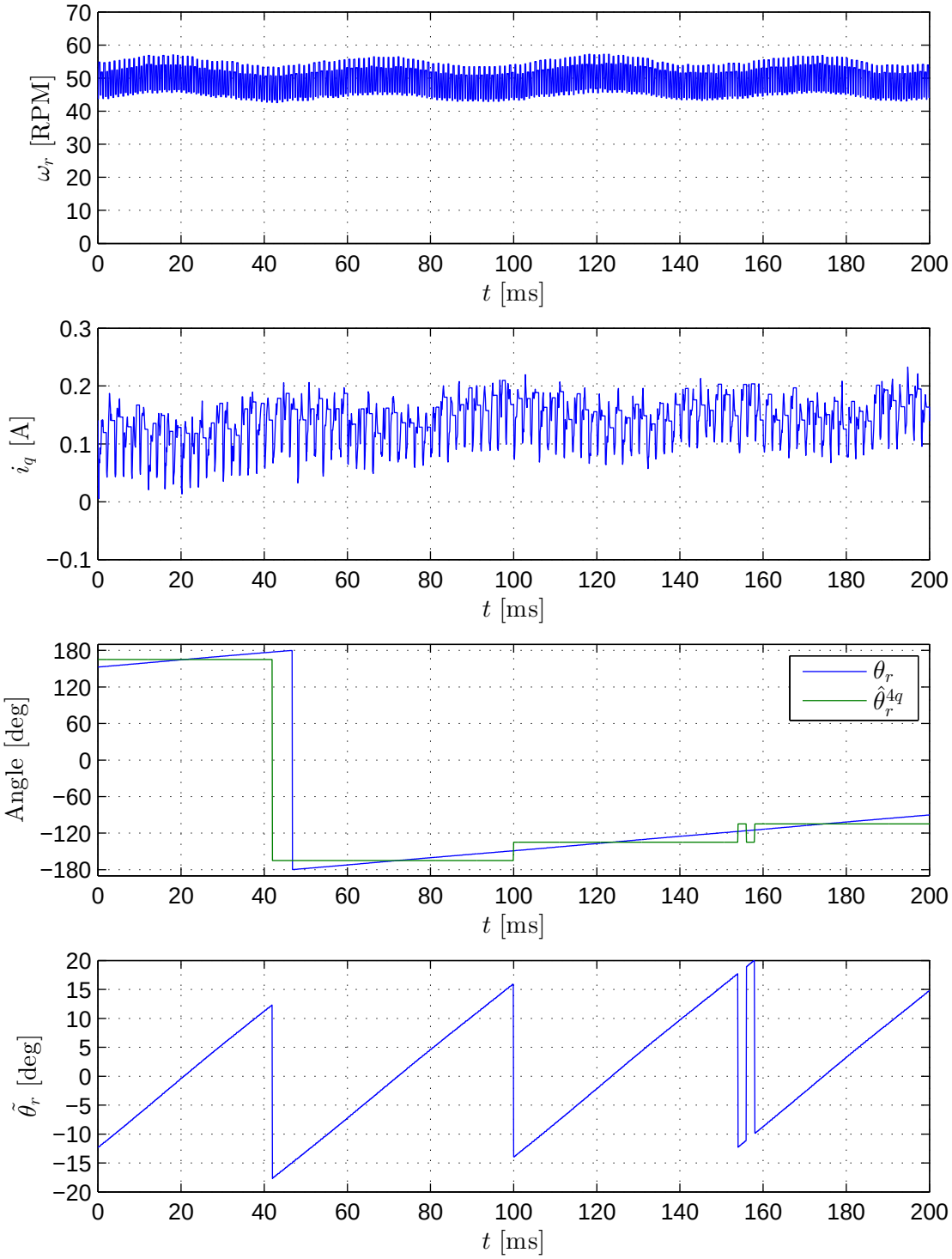


Figure 5.29.: Tracking performance under FOC. Reference velocity of 50 RPM (sector estimation, SEM motor).

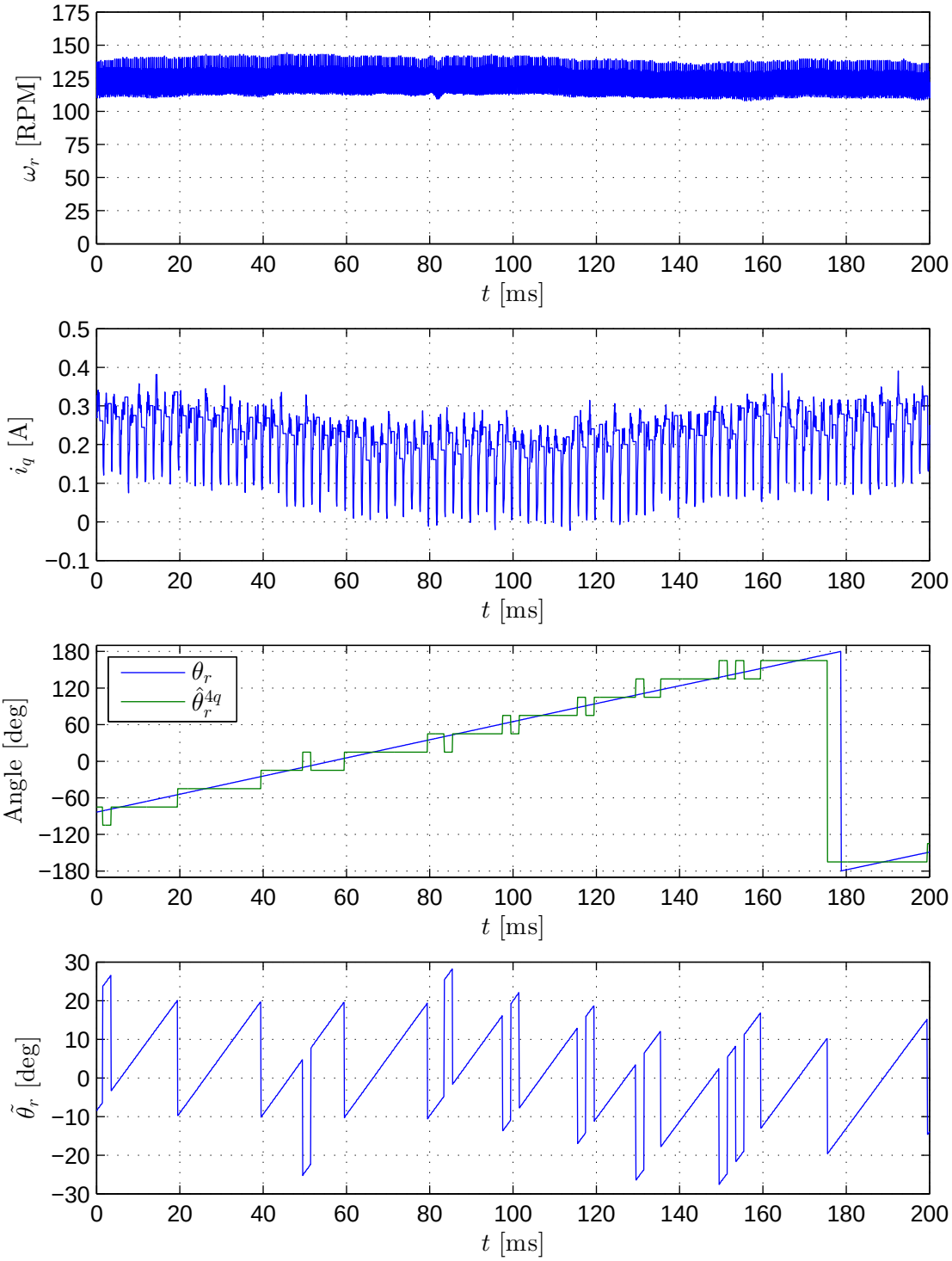


Figure 5.30.: Tracking performance under FOC. Reference velocity of 125 RPM (sector estimation, SEM motor).

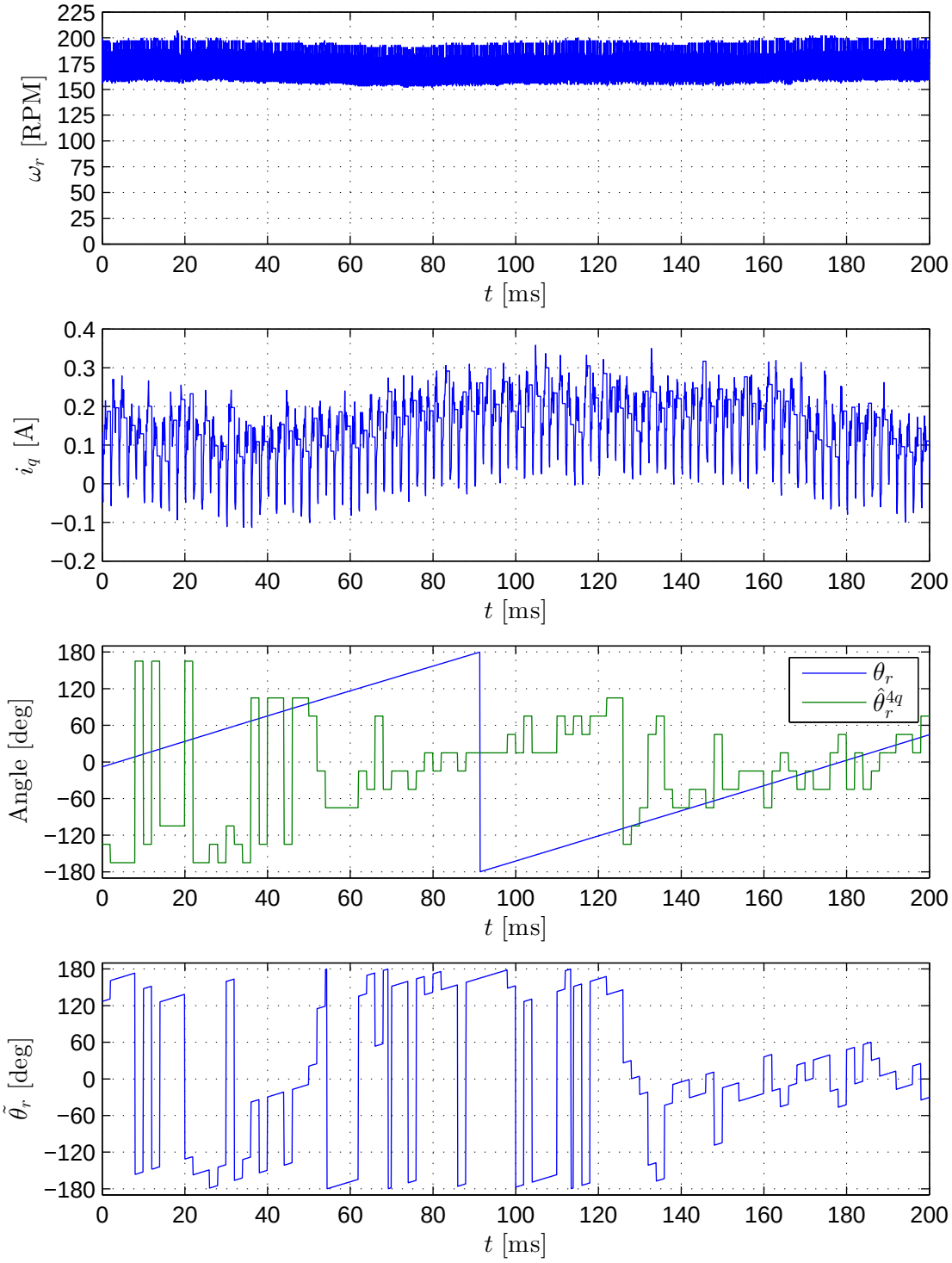


Figure 5.31.: Tracking performance under FOC. Reference velocity of 175 RPM (sector estimation, SEM motor).

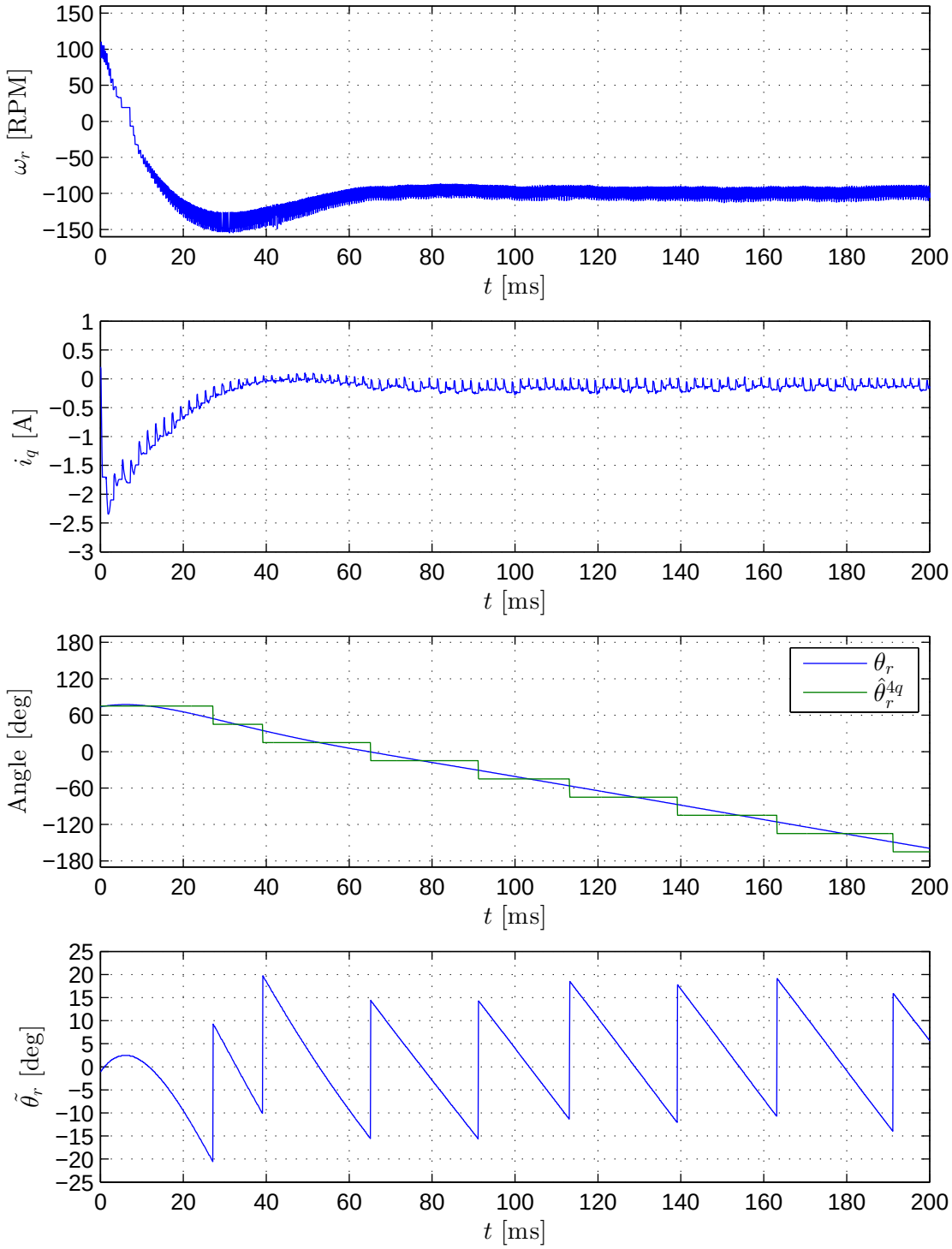


Figure 5.32.: Tracking performance under FOC. Step change in reference velocity of 100 RPM to −100 RPM (sector estimation, SEM motor).

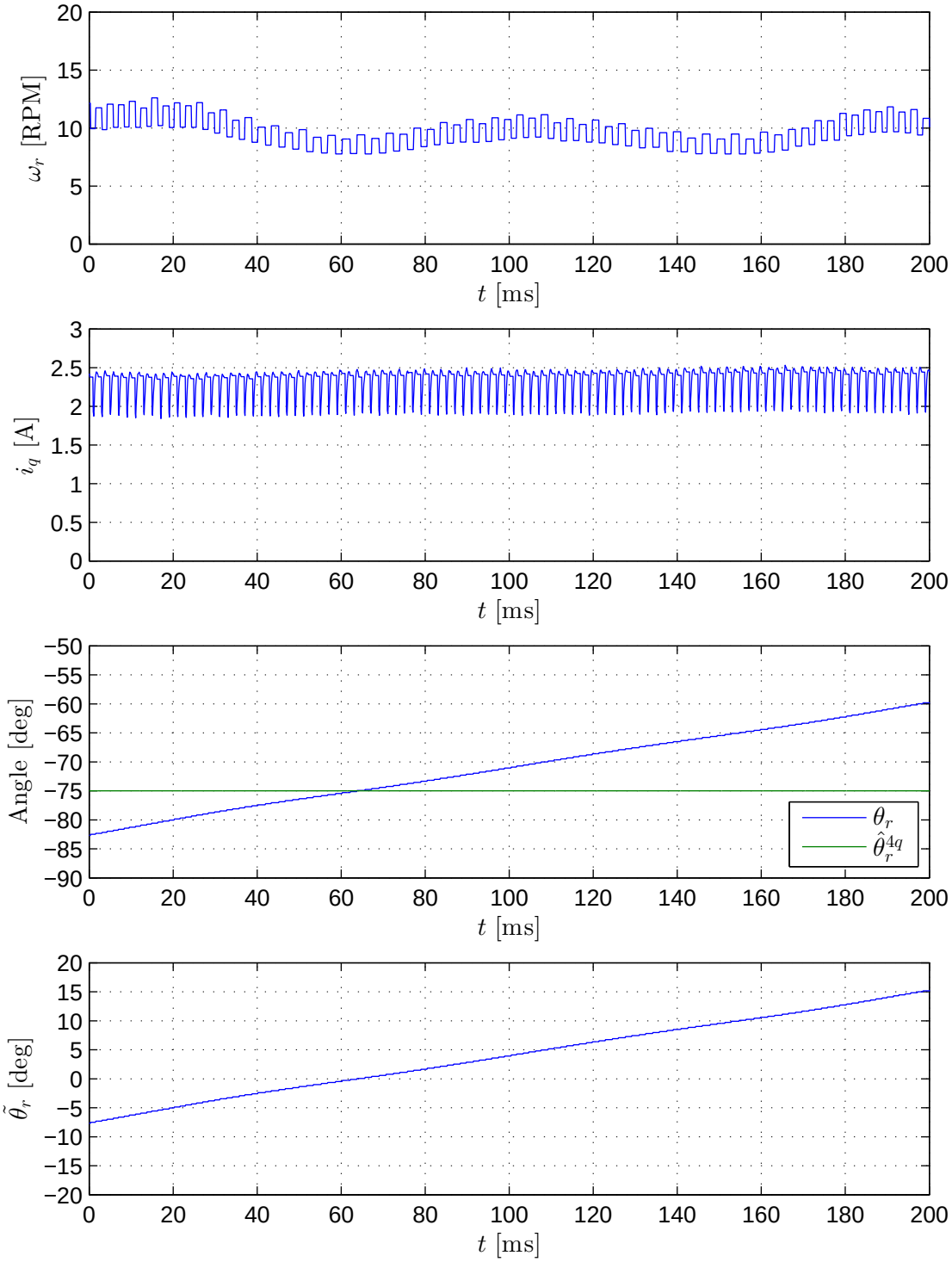


Figure 5.33.: Tracking performance under FOC. Reference velocity of 10 RPM. Load current of approximately 2.5 A (sector estimation, SEM motor).

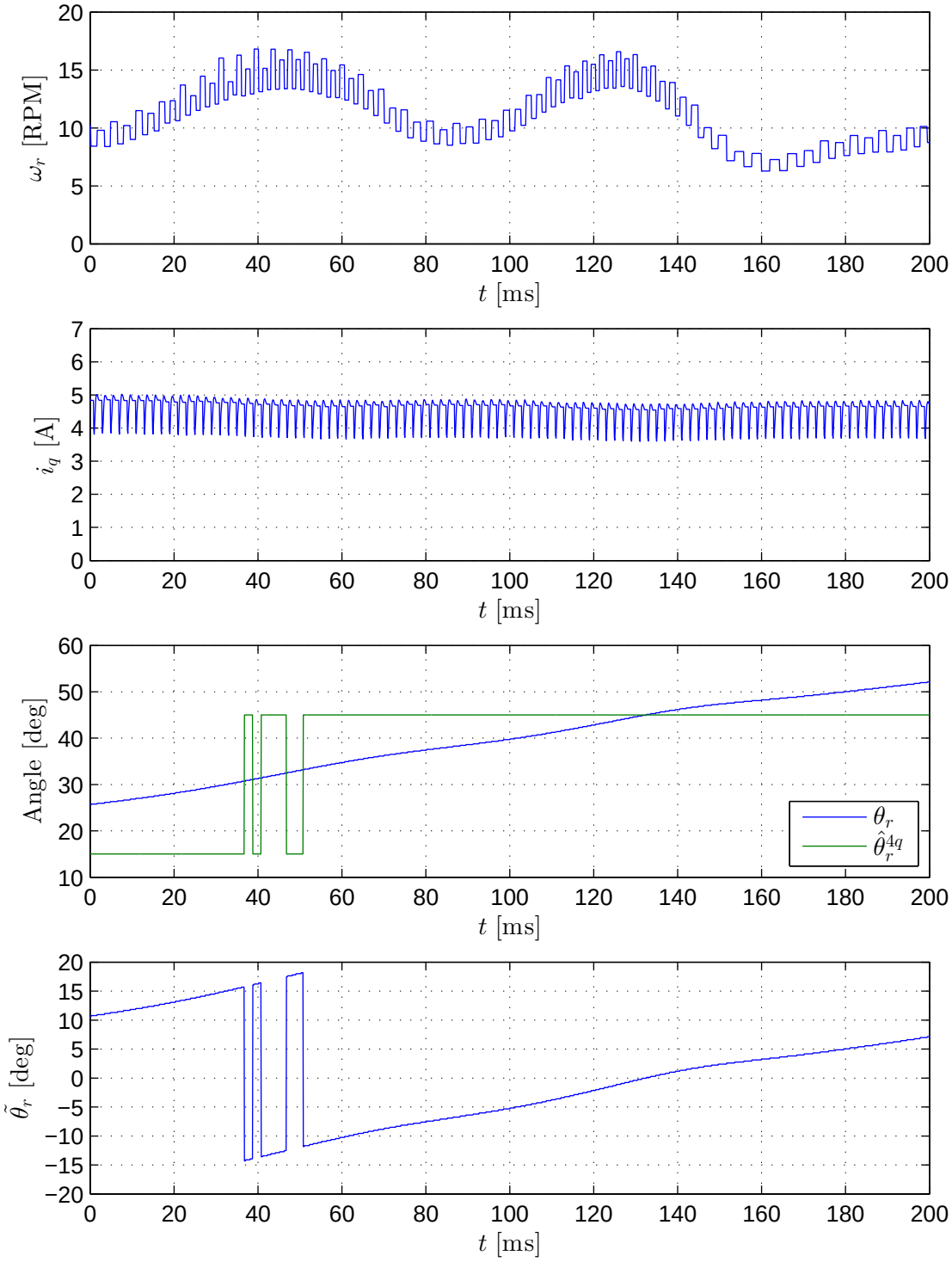


Figure 5.34.: Tracking performance under FOC. Reference velocity of 10 RPM. Load current of approximately 5 A (sector estimation, SEM motor).

## 5.4. Summary

In this chapter, two algorithms were presented that are able to estimate the angular position of the rotor of a SMPMSM based on its anisotropic magnetic properties. These algorithms differ from the one presented in Chapter 4, in that they are based directly on time-domain measurements instead of frequency-domain signal processing, and as such, require no filters that introduce delay.

The INFORM algorithm and its applications are generally well-document in the literature, but here it is presented with additions specifically for making it robust to the inverter voltage error. The effect of prefilters and quantization in digital control systems is also taken into account. Additionally, the sensitivity of the algorithm to magnetic saturation is discussed. As in Chapter 4, measurement results show that the Siemens motor is ill-suited for sensorless control based on the INFORM algorithm. For the SEM motor, however, the estimation error is generally in the range $[-25°; 25°]$ up to its rated current. Above its rated current, the estimation error increases significantly due to the effect of magnetic saturation.

In an effort to simplify the INFORM method, based on the same fundamentals, a new algorithm was developed that restricts itself to utilizing less information than available to the INFORM method. This, in turn, has the effect of restricting the estimate of the rotor position to fixed 30° sectors, which, compared to the INFORM method, results in a slightly worse estimate at low levels of load current. The benefit, however, is that the algorithm is not affected by magnetic saturation and thus its accuracy does not depend on the level of load current. Additionally, its implementation is somewhat simpler. Measurement results show that the Siemens motor is also ill-suited for sensorless control based on the sector estimation algorithm. For the SEM motor, the estimation error is generally in the range $[-20°; 20°]$, regardless of the level of load current.

For both the INFORM and sector estimation algorithms, the speed is limited to approximately 125 RPM for the SEM motor. Above this speed, the quality of the models on which the algorithms are based deteriorate quickly. As a result, the tracking performance of the algorithms degrade significantly.

# 6. Conclusion

Field-oriented control of permanent-magnet synchronous motors provides a hardware platform capable of excellent power density, efficiency and dynamic performance, and all with the ease of controlling a DC motor. It is thus no wonder that this technology has become ubiquitous in recent years with the advent of cheap microprocessors and power electronics. The classical FOC topology does, however, come with the added cost of requiring a position or speed sensor for its reference frame transformations. Ridding the FOC topology of this requirement would represent a significant boon to its users in terms of reduced cost and improved reliability. The methods based on back-EMF estimation have already provided suitable solutions for this problem at higher speeds than dealt with here. In this thesis, for low-speed operation, we have found:

The high-frequency injection methods, an example of which was presented in Chapter 4, provide a continuous estimate of the angular position of the rotor by signal processing of the current response to an injected high-frequency voltage. Their main drawback is that this voltage component must coexist with the fundamental voltage of the machine, and as such, little can be done to work around the error component introduced by the inverter. For these methods, the inverter voltage error must generally be compensated for somehow, which typically requires offline measurements of parameters specific to the inverter.

The INFORM method can generally work in the presence of significant voltage error from the inverter, but it requires synthesizing its voltage vectors with single-leg switching patterns and oversampling the current within a switching period. The accuracy of the algorithm is also sensitive to large variations in load current, the extent of which is difficult to predict as it depends on the construction and geometry of the motor.

The sector estimation algorithm incorporates the robustness of the INFORM method to the inverter voltage error and avoids the complexity associated with oversampling the current. It is a simpler algorithm that has the additional benefit of being able to accurately estimate the position of the rotor regardless of the level of load current present in the motor. The loss of accuracy at low current levels, compared to that of the INFORM method, is considered negligible.

For all the algorithms presented in this thesis, a necessary condition for them to function properly is the presence of a certain degree of effective rotor saliency. This was particularly evident for the case of the Siemens servo motor.

In summary, the main contributions of this thesis are:

- Development of the high-frequency and voltage pulse injection methods in a unified framework of space vectors.
- Modification of the INFORM algorithm to account for the inverter voltage error.
- Development of the sector estimation algorithm.

## 6.1. Future Work

This thesis has been mostly concerned with the ability of the algorithms to accurately and robustly estimate the angular position of the rotor. That is adequate for the purpose of torque control, but for industrial applications of FOC, speed control is predominantly the main concern. As the speed is usually estimated from changes in position between samples, recommendations for future work are:

- Since the high-frequency injection methods can continuously provide an estimate of the rotor position, they might, in terms of speed estimation, have an advantage compared to the INFORM and sector estimation methods, which only provide estimates when they periodically assume control of the machine. It would be worthwhile to consider how this estimation rate impacts the accuracy of the speed estimate.
- The estimate of the rotor position produced by the sector estimation algorithm is inherently quantized. The algorithm effectively has the same output as a very low resolution incremental encoder. It would be interesting to explore what limitations this imposes on the dynamic performance of the speed control loop.

# A. Noise Filtering of the LEM LA-P Series Current Transducer

Figure A.1 shows a schematic of a LEM LA-P series current transducer. The current in the primary winding $I_P$ creates a flux in the surrounding magnetic core that is sensed by the Hall element in its gap[1], which produces a voltage in direct proportion to the flux density, and thereby $I_P$. The Hall voltage is amplified and used to drive a secondary current $I_S$, that creates a flux in the magnetic core in opposition to that of $I_P$. This feedback loop eventually results in $I_S$ mirroring $I_P$ by its turns ratio. Inserting a measurement resistor $R_M$ in the secondary winding thus allows sensing $I_P$ while galvanically isolated from the primary circuit.

A possible issue with these types of current transducers, is how their amplifier stage is implemented. The simple push-pull stage shown in Figure A.1 can introduce significant distortion in the feedback loop if the transistors are not well matched.

For the hardware platform presented in Chapter 3, Figure A.2 shows the DFT of $I_P$ at the input of the DSP as measured by a Tektronix DPO 2014 oscilloscope[2]. The output of the current transducer shows significant noise content above 200 kHz.

Figure A.3 shows $I_P$ as seen from the DSP with and without a single-pole RC anti-aliasing filter with a cut-off frequency of 20 kHz. As seen, the addition of the anti-aliasing filter reduces the RMS value of sensor noise significantly.

[1] $I_C$ is the control current for the Hall element.

[2] The Tektronix DPO2014 oscilloscope specifies at least 40 dB attenuation at the Nyquist frequency of its sampling system.

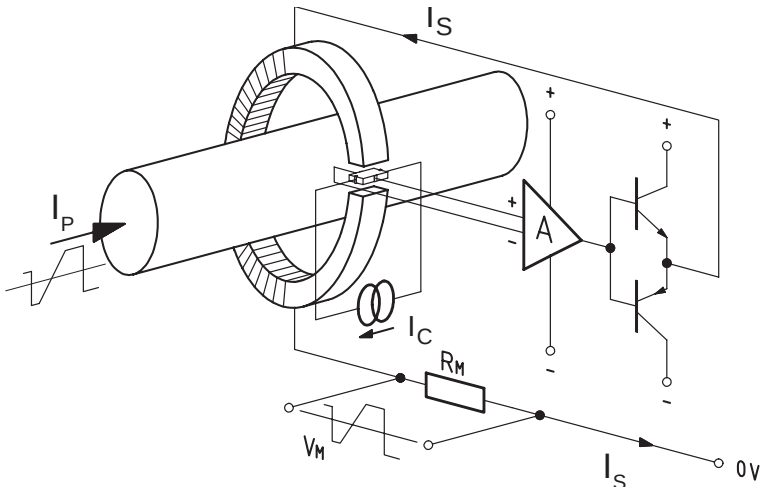


Figure A.1.: Schematic of a closed-loop Hall effect current transducer. Image from *Isolated Voltage and Current Transducers* (2004).

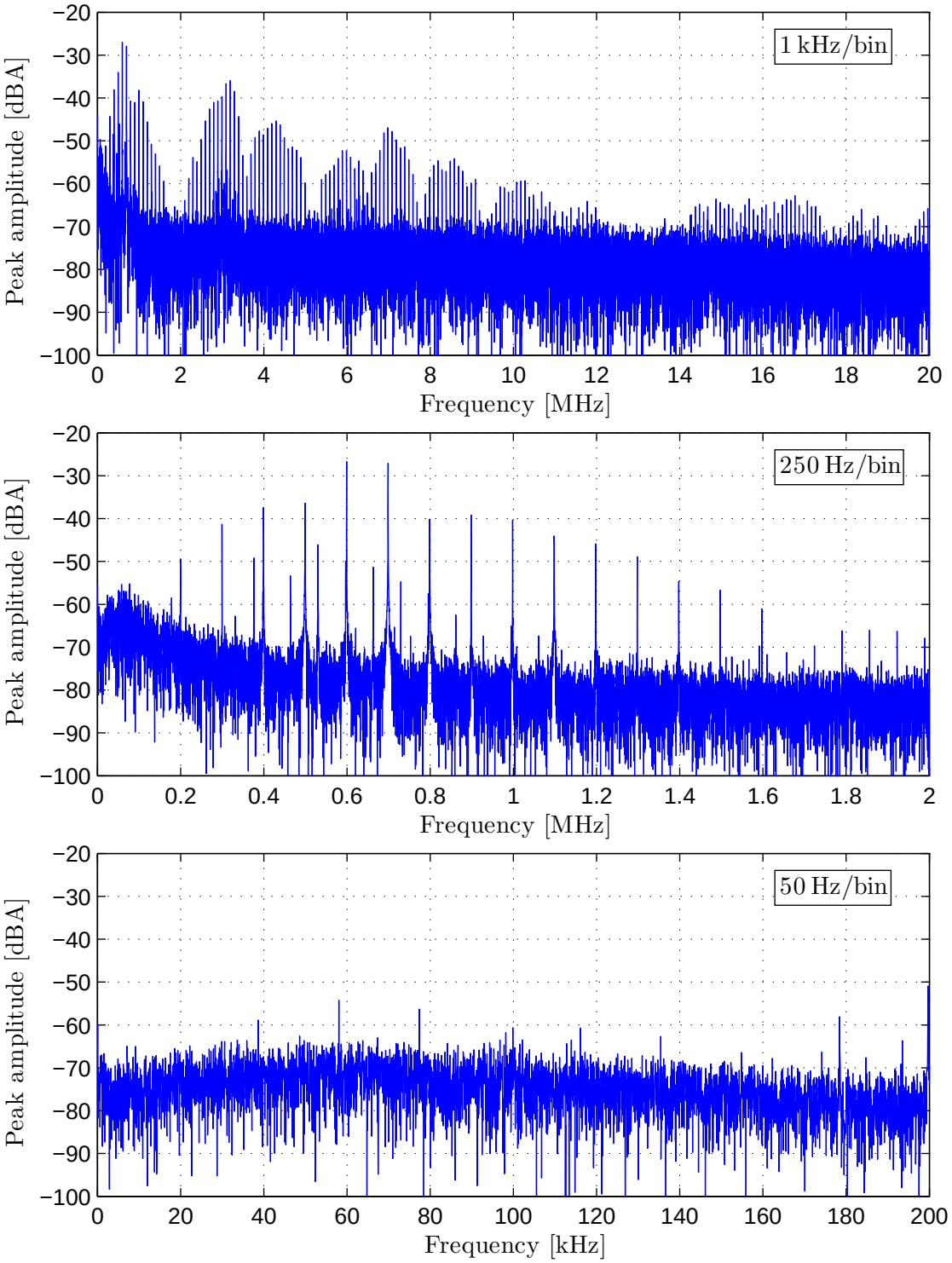


Figure A.2.: DFT of $I_P$ as seen from the oscilloscope.

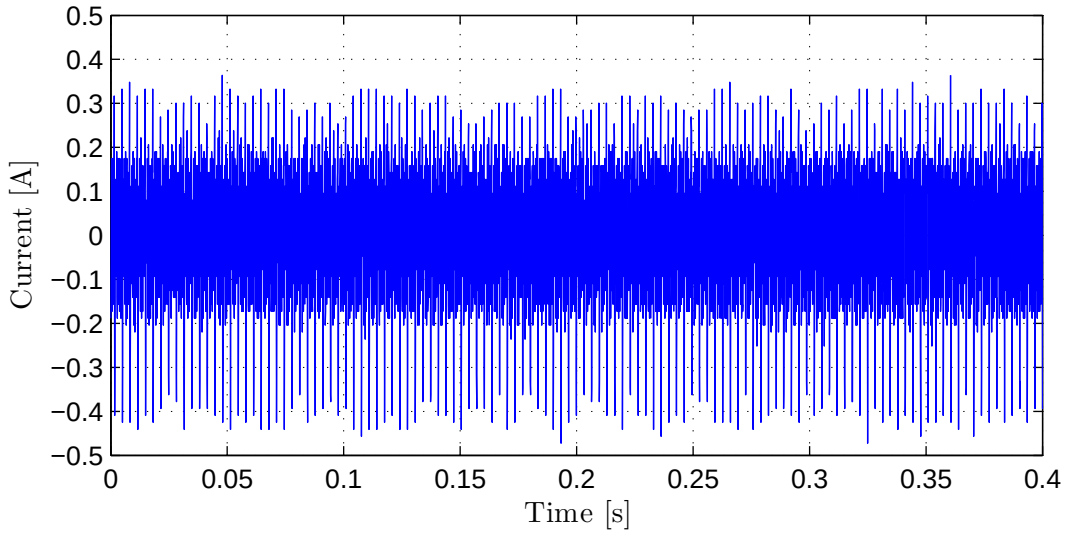


(a) Without anti-aliasing filter. $I_{P,\mathrm{RMS}} = 158\,\mathrm{mA}$

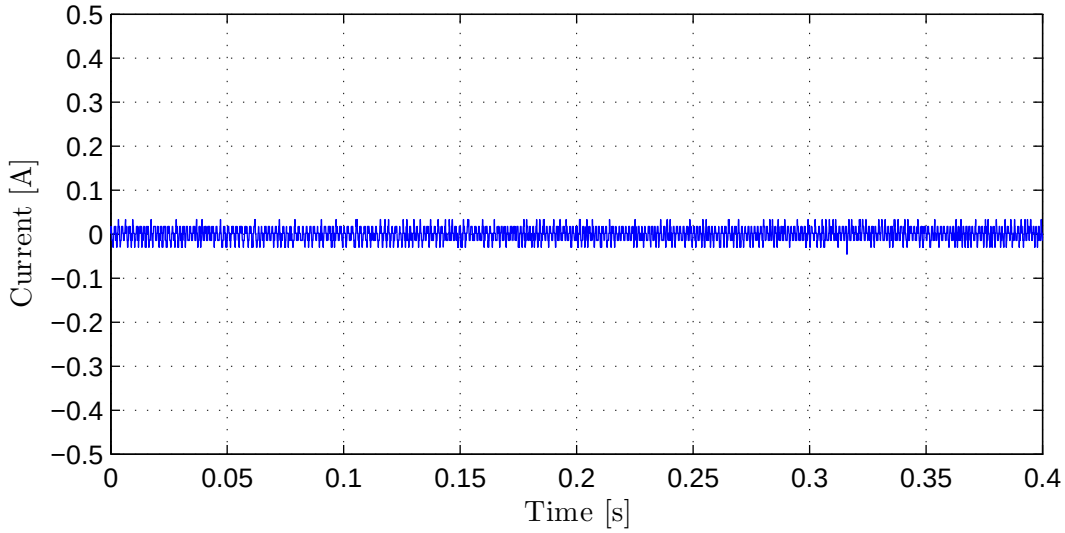


(b) With anti-aliasing filter. $I_{P,\mathrm{RMS}} = 15.1\,\mathrm{mA}$

Figure A.3.: $I_P$ waveform as seen from the DSP.

# Bibliography


Harnefors, Lennart and Hans-Peter Nee (1998). "Model-Based Current Control of AC Machines Using the Internal Model Control Method". In: *IEEE Transactions on Industry Applications* 34 (1), pp. 133–141.

Holtz, Joachim (2008). "Acquisition of Position Error and Magnet Polarity for Sensorless Control of PM Synchronous Machines". In: *IEEE Transactions on Industry Applications* 44 (4), pp. 1172–1180.

*Isolated Voltage and Current Transducers* (2004). *Characteristics - Applications - Calculations*. 3rd ed. LEM.

Jianmin, Wang and Gao Jianwei (2011). "Analysis of Position Estimation Error Resulted from Filter in Carrier Signal Injection Based Sensorless Control of PMSM". In: *Conference Proceedings of the 2011 International Conference on Electrical Machines and Systems*, pp. 1–6.

Kazmierkowski, Marian P. and Henryk Tunia (1994). *Automatic Control of Converter-Fed Drives*.

Kim, Joohn-Sheok and Seung-Ki Sul (1994). "New Stand-still Position Detection Strategy For PMSM Drive Without Rotational Transducers". In: *Conference Proceedings of the 1994 Applied Power Electronics Conference and Exposition* 1, pp. 363–369.

Krause, Paul C., Oleg Wasynczuk, and Scott D. Sudhoff (2002). *Analysis of Electrical Machinery and Drive Systems*. 2nd ed.

Lu, Kaiyuan et al. (2010). "Determination of High-Frequency d- and q-axis Inductances for Surface-Mounted Permanent-Magnet Synchronous Machines". In: *IEEE Transactions on Instrumentation and Measurement* 59 (9), pp. 2376–2382.

Mobarakeh, B. Nahid, F. Meibody-Taba, and F.M. Sargos (2000). "A Self-organizing Intelligent Controller for Speed and Torque Control of a PMSM". In: *Conference Record of the 2000 IEEE Industry Applications Conference* 2, pp. 1283–1290.

Morimoto, Shigeo et al. (2001). "Sensorless Control Strategy for Salient-Pole PMSM Based on Extended EMF in Rotating Reference Frame". In: *Conference Record of the 2001 IEEE Industry Applications Conference* 4, pp. 2637–2644.

Schroedl, Manfred (1992). "Sensorless control of A.C. machines"". In: *VDI Fortschritt-Berichte* 21 (117).

Vas, Peter (1992). *Electrical Machines and Drives. A Space-Vector Theory Approach.*

Xiang, Xiaodong and Yikang He (2007). "Sensorless Vector Control Operation of a PMSM By Rotating High-Frequency Voltage Injection Approach". In: *Conference Proceedings of the 2007 International Conference on Electrical Machines and Systems*, pp. 752–756.

Yongdong, Li and Zhu Hao (2008). "Sensorless Control of Permanent Magnet Synchronous Motor – A Survey". In: *Conference Proceedings of the 2008 Vehicle Power and Propulsion Conference*, pp. 1–8.